Poromechanical Analysis of Deeply Drilled Wellbores for Geo-energy Production

Sina Heidari

A Thesis

In the Department

of

Building, Civil and Environmental Engineering

Presented in Partial Fulfillment of the Requirements

For the Degree of

Doctor of Philosophy (Civil Engineering) at

Concordia University

Montréal, Québec, Canada

June 2023

CONCORDIA UNIVERSITY

SCHOOL OF GRADUATE STUDIES

This is to certify that the thesis prepared

By: Sina Heidari

Entitled: Poromechanical Analysis of Deeply Drilled Wellbores for Geo-energy Production

and submitted in partial fulfillment of the requirements for the degree of

Doctor of Philosophy (Civil Engineering)

complies with the regulations of the University and meets the accepted standards with respect to originality and quality.

Signed by the final examining committee:

Dr. Javad Dargahi	Chair
Dr. Li Li	External Examiner
Dr. Mojtaba Kheiri	Examiner
Dr. Adel M. Hanna	Examiner
Dr. Ahmed Soliman	Thesis Supervisor
Dr. Biao Li	

Approved by Dr. Mazdak Nik-Bakht, Graduate Program Director

7/31/2023 Dr. Mourad Debbabi, Dean
Gina Cody School of Engineering and Computer Science

Abstract

Poromechanical Analysis of Deeply Drilled Wellbores for Geo-energy Production.

Sina Heidari, Ph.D.

Concordia University, 2023

Geo-mechanical analysis and ensuring wellbore stability are paramount for the success of deep geo-energy production projects. The present study addresses the complex challenges arising from geological formations comprising laumontite-rich rocks, fault zones, and fractured rock formations, which significantly influence the mechanical behavior and stability of wellbores.

Tight glutenite reservoir formations containing laumontite minerals pose challenges for geo-energy production due to their complex stress-sensitive mechanical behaviors. With an increase in the confining pressure, there is a transition from the shear dilation to the consolidated compaction in laumontite-rich formations. This study presents the finite element modeling of constitutive behaviors of laumontite-rich rocks using a thermodynamic-consistent plasticity model. Poromechanical analysis is performed to investigate plastic zone development around a borehole in an overpressured reservoir along with a comparison to traditional plastic constitutive models. The findings contribute to understanding and addressing the challenges of wellbore stability in laumontite-rich formations for geo-energy projects.

The wellbore stability of deeply buried petroleum wells in fault zones is another major concern of deep drilling projects. This study also focuses on a super-deep petroleum well drilled into an Ordovician limestone reservoir formation with a buried depth of about 8000 meters located in the Tarim Basin, China. Laboratory tests and dual-porosity theories of poromechanics are employed to derive stress and pore pressure distributions in a limestone formation surrounding the wellbore. The analysis highlights the significance of borehole azimuth and the selection of an optimal well trajectory, considering the strength properties of both the rock matrix and fractures.

Geological formations in the Canadian Shield with natural fractures in fault zones offer enhanced permeability for geothermal development. However, ensuring wellbore stability during drilling and energy production is crucial. The Finite Element modeling is employed to assess the performance of boreholes in fractured rock formations under non-isothermal conditions at a potential deep geothermal site in northern Canada. The analysis considers plastic yielding in the rock matrix and sliding potential along fractures, accounting for the cooling effect. Findings highlight the importance of managing the cooling effect to avoid excess pore pressure build-up and sliding along tilted fractures.

Collectively, this research provides a comprehensive understanding of wellbore stability and geomechanical behaviors in diverse geological formations. The findings contribute to the development of strategies and guidelines for safe and efficient geo-energy production in challenging geological environments.

Acknowledgment

I would like to express my deepest gratitude to Dr. Biao Li, my supervisor, for his unwavering availability, exceptional support, and guidance throughout my studies. Dr. Li's dedication to my research and his willingness to go above and beyond has been invaluable in shaping the outcome of this thesis. Thank you, Biao, for always being there for me, and for your continuous encouragement, patience, and hard work.

I would like to express my heartfelt appreciation to Dr. Antoine B. Jacquey for his invaluable support in utilizing his source code. His guidance and insightful meetings have significantly contributed to the success of this research.

I extend my sincere appreciation to the members of my thesis committee, Dr. Li Li, Dr. Mojtaba Kheiri, Dr. Adel M. Hanna, and Dr. Ahmed Soliman for their valuable insights and suggestions.

I am grateful for the support of the Concordia Graduate Excellence Award granted to doctoral students, as this work would not have been possible without it. Additionally, I extend my appreciation to Concordia University for the financial assistance provided through the Seed start-up grant.

I would like to express my heartfelt appreciation to Dr. Neda Faridian and Dr. Mansour Rajabi, close friends of my parents, who have always been there for me. Their unwavering presence in my life has had a profound impact, and I will forever cherish the memories we have created together. Neda and Mansour, your unforgettable hospitality and support from the moment I arrived in Montreal have meant the world to me. I am deeply grateful for your friendship, wisdom, and encouragement.

"Friends make life richer."

Studying at Concordia University provided me with the opportunity to meet new friends. I am sincerely grateful for Hooman Dabirmanesh, who has consistently been there for me, offering a listening ear, answering my questions, and engaging in inspiring discussions. I would also like to acknowledge the memorable moments shared with Mehdi Kharazmi, Mohammadhossein Sojoudi, Saeed Vadiee, Abdulnaser Ibrahim Alamari, Emad Norouzi, and Sohail Akhtar. I wish each of you the very best in life.

It has always been a source of pride for me to have made numerous friends outside of Concordia University. I am eternally grateful to each of them for bringing a smile to my face during difficult situations and making my experience of living abroad so much easier. If my memory serves me well, I would like to mention their names here: Yahsar Rafati, Mohammad Rahnemoun, Giti Nouri, Abtin Jahanbakhshzadeh, Mohammadreza Birjandi, Mitra Misaghi, Nahid Seif, Rasoul Panahi, Hamid Ghomi, Bahador Ziaeemehr, Armina Shirangi, Vahid Dolatkhah, Elahe Rafiei, and Mansoureh Salehi.

Last but certainly not least, I want to express my deepest gratitude to my family: my father, Ebad, my mother, Effat, and my brother, Arash. I consider myself incredibly fortunate to have each of you in my life. Your unwavering love, endless encouragement, and unconditional support have been the driving force behind me, propelling me forward up to this point. It is because of your presence, belief in me, and constant support that I have been able to overcome challenges and achieve my goals. I am forever grateful for the foundation of love and strength you have provided, and I am honored to have you by my side.

Dedication

To my lovely parents

Contributions of Authors

The author of this thesis, Sina Heidari, has followed the guidelines for preparing a manuscript-based thesis format. The research conducted by Sina Heidari, under the supervision of Dr. Biao Li, is presented in chapters 3 to 5 of this thesis. These chapters discuss the outcomes of numerical modeling and analytical solutions. As a result of this research, several publications have been produced.

- Chapter 3

1) Heidari, S., Li, B., Jacquey, A.B., Xu, B., 2023. Constitutive modeling of a laumontite-rich tight rock and the application to the poromechanical analysis of deeply drilled wells. Rock Mech. Bull. 2, 100039. https://doi.org/10.1016/j.rockmb.2023.100039

SH: Coding, analysis, draft preparation, revision

BL: Supervision, draft preperation, revison

ABJ: Coding, revison

BX: Data collection

- Chapter 4

2) Heidari, S., Li, B., Zsaki, A.M., Xu, B., Wang, C., 2021. Stability analysis of a super deep petroleum well drilled in strike-slip fault zones in the Tarim Basin, NW China. Arab. J. Geosci. 14, 675. https://doi.org/10.1007/s12517-021-06709-z

SH: Coding, analysis, draft preperation, revison

BL: Supervision, draft preperation, revison

AMZ: Supervison, revison

BX: Data collection

CW: Experiments

- Chapter 5

3) Heidari, S., Li, B., Jacquey, A.B., 2023. Finite element modeling of wellbore stability in a fractured formation for the geothermal development in northern Quebec, Canada. Geoenergy Science and Engineering. *In Review.* Submitted Manuscript Number: PETROL34106

SH: Coding, analysis, draft preperation, revison

BL: Supervison, draft preperation, revison

ABJ: Coding, revison

Table of Contents

List of Tables

List of Figures

Chapter 1

Introduction

1.1. Background and problem statement

Wellbore instability is a widely recognized problem that occurs in the fields of geo-energy and geological engineering. It is a failure phenomenon that refers to the deformation, and collapse of a wellbore, which is a hole drilled into the earth's surface. Wellbore stability is particularly important for deep geo-engineering projects such as deep sequestration of carbon dioxide, deep petroleum resources production, and deep geothermal energy production and storage. Wellbore instability can create a major economic loss to the whole project. In addition, borehole failure or integrity issues may trigger fluid leaking into groundwater and contaminate the surrounding ecosystem. Well failure must be mitigated to prevent harmful effects on the population and goods, and on the project's sustainability and acceptability. In the past decades engineers and geologists have striven hard to mitigate the geo-risk through analyzing the geological conditions and selecting appropriate wellbore support systems and drilling techniques to prevent instability. Various types of wellbore-related problems have been identified and explored in literature. The most frequent ones include wellbore breakouts, induced fractures, and fracture reactivation. These failures can occur in different modes, such as shear failure, tensile failure, or sliding along weak planes (Chen et al. 1996). Having a thorough understanding of these failure mechanisms and the factors that trigger each mode of failure is crucial in designing wellbore trajectories and determining appropriate drilling mud. There are two common failure modes during the drilling of deeply buried wellbores: (1) plastic yielding of host rock formation and (2) sliding along weak planes.

The ability to accurately predict plastic deformation and failure in wellbore stability analyses requires a thorough understanding of the deformation mode and failure mechanism in the rock surrounding the wellbore (Garavand et al. 2020). Laboratory experiments have shown that porous rocks can deform under both shear-induced dilation and shear-enhanced compaction mechanisms, depending on the stress state (Wong et al.

1997, Vajdova et al. 2004, Baud et al. 2006). The shapes of the deformation and failure patterns around the wellbore are influenced by the initial stress state and local stress paths. Examining the local stress paths in the near-wellbore zone provides a better understanding of the reasons for different types of failure mechanisms including the shear compaction and dilation. The transition from an isotropic to an anisotropic stress state leads to an increase in the deviatoric part of the effective shear tensor, which results in the development of inelastic deformation. Under increasing confining pressure conditions, certain rocks, such as laumontite-rich reservoir rocks, exhibit a transition from shear to compaction-yielding behavior. Most previous constitutive models for stress-strain behaviors in rocks have primarily focused on brittle rocks. The significance of incorporating strain hardening/softening behavior in the poromechanical analysis of wellbore stability has been highlighted in the study by Chen et al. (2012). However, there is limited research specifically addressing the constitutive behavior of rocks that can be classified as brittle/ductile materials. It is crucial to develop a more accurate characterization of constitutive behavior that can capture the transition from shear to compaction yielding. This understanding is essential for analyzing wellbore stability in deep geo-energy engineering projects.

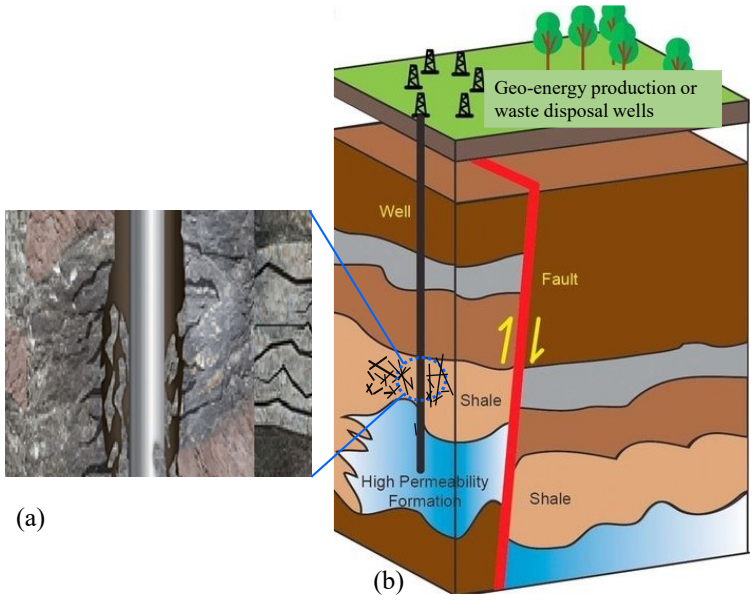

Fig. 1.1. (a) A plastic zone around the fractured wellbore; from https://geodatadrilling.com/ (b) wellbore boundaries; modified after Hosseini et al. (2018)

Sliding failure along weak planes like natural fractures that intersect with the wellbore has recently been reported as one of the significant causes of wellbore instabilities during drilling operations in the geo-energy industry (Younessi and Rasouli, 2010). This occurs when the wellbore intersects with existing fractures in the surrounding rock (Figure 1.1). If the drilling fluid penetrates through existing fractures in the rock, it can cause the fractures to become destabilized and potentially lead to the reactivation of the fracture (Proctor et al., 2020; Zhang et al., 2009). This reactivation can cause the surrounding rock to become unstable and may ultimately result in wellbore instability (Li 2022). Analyzing the stability of wellbores is crucial for determining the wellbore trajectory and drilling mud pressure. When dealing with reservoirs in fault zones, natural fractures weaken the rock matrix and create pathways for pore fluid dispersion. Therefore, the study of wellbore stability must account for the dual-porosity and dual-permeability characteristics of both rock fractures and the rock matrix. It is essential to capture the stresses and variations in pore pressure in both the rock matrix and fractures to conduct a comprehensive analysis of wellbore stability. Additionally, the impact of fracture strength should also be taken into consideration. Moreover, there is a limited comprehension of how wellbores behave in fractured formations when subjected to thermal disturbances, considering the plastic yielding of the rock matrix and the possibility of fractures sliding. This knowledge gap is especially significant for deep geothermal energy engineering projects. Therefore, numerical models are required to accurately quantify the plastic yielding of the rock matrix and the potential sliding of specific fractures, considering the non-isothermal effects.

1.2. Research objectives and contributions

The main objective of this thesis is to present computational approaches for fully coupled poromechanical analysis of deeply drilled wellbores. Two major contributions are summarized below:

(1) The application of a thermomechanics-based constitutive model to the poromechanical analysis of deeply drilled wellbores incorporating the shear dilation to compaction transition behavior of host rocks.

(2) On Thermo-Hydro-Mechanical (THM) responses of deep wellbore drilled in fractured formations based on analytical solutions and the Finite Element Method (FEM).

towards this, the following sub-objectives are achieved:

1- Formulating and compiling the codes of Hydro-Mechanical (HM) analytical solutions for single porosity and dual porosity media.
2- Investigating the fracture strength in the poromechanical analysis of wellbore stability in fractured porous media using dual porosity analytical solutions.
3- Validating the HM Finite Element numerical model using a single porosity analytical solution.
4- Performing HM Finite Element simulations of a wellbore considering a thermomechanics-based constitutive model.
5- Formulating and compiling a code of THM analytical solution for single porosity media.
6- Validating the THM Finite Element numerical model using a single porosity analytical solution.
7- Conducting THM Finite Element numerical simulation of a wellbore drilled near a fractured formation.

1.3. Thesis organization

This thesis is divided into six chapters. Chapters three to five are manuscripts for journal articles that are published or currently under review as indicated in the list of publications.

The organization of the thesis is as follows:

- Chapter 1 includes an introduction, problem statements, research objectives, and thesis organization.
- Chapter 2 presents a comprehensive literature review explaining the detailed problem statements. The available numerical and analytical solutions were

discussed. The open-source codes employed in this study to perform numerical simulations were also explained.

- Chapter 3 presents "The application of a thermomechanics-based viscoplastic constitutive model on deeply drilled wellbore stability analysis". In this chapter, the mineral composition of the highly porous laumontite-rich rock sample was studied. The stress-strain behavior of the sample was modeled employing a new constitutive model and validated with experimental results. The FEM numerical solution was validated using single porosity analytical solutions. The plastic zone around a wellbore drilled in an over-pressured reservoir was modeled.
- Chapter 4 presents "The stability analysis of a super deep petroleum well drilled in strike-slip fault zones in the Tarim Basin, NW China". In this chapter laboratory characterization of mineral compositions and micro-structures of Ordovician limestone samples were investigated. The dual porosity analytical solution was validated using the Single porosity code. The effect of in-situ stress condition and wellbore inclination on the stress analysis was investigated using a dual porosity solution. The importance of considering fracture strength in the poromechanical analysis of wellbore stability in fractured porous media was highlighted.
- Chapter 5 presents "The performance of wellbores drilled in a fractured formation for the geothermal development in northern Quebec, Canada". The geologic characteristics of the fractured rock in the Kuujjuaq community in northern Quebec were discussed. Two benchmarks were shown to show the accuracy of the coupled THM equations. A numerical simulation of an overpressured wellbore was performed to validate the FEM code using single porosity THM analytical solution. The slip tendency of a fracture near a drilled wellbore was investigated by numerical modeling. The effect of cooling and stress anisotropy on the slip tendency of the fracture was studied.
- Chapter 6 includes the summary of the thesis, conclusions, and recommendations for future work.
- Appendix A provides the HM analytical equations for single porosity media which were used to validate the numerical simulations presented in Chapter 3.

- Appendix B provides the HM analytical solutions for dual porosity media, which are relevant to Chapter 4.
- Appendix C presents the THM analytical solutions for a single porosity media which were employed to validate the numerical models discussed in Chapter 5.
- Appendix D solves an example using the HM dual porosity analytical solutions provided in Chapter 2 validating them against single porosity analytical solutions.
- Appendix E includes two benchmarks that were solved to demonstrate the accuracy of the THM numerical simulation by comparing them to their analytical solutions.

Chapter 2

Literature Review

2.1. Introduction

The objective of this thesis is to present a computational model for the fully coupled poromechanical analysis of deep wellbores. This chapter is divided into five sections. The first section establishes the general workflow of different researchers on wellbore stability. The second section introduces two main topics of interest in this research: (1) The transition from shear dilation to compaction in the poromechanical analysis of wellbores, and (2) the fracture sliding potential of drilled geothermal wellbores.

The research consists of both analytical and numerical simulations; hereupon the comprehensive review of the relevant analytical and numerical solutions will be conducted in the third and fourth sections. The **M**ultiphysics **O**bject **O**riented **S**imulation **E**nvironment (MOOSE) which is an open-source tool used for the numerical simulations of this thesis will be introduced in the last section. The last section of this chapter explains the coupled equations implemented in MOOSE by previous researchers, which were utilized to perform wellbore simulations relevant to the current study.

2.2. General background

Borehole instability issues commonly encountered in deep bedding planes containing clay minerals, such as shales, are often influenced by factors including mud weight, in situ stress, wellbore orientation, chemical reactions, and thermal convection (Ma and Chen, 2015). The primary cause of wellbore instability is typically attributed to incorrect drilling mud weight (Lee et al., 2012; Zoback, 2007). Inadequately low mud weight can result in shear failure around the borehole, leading to collapses, while excessively high mud weight can cause tension failure, resulting in lost circulation. Various researchers have proposed methods for analyzing wellbore stability, assuming linear elastic and isotropic strength properties of the rock (Aadnoy and Ong, 2003; Kang et al., 2009; Lee et al., 2012; Zoback, 2007; Zoback et al., 1985). However, these methods may yield

inaccurate results when applied to wellbores in deep reservoirs due to the anisotropic nature of formations, the neglect of natural fractures, pore pressure propagation, and the coupling phenomena (Abousleiman and Cui, 1998; Ekbote and Abousleiman, 2006; Meng et al., 2019; Younessi and Rasouli, 2010; Yuan et al., 2013; Zhang et al., 2008; Zhang, 2013). Several semi-analytical elastoplastic solutions have been developed incorporating both Tresca and Mohr-Coulomb failure criteria (Bradford and Cook, 1994; Chen and Abousleiman, 2017; Fung et al., 1996; Zhou et al., 2016). However, the applicability of these models in petroleum applications is limited (Garavand et al., 2020). On the other hand, some of these models do not consider the distribution of pore pressure or the potential occurrence of compaction localization regions.

2.3. Wellbore stability issues

2.3.1. Dilation to compression transition

Recent research investigating porosity changes and yield stress in crustal rocks with varying porosities has revealed the existence of two distinct types of flow. In rocks with low porosity, the dilation of pore space is frequently observed, and the yield stresses associated with this type of dilatant flow exhibit its dependence on pressure; conversely, significant reductions in porosity are typically observed in rocks with high porosity, and the yield stress for this type of flow decreases as the effective pressure increases (Wong et al., 1997). In the field of reservoir engineering, the stability of a deep borehole has been discovered to be highly influenced by the degree of work hardening caused by shear-enhanced compaction (Veeken et al., 1989). In the study of Garavand et al. (2020) a wellbore stability analysis is performed using an elastoplastic model that incorporates a non-associated flow rule and combined yield surfaces; plastic deformation is simulated using dynamic equations commonly employed in wave propagation problems. The model of Garavand et al. (2020) considers both shear and compaction modes, accounting for the hardening of the medium followed by a subsequent softening process. The research of Garavand et al. (2020) emphasizes the importance of considering the potential occurrence of irreversible deformation in different modes, specifically dilatancy and compaction, when analyzing wellbore stability. In elastoplastic modeling, the inclusion of the plastic

potential is crucial as it determines the extent of rock deformation beyond the yield point. The use of an associated flow rule, where the yield surface serves as the plastic potential, often leads to discrepancies with experimental data due to the incorporation of the dilatancy coefficient into the internal friction angle. On the other hand, employing a non-associated flow rule allows for a more accurate representation of inelastic deformation. However, it necessitates the formulation of an independent potential function with additional parameters and measurements, which remains a complex task in studying and modeling rock behavior. Despite the complexity involved, most studies primarily focus on analyzing constitutive relationships and interpreting experimental observations (Baud et al., 2006; Vajdova et al., 2004) paying less attention to modeling inelastic deformation in real-world scenarios such as oil and gas wells.

2.3.2. Fracture sliding potential

One of the most common failures observed near the wellbore is fracture sliding. When drilling a wellbore to access the reservoir formation, which is typically located several hundred to several thousand meters below the surface, various formations, rock masses, and discontinuities are encountered. The weak planes have the potential to slide when the wellbore intersects them (Younessi and Rasouli, 2010). Fracture sliding occurs when the shear stress applied to a plane in the rock mass exceeds its shear strength. Formations are often heterogeneous and anisotropic, so sliding occurs along the weakest plane, such as a fracture plane if present. The Mohr-Coulomb criterion is a widely used sliding failure envelope in geomechanics (Figure 2.1).

$$\tau = \mathrm{C_d} + \sigma_n' \tan\phi_\mathrm{d} \tag{2.1}$$

Where τ and σ_n' are the shear and effective normal stresses applied on a discontinuity plane, ϕ_d, and $\mathrm{C_d}$ are friction angle and cohesion respectively.

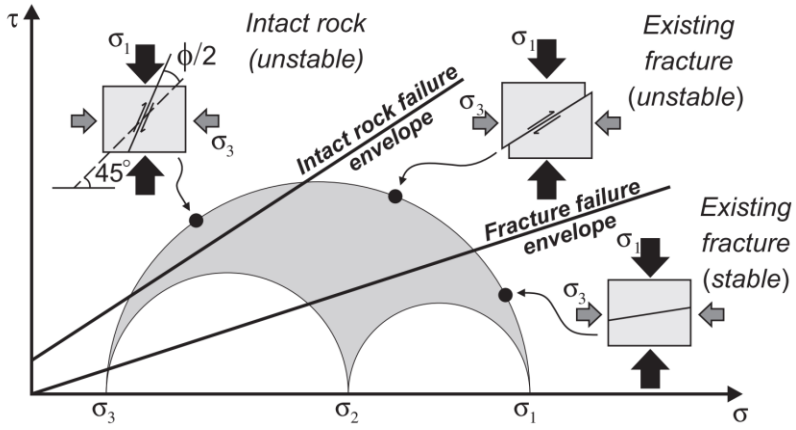

Fig. 2.1. The stress state illustrated by Mohr's circle (Younessi and Rasouli, 2010).

Fracture reactivation can occur at three distinct stages throughout the lifespan of a wellbore: during drilling operations, during the production phase resulting from reservoir depletion, and during fluid injection. Sliding takes place in each of these cases, but the specific mechanisms of sliding differ. In cases where the drilling fluid infiltrates the formation due to the absence or thinness of the mud cake (A physical barrier to prevent further penetration and loss of drilling fluid), it can penetrate existing fractures and raise the pressure along the fracture plane. As a result, the effective stress applied perpendicular to the fracture plane decreases. According to the Mohr-Coulomb criterion, this altered stress condition may surpass the shear strength of the fracture, leading to the sliding of the fracture plane, as shown in Figure 2.2. The study of Younessi and Rasouli (2010) focuses on investigating the sliding mechanisms associated with drilling operations by utilizing the interaction matrix connected to the Mohr-Coulomb criteria. The interaction matrix is a matrix containing the effective fracture parameters that affect the sliding tendency. Dip direction, roughness, aperture of the fracture, effective induced stresses, pore pressure, and drilling mud density were found to be the six parameters that play a major role in controlling fracture sliding potential. The interaction matrix corresponding to these parameters was constructed in the study of Younessi and Rasouli (2010).

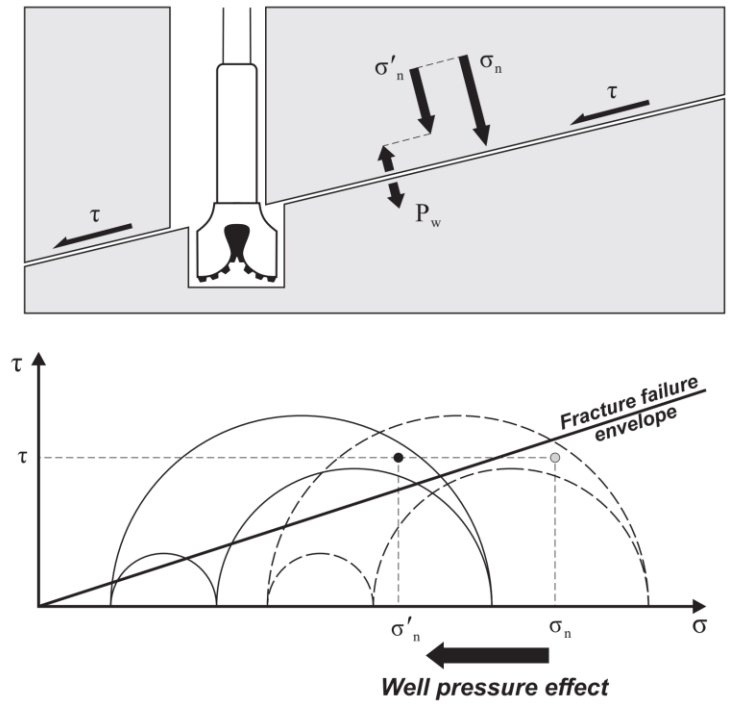

Fig. 2.2. The shear failure of a fracture plane (Younessi and Rasouli, 2010).

The research of Younessi and Rasouli (2010) introduces a method for analyzing the potential sliding of a fracture that intersects a wellbore during drilling operations. The research of Younessi and Rasouli (2010) highlights the considerable impact of effective stresses on the sliding potential. Additionally, it reveals that the drilling fluid plays a dominant role in the system, which is advantageous since it is the only parameter that can be typically controlled during drilling in practical terms. Numerous drilling projects have been conducted in the Tarim Basin, located in the northwest region of China to reach an Ordovician target zone situated at an extraordinary depth of over 7500 meters (Li et al., 2022). The Ordovician formation is situated within a graben structure. Through seismic analysis and image logging data obtained from various reference wells, it has been observed that the target formation exhibits extensive bedding planes and natural fractures. This indicates a significant potential for encountering challenges such as borehole instability or other complications while drilling through the fragmented Ordovician zone.

The identification of an ultra-deep fault-karst reservoir located in the Shunbei area of the Tarim Basin has garnered significant interest among researchers in recent years. Zhou et al. (2020) and Chen et al. (2020) conducted studies using established three-

dimensional (3D) geomechanical models to analyze the distribution of stresses and pressures around the Shunbei 1 and 5 fault zones. The results of these studies shed light on the failure mechanisms and intricate issues related to wellbore instability. It was found that challenges like borehole collapse and lost circulation, frequently encountered during drilling operations, were primarily attributed to factors such as significant depth, complex lithology, extensively developed natural fractures, and stress concentration.

2.4. Analytical solutions of wellbores

Poroelastic and thermoporoelastic models have found extensive application in various engineering fields, including the analysis of wellbore stability (Abousleiman and Ekbote, 2005; Li et al., 2018; Liu and Abousleiman, 2016; Wang and Dusseault, 2003; Wu et al., 2012; Zhang et al., 2003). Semi-analytical solutions offer valuable insights into different scenarios and conditions. For instance, Wu et al. (2012) presented a solution for a vertical wellbore subjected to hydrostatic stress. To accurately capture the pressure history observed in the field, conventional thermo-poroelastic models based on single-porosity and single-permeability assumptions may be insufficient. Therefore, more sophisticated formulations, such as the dual porosity concept, have been developed to provide a more precise description of stress and fluid pressure evolution in practical reservoirs (Nguyen et al., 2009; Zhang et al., 2003). The dual-porosity model offers a refined approach to analyze reservoir behavior by considering the presence of distinct pore systems with different properties and connectivity. This allows for a more realistic representation of the complex fluid flow and heat transfer processes occurring within the reservoir. Li (2003) focused on a vertical wellbore under non-hydrostatic stress. Abousleiman and Nguyen (2005) developed a solution for an inclined wellbore in a naturally fractured porous medium. Nguyen et al. (2009) and Nguyen and Abousleiman (2010) addressed the behavior of an inclined wellbore in a chemically active fractured porous medium. A fully coupled N-porosity N-permeability poroelastic formulation was derived by Mehrabian and Abousleiman (2014), and Liu and Abousleiman (2016). In the context of THM simulation of dual-porosity media, Khalili and Selvadurai (2003) introduced a comprehensive coupled THM formulation. This formulation provides a general framework for analyzing the behavior of dual-porosity systems and has been

applied to field design in hot dry rock for enhanced geothermal systems by Gelet et al. (2012) and Li et al. (2018). A novel integrated formulation was introduced by Wang et al. (2021) to simulate the behavior of a naturally fractured formation subjected to non-isothermal conditions and two-phase fluid flow. The formulation utilizes a dual-porosity model and specifically focuses on scenarios involving a constant flow injection rate.

The application of dual-porosity models has expanded beyond the study of mechanical deformation and fluid flow alone. Researchers have also incorporated thermal coupling and two-phase flow phenomena into the theoretical and numerical analysis of dual-porosity systems. This extension enables a comprehensive understanding of the dynamic behavior of reservoirs under varying thermal and fluid saturation conditions. By adopting dual-porosity models, researchers and engineers gain a more comprehensive and accurate representation of the stress and fluid pressure evolution in reservoirs. This enhanced understanding facilitates better reservoir management and decision-making processes, ultimately improving the efficiency and performance of practical reservoir operations. The published semi-analytical solutions and formulations contribute to the understanding of THM borehole behavior under various conditions, enabling more accurate analysis and design in practical applications. They offer valuable tools for assessing the response of boreholes in different geological settings and can support decision-making processes in the field of geothermal energy and reservoir engineering.

2.5. Numerical analysis of wellbores

Analytical solutions are often insufficient when it comes to addressing complex engineering problems that involve intricate boundary and loading conditions. In practice, analytical solutions are commonly employed to validate the capabilities of numerical programs, which are better equipped to simulate intricate geomechanical scenarios. Zhang et al. (2003) introduced a numerical approach that encompasses dual porosity poroelastic formulations, effectively integrating solid deformations and fluid flow in both the matrix and fracture systems of naturally fractured reservoirs. Using the FEM, Zhang et al. (2003) employed a solution to address the issue of an inclined wellbore revealing that, in comparison to the single porosity solution, the dual porosity solution exhibited a

significantly reduced area prone to shear and spalling failures, along with a slightly larger area susceptible to fracturing. Consequently, a wellbore situated in a dual-porosity medium exhibited a larger region of stability, a significantly diminished collapse area, and a marginally increased fracturing area. Levasseur et al. (2010) proposed an HM model capturing permeability evolution. A corresponding FEM formulation was developed by Levasseur et al. (2010), and they numerically investigated the HM coupling effects on the performance of an underground excavation at Mont Terri Rock Laboratory.

Nair et al. (2005) applied the FEM to obtain the solution of the governing equations for fully coupled two-phase (i.e., oil and gas) flow problems in porous media. The solid deformations and fluid pressures were treated as the primary unknowns while the saturations were the secondary unknowns obtained from the capillary pressure–saturation relations. The model of Nair et al. (2005) is then verified against the analytical solutions of Ekbote et al. (2004).

Gomar et al. (2016) introduced a novel approach to model changes in fracture permeability during drilling in fractured rocks. The method of Gomar et al. (2016) combines the FEM for fully coupled thermo-poroelastic analysis of stress distribution around the borehole with the displacement discontinuity method to model fracture deformation. Their approach demonstrated that the maximum variation in aperture occurs near the borehole and diminishes significantly at greater distances from the borehole. Gomar et al. (2016) observed that mechanical stresses resulting from rock excavation have a short-term impact, while fluid pressure and thermal stresses play a more significant role in long-term permeability changes in fractures. Gomar et al. (2016) also found that fracture permeability decreases as the fracture and rock matrix deplete, while it increases with pressurization and cooling of the fracture; fracture permeability initially decreases during a balanced fluid pressure condition within a short period, but then increases due to cooling of the surrounding rock near the borehole. Li et al. (2019) introduced HM solutions to forecast the occurrence of progressive breakouts in deviated wellbores. The approach of the study of Li et al. (2019) comprises two key components. Initially, a coordinate transformation was employed to determine the stress tensor on a cross-sectional plane perpendicular to the wellbore axis. Subsequently, this stress tensor was utilized in an

ABAQUS finite element model of the borehole to simulate breakouts on the identified cross-sectional plane. Li et al. (2022) conducted a comprehensive analysis of wellbore stability in the No. 11 fault belt located in the Shunbei field, northwest of the Tarim Basin in China. The study of Li et al. (2022) focused on a target zone situated at a depth exceeding 7500 m. An integrated geomechanical investigation was performed, incorporating geological, seismic, logging, and drilling data. Through the analysis of Li et al. (2022), the estimates for pore pressure, collapse pressure, and fracture pressure of the well were obtained. Additionally, a fracture development index was calculated to identify zones with concentrated fracture distribution.

2.6. Simulation applications

2.6.1. MOOSE

MOOSE, which stands for "Multiphysics Object-Oriented Simulation Environment," is a parallel computational framework designed to solve coupled systems of nonlinear equations. Developed by Gaston et al. (2009), MOOSE provides a flexible and efficient platform for modeling and simulating a wide range of multiphysics problems. The primary motivation behind the development of MOOSE was to address the increasing complexity of scientific and engineering simulations, which often involve multiple physical phenomena interacting with each other. Traditional simulation codes were limited in their ability to handle such coupled systems, leading to inefficiencies and difficulties in achieving accurate results. MOOSE aims to overcome these challenges by offering a unified framework that facilitates the integration of different physics modules and enables efficient parallel computations. At its core, MOOSE is built upon an object-oriented design philosophy, allowing for modularity, extensibility, and code reuse. It provides a comprehensive set of tools and libraries for discretizing equations, solving nonlinear systems, and managing data (Gaston et al., 2009). One of the key features of MOOSE is its parallel computing capabilities. It utilizes high-performance computing architectures to distribute the computational workload across multiple processors or computing nodes, enabling simulations to be performed efficiently on large-scale systems. This parallelization capability makes MOOSE particularly suitable for tackling computationally

demanding problems that require significant computational resources. MOOSE incorporates a sophisticated time-stepping scheme that allows for adaptive time integration, ensuring efficient and accurate simulations. It also provides robust nonlinear solvers capable of handling highly nonlinear systems of equations. Additionally, MOOSE offers advanced meshing capabilities, including adaptive mesh refinement, which can enhance the accuracy and efficiency of simulations by dynamically adjusting the mesh resolution based on the solution's needs. The MOOSE framework has been successfully applied to a wide range of scientific and engineering applications. Its flexibility and versatility make it an attractive choice for researchers and engineers working on multiphysics problems, as it allows for solid integration of different physics modules and enables comprehensive analysis of complex phenomena. In this thesis, all the FEM numerical simulations were performed using a MOOSE environment. The open-source codes which work based on MOOSE will be explained in sections 2.6.2 and 2.6.3.

2.6.2. GOLEM; THM application for fractured media

Cacace and Jacquey (2017) proposed the theory and numerical implementation for modeling coupled fluid flow and heat transfer in faulted geological formations. In the simulator of Cacace and Jacquey (2017) named GOLEM which is a MOOSE-based application, zero-thickness lower dimensional elements representing faults are used. As shown in Figure 2.3, the 0D vertex represents point-like sources, the 1D edge represents well paths, and the 2D face represents fractures and faults within the 3D element which is a porous matrix.

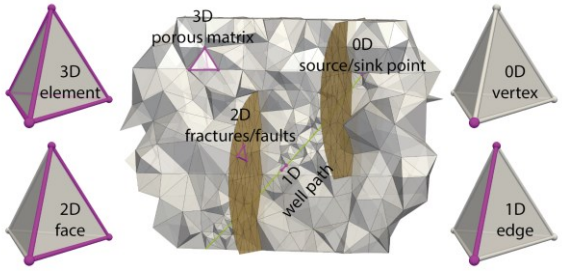

Fig. 2.3. Sketch representation of the fracture and rock masses as based on a superposition of lower- and higher-dimensional geometric elements (Cacace and Jacquey 2017)

Figure 2.4 depicts a reference case adapted from the work of Cacace and Jacquey (2017). The example showcases a situation of steady-state fluid flow in a two-dimensional porous medium section with an embedded fracture. To establish a constant and uniform flow, a discharge is applied at the left boundary within the domain. The fracture is assumed to extend infinitely in a direction perpendicular to the plane, while its length along the plane is finite. The fracture's midpoint is precisely positioned at the center of the domain. It possesses a variable width along its length and is inclined to the boundary of the model.

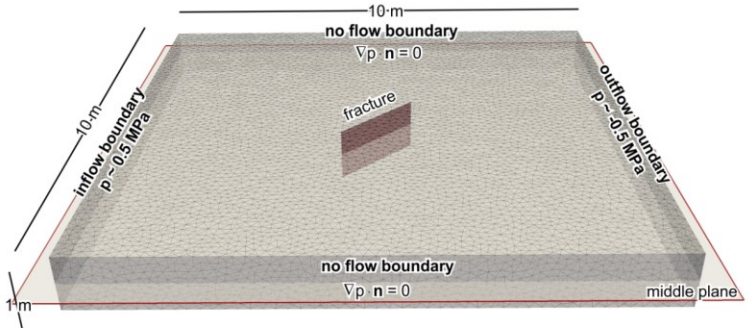

Fig. 2.4. Sketch showing the geometry and boundary conditions for the benchmark case of groundwater flow in a fractured porous medium **(**Cacace and Jacquey 2017)

The obtained numerical results by Cacace and Jacquey (2017) for the three-dimensional problem by solving a steady-state flow problem within the matrix-fracture domain can be seen in Figure 2.5. The presence of the discrete fracture disrupts the uniform horizontal flow in the vicinity of the fracture, distorting the isolines of constant pressure. This leads to a faster flow aligned parallel to the fracture plane. The computed pore pressure along a diagonal cross-section of the model domain with the analytical solution was plotted. The comparison demonstrates a perfect match between the two results, validating the reliability and implementation of the discrete fracture approach in the formulation of Cacace and Jacquey (2017) which was implemented in GOLEM**.**

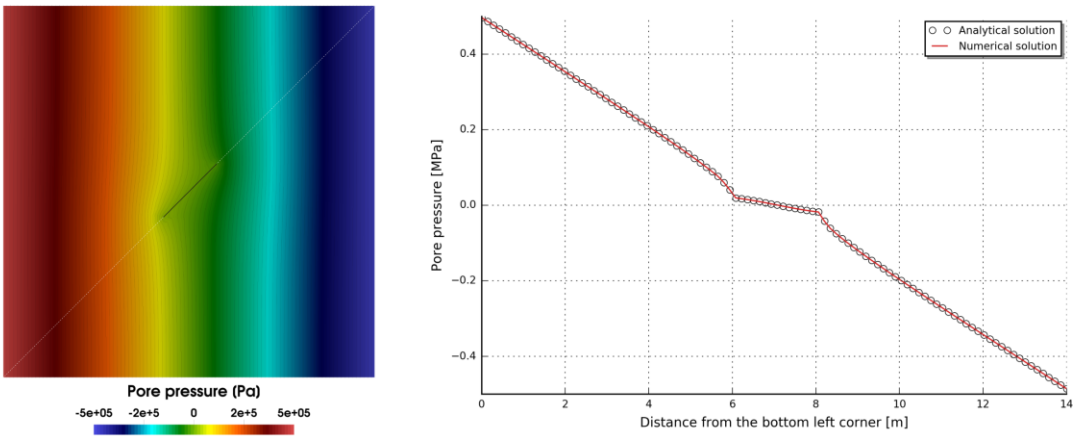

Fig. 2.5. Left: Contours of pressure from the numerical simulation by GOLEM. Right: comparison between simulated (continuous red curve) and analytical solution (black circles) pressure distribution along a line through the model (Cacace and Jacquey 2017)

2.6.3. LEMUR; muLtiphysics of gEomaterials using MUltiscale Rheologies

As explained in section 2.3.1; under differential loads, porous rocks can undergo deformation and failure through shear localized deformation or cataclastic flow. The sensitivity of these deformation mechanisms to external loading conditions, such as applied effective pressure, temperature, strain rate, and the presence of fluids, varies significantly (Jacquey et al., 2021; Jacquey and Regenauer-Lieb 2021). Most of the understanding of rock deformation and its transition from compaction to dilation under applied loads comes from laboratory experiments conducted under controlled conditions (Baud et al., 2006; Vajdova et al., 2004). Jacquey and Regenauer-Lieb (2021) expanded the thermomechanics theory to incorporate poromechanics based on path and rate-dependent critical state line models. Their thermodynamically consistent model holds relevance for civil engineering and geological applications. Additionally, Jacquey et al. (2021) further extended the thermomechanics theory to include poromechanics in geomaterials, aligning with the theory of poroelasticity and accounting for dissipative inelastic processes. Through experimental data, Jacquey et al. (2021) demonstrated how the derived thermodynamically consistent model which was implemented in a MOOSE-based application named LEMUR; can capture the macroscopic mechanical and porous responses in triaxial loading experiments. Their focus was particularly on the transition from dilation to compression

under confining pressure and the resulting localization patterns, which can range from shear dilation to compaction bands. Figure 2.6 illustrates the simulation of drained triaxial loading experiments at different confining pressures performed by Jacquey et al. (2021).

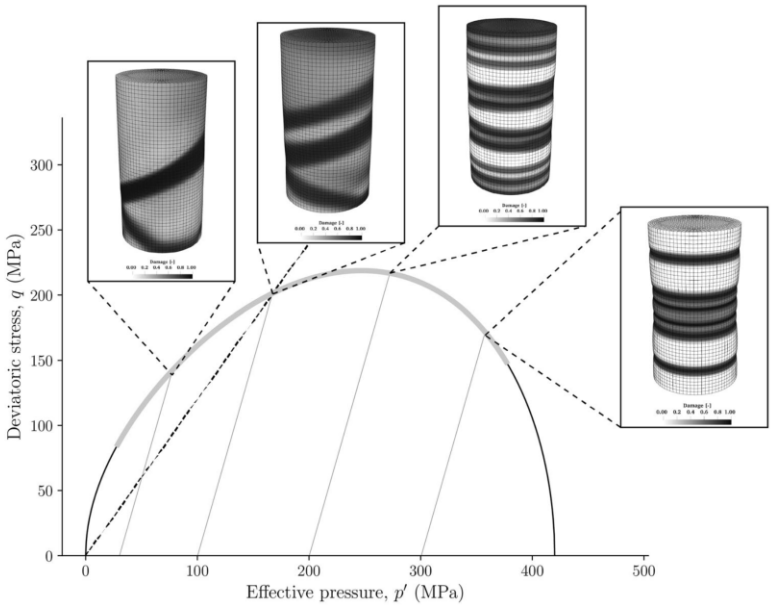

Fig. 2.6. Yield function for the Bentheim sandstone together with simulation results of triaxial tests of different stress levels: Localization illustrated by the distribution of the damage intensity variables (Jacquey et al. 2021).

In Figure 2.6, triaxial loading paths are illustrated as gray lines together with the yield function. The thick gray line on the yield function indicates where the model predicts strain localization. Colors are employed along the yield surface to highlight the loading paths that result in localized deformation within the sample, distinguishing between shear dilation and compaction. As shown in Figure 2.6, at higher differential stress, the samples undergo more compaction deformation. Figure 2.7 illustrates two triaxial loading paths: one in the dilation regime with a confining pressure of 40 MPa, and the other in the compaction regime with a confining pressure of 260 MPa. These simulations represent the extreme cases observed in laboratory experiments. The simulation results are compared to experimental data from Baud et al. (2006) showing a generally good agreement. The damage variable distribution demonstrates the occurrence of two types of localization: a shear band with dilation orientation at around 45 degrees, and multiple compaction bands perpendicular to the axial loading direction.

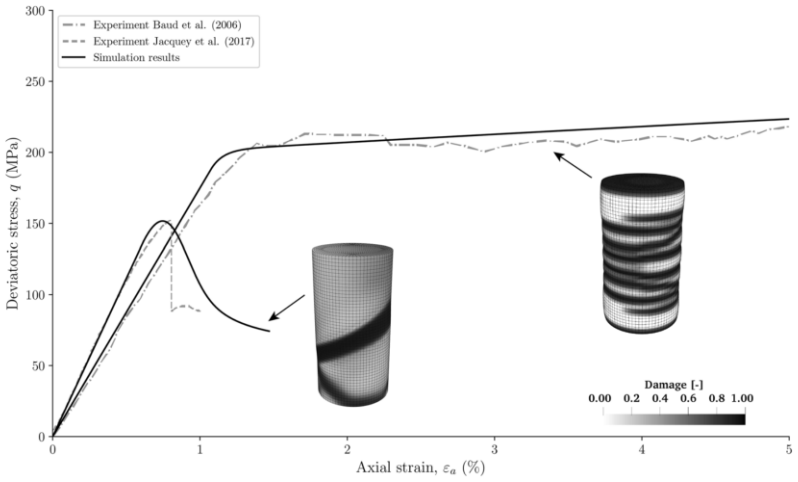

Fig. 2.7. Evolution of the deviatoric stress versus total axial strain for triaxial simulation (Jacquey et al. 2021)

2.7. Summary

Ensuring the stability of wellbores and faults is crucial for drilling and energy production. Some rocks such as Laumontite-rich rock formations pose challenges in deep geo-energy engineering due to their soft and structurally sensitive nature. Previous studies have focused on the complex stress-dependent behavior of similar materials. Limited research exists on the constitutive behavior of laumontite-rich rocks, particularly about wellbore stability design. Existing constitutive models which are used for borehole stability analysis are mostly applicable to brittle rocks and do not adequately capture the dilation behavior. Pore pressure and stress changes affect wellbore stability, especially in fractured rock formations. Accurate assessment of flow dynamics in fractures and rock matrix is important for geothermal energy production. Stress redistribution around the wellbore and plastic zone expansion must be managed for system integrity. Numerous numerical solutions for fractured media have been proposed. However, previous approaches often lack quantification of stress and pore pressure along specific fractures and neglect thermal convection.

Chapter 3

Constitutive modeling of a laumontite-rich tight rock and the application to poromechanical analysis of deeply drilled wells[†]

3.1. Abstract

Geological formations containing laumontite-rich rock are usually treated as problematic for geo-energy production projects because the presence of laumontite minerals can promote complex mechanical behaviors. Previous laboratory results indicate that rock formations with a higher laumontite content display severe stress sensitivity in poromechanical responses. With an increase in confining pressure, there is a transition from dilation to compression regime and the resulting localization styles range from shear dilation to compaction bands. In this study, we conduct finite element modeling of constitutive behaviors of rocks retrieved from the tight glutenite reservoir formation using a thermodynamic-consistent plasticity model. The shear dilation to compaction transition is well characterized. Poromechanical analysis is also conducted to analyze the plastic zone development around a borehole drilled in an over pressured reservoir. The simulated stress paths of key points around the borehole are used to demonstrate the plastic strain development processes. The impact of in-situ stress on the wellbore stability is highlighted, and a comparison with the results from using the traditional plastic constitutive model is conducted.

Keywords: laumontite-rich rock, finite element modeling, shear zone, thermomechanics-based constitutive model, hydro-mechanical coupling.

[†]A version of this manuscript has been published in *Rock Mechanics Bulletin* Journal (2023).

3.2. Introduction

In deep geo-energy engineering, rock formations containing laumontite should be given special attention as drilling or hydraulic fracturing tend to have issues in such formations (Chen et al., 2020). Laumontite is a soft mineral containing chemical water and has a chemical formula of $Ca(AlSi_2O_6)_2 \cdot 4H_2O$). Laumontite was usually formed in unconsolidated sediments with the assistance of alkaline interstitial solutions. Through silicate diagenesis processes, laumontite can be transferred into other zeolite type of minerals (Bravo et al., 2017; Vernik, 1990; Zhang et al., 2016). It can occur as fracture infills or as a replacement mineral of plagioclase within a rock formation (Morrow and Byerlee, 1991; Solum et al., 2003), thus laumontite plays an important role in crustal fault zones (Baik et al., 2009; Evans and Chester, 1995; Vernik and Nur, 1992). Previous experimental data have indicated the structural sensitivity of laumontite under dry-wet cycles and pressure or temperature disturbances (Bravo et al., 2017; White et al., 2004). The geomechanical characteristics of reservoir rocks can be complex due to the presence of laumontite. Previous studies on soft mudrocks or fault gouge geomaterials, which are also abundant in chemical bound water, have documented their complex stress path-dependent mechanical behaviors (An et al., 2021; Li and Wong, 2017; Zhang et al., 2022).

Currently, there are very limited studies focusing on the constitutive behavior of laumontite-rich rocks. Some tight reservoir rocks containing laumontite (glutenite) were treated as brittle material because of the presence of a large quantity of aggregates (Chen et al., 2020). The only experimental data (from the literature) on the pressure-dependent constitutive behavior of laumontite-rich reservoir rocks is from Yang et al. (2021), which shows that the rock can display shear to compaction yield transition behaviors under an increasing confining pressure condition. A better characterization of the constitutive behavior is essential for wellbore stability analysis and hydraulic fracturing design in deep geo-energy engineering (Chen et al., 2012; Li et al., 2018a; Wu et al., 2018). The study by Chen et al. (2012) highlights the importance of considering strain hardening/softening behavior in the poromechanical analysis of wellbore stabilities. Failure functions with multi-yield surfaces are usually considered in modeling complex constitutive behavior (Abaqus, 2016). However, a challenging aspect of such an approach is how the intersection

of multiple yield functions is handled in the numerical implementation. Previous constitutive models on confining pressure-dependent stress-strain rock behaviors are mostly applicable for brittle rocks and the attention is mainly focused on the transition of tensile or shear failure mechanisms (Mukherjee et al., 2017; Zhu and Shao, 2017). In addition, to fulfill the second law of thermodynamics, most constitutive models consider an associate flow rule, which overestimates the dilation behavior in simulating volumetric strains of geomaterials with strong heterogeneity in particle sizes (Jiang and Xie, 2011; Puzrin, 2012; Vermeer and De Borst, 1984; Zhu and Arson, 2014). In recent years, the plastic damage model has also been well considered in the thermodynamic framework to account for the damage evolution process in post-peak brittle–ductile characteristics (Zheng et al., 2022a, 2022b). Another approach is to consider a constitutive model derived from a thermodynamic-consistent physical framework to capture the macroscopic evolution of deformation whether within dilation-enhanced brittle conditions or compaction-induced ductile conditions (Jacquey et al., 2021; Jacquey and Regenauer-Lieb, 2021).

In this study, we present the petrophysical and geomechanical characterization of a laumontite-rich tight rock with cores retrieved from a deep over-pressured petroleum reservoir. Using a thermomechanics-based viscoplastic (VP) model, we capture the confining pressure-dependent constitutive behavior based on finite element modeling. We also extend the application to the poromechanical analysis of deeply drilled wells in an over pressured reservoir.

3.3. Constitutive model and governing equations for poromechanical analysis

3.3.1. A thermomechanics-based viscoplastic model

A new thermomechanics-based viscoplastic model proposed by Jacquey and Regenauer-Lieb (2021) is used herein to carry out the constitutive modeling of the deformation of laumontite-rich tight rock. The model is based on a thermodynamic-consistent physical framework and incorporates poromechanics of path- and rate-dependent critical state line models. Before the introduction of the yield function and flow rule, we first introduce fundamental quantities of the constitutive model. For a

hydromechanical coupled analysis, the negative or positive signs of stress and strain variables are usually expressed according to the convention of solid mechanics (tension is treated as positive). However, to be more comprehensive to display the internal variables (e.g., pre-consolidation stress and volumetric plastic strain) which are essential for describing the yield function and plastic flow behaviors, we use the following expressions to show the basic stress and strain invariants based on a triaxial setting:

$$p' = -\frac{\sigma'_{kk}}{3} \tag{3.1a}$$

$$q = \sqrt{\frac{3}{2}\tau : \tau} \tag{3.1b}$$

where p' are the effective stress (compression is treated as positive) and q the deviatoric stress (always positive by definition).

In Equation 3.1b the deviatoric stress tensor τ is given as:

$$\tau_{ij} = \sigma'_{ij} + p'\,\delta_{ij} \tag{3.2}$$

In which σ'_{ij} is the effective stress tensor, and δ_{ij} is the Kronecker delta.

The plastic volumetric strain ε_v^p (positive in compression), and the deviatoric or shear strain γ are expressed by:

$$\dot{\varepsilon}_v^p = -\dot{\varepsilon}_{kk}^p \tag{3.3a}$$

$$\dot{\gamma}^p = \sqrt{\frac{2}{3}\dot{e}_{ij}^p : \dot{e}_{ij}^p} \tag{3.3b}$$

A rating form has been given in Equations 3.3 and $\dot{e}_{ij}^p = \dot{\varepsilon}_{ij}^p + \frac{1}{3}\dot{\varepsilon}_v^p\delta_{ij}$ is the deviatoric plastic strain rate tensor. According to Collins (2003), a general family of critical state line models based on the theory of thermomechanics can be generated by postulating a positive dissipation function.

An essential aspect of this approach is the derivation of the yield function in the dissipative stress space, which takes a much simpler form than in the true stress space. Furthermore, Jacquey and Regenauer-Lieb (2021) extended within the thermomechanics framework the dissipation function introduced by Collins (2003) to consider rate dependent plastic deformation while maintaining the same yield function in the dissipation stress space, which reads:

$$F = \sqrt{\frac{\pi^2}{A^2} + \frac{\chi^2}{B^2}} - 1 = 0 \tag{3.4}$$

where π is the effective dissipative stress, and χ is the dissipative deviatoric stress. This yield function consists of an ellipse of semi-axis A and B centered in $(0,0)$ in the effective dissipative stress space (π, χ). The coefficients *A* and *B* are given as:

$$A = (1-\gamma)\, p' + \frac{1}{2}\gamma p_c \tag{3.5a}$$

$$B = \mu \left| (1-\alpha)\, p' + \frac{1}{2}\alpha\gamma p_c \right| \tag{3.5b}$$

where μ is a material constant which is related to the rock's friction angle; α and γ are two dimensionless constants responsible for "dissipation coupling" and they guarantee non-associative flow rules in the true stress space. The transition from true stress space to dissipative stress space is given by:

$$p' = \rho + \pi \tag{3.6a}$$

$$q = \chi \tag{3.6b}$$

where ρ is the shift pressure which can be obtained as:

$$\rho = \frac{1}{2}\gamma p_c^0 \exp\left(\frac{\varepsilon_v^p}{\Lambda_i}\right) \tag{3.7}$$

In Equation 3.7, p_c^0 is the initial consolidation pressure, and Λ_i the plastic compressibility parameter that governs the inelastic compression or dilation behaviors.

Given the yield function expressed in Equation 3.4, the flow rules for the plastic strain invariants can be derived as:

$$\dot{\varepsilon}_v^p = \frac{\langle F \rangle}{\eta} \frac{\partial F}{\partial \pi} \tag{3.8a}$$

$$\dot{\gamma}^p = \frac{\langle F \rangle}{\eta} \frac{\partial F}{\partial \chi} \tag{3.8b}$$

The flow rules shown in Equations 3.8 are also expressed in the dissipative stress space, and a plastic strain rate vector normal to the yield function is formulated. η is a viscosity (or reference rate of dissipation) with specific units of $\text{pa}^{-1}.\text{s}$. The Macaulay brackets $\langle \bullet \rangle$ are applied to force the plastic strains to be always positive or null. As introduced in Equation 3.8, the flow rule for the plastic strain is orthogonal to the yield function in the dissipative stress space to fulfill the second law of thermodynamics. However, the flow direction is not necessarily orthogonal to the yield function in the true stress space, thus the use of dissipative stress can induce non-associative flow rules and therefore can better characterize the dilatancy behavior.

For viscoplastic constitutive laws, the yield function is first evaluated using trial effective stress. If the yield function is positive, the following residuals in Equations 3.9 are used to solve for an acceptable value for the plastic strain rate tensor.

$$R_v\left(\dot{\varepsilon}^p, \dot{\gamma}^p\right) = \langle F \rangle \frac{\partial F}{\partial \pi} - \eta \dot{\varepsilon}_v^p = 0 \tag{3.9a}$$

$$R_d\left(\dot{\varepsilon}^p, \dot{\gamma}^p\right) = \langle F \rangle \frac{\partial F}{\partial \chi} - \eta \dot{\gamma}^p = 0 \tag{3.9b}$$

The increments of plastic strain rates are obtained by differentiating Equations 3.9 and using Newton-Raphson iterations (noted $i + 1$):

$$\frac{\partial R_v^{(i)}}{\partial \dot{\varepsilon}_v^p}\delta\dot{\varepsilon}_v^{p(i+1)} + \frac{\partial R_v^{(i)}}{\partial \dot{\gamma}^p}\delta\dot{\gamma}^{p(i+1)} = R_v^{(i)} \tag{3.10a}$$

$$\frac{\partial R_d^{(i)}}{\partial \dot{\varepsilon}_v^p}\delta\dot{\varepsilon}_v^{p(i+1)} + \frac{\partial R_d^{(i)}}{\partial \dot{\gamma}^p}\delta\dot{\gamma}^{p(i+1)} = R_d^{(i)} \tag{3.10b}$$

with the increments obtained, the plastic strain rates are updated at each iteration provided that the residuals R_v and R_d reach a tolerance value.

$$\dot{\varepsilon}_v^{p(i+1)} = \dot{\varepsilon}_v^{p(i)} + \delta\dot{\varepsilon}_v^{p(i+1)} \tag{3.11a}$$

$$\dot{\gamma}^{p(i+1)} = \dot{\gamma}^{p(i)} + \delta\dot{\gamma}^{p(i+1)} \tag{3.11b}$$

The procedure to update the effective stress tensor for viscoplastic constitutive laws is summarized in Box 3.1.

1 Set $i = 0,\ \dot{\varepsilon}_v^p = 0,\ \dot{\gamma}^p = 0,\ R_v^{(0)} = R_v(0,0),\ R_d^{(0)} = R_d(0,0)$;

2 **While** $i \le i_{\max}$ **do**

3 **While** $\sqrt{R_v^{(i)2} + R_d^{(i)2}} > tol$ **do**

4 Compute $\delta\dot{\varepsilon}_v^{p(i+1)}$, and $\delta\dot{\gamma}^{p(i+1)} \rightarrow$ Eq.10

5 Update strain rates $\dot{\varepsilon}_v^{p(i+1)}$, and $\dot{\gamma}^{p(i+1)} \rightarrow$ Eq.11

6 Update residuals:

7 $R_v^{(i+1)} = R_v\left(\dot{\varepsilon}_v^{p(i+1)}, \dot{\gamma}^{p(i+1)}\right)$;
$R_d^{(i+1)} = R_d\left(\dot{\varepsilon}_v^{p(i+1)}, \dot{\gamma}^{p(i+1)}\right)$;

8 **End**

9 $i = i + 1$;

10 **End**

Box 3.1. Summary of the algorithm to update the stress for visco-plastic constitutive law, modified after Jacquey et al. (2021).

3.3.2. Poromechanical analysis

For a fully saturated rock, **t**he poromechanical behavior can be generally described using theories of poroelasticity (Biot, 1956). Jacquey et al. (2021) extended a modular thermomechanics approach to include rate-dependent critical state line constitutive models for hydro-mechanical coupling as relevant for porous media. The partial differential equations for the mechanical response of the skeleton and the evolution of the fluid pressure can be given as:

$$\nabla_j \cdot \left(\sigma'_{ij} - \alpha_B p_f \delta_{ij} \right) = 0 \tag{3.12}$$

$$\frac{1}{M_b} \frac{\partial p_f}{\partial t} + \alpha_B \frac{\partial \varepsilon_{kk}}{\partial t} + \left(1 - \alpha_B\right) \frac{\partial \varepsilon_{kk}^p}{\partial t} + \nabla \cdot \mathbf{q}_f = 0 \tag{3.13}$$

In Equations 3.12 and, 3.13 Biot's poroelastic coefficient α_B and Biot's modulus M_b are given as:

$$\alpha_B = 1 - \frac{K}{K_s} \tag{3.14}$$

$$\frac{1}{M_b} = \frac{n}{K_f} + \frac{\left(\alpha_B - n\right)}{K_s} \tag{3.15}$$

where p_f is the pore fluid pressure, n is the porosity, K is the drained bulk modulus of the rock with K_s the solid bulk modulus, and K_f the fluid bulk modulus. $\mathbf{q}_f$ is the Darcy velocity defined via the intrinsic permeability k and the fluid viscosity μ_f as:

$$\mathbf{q}_f = -\frac{k}{\mu_f} \nabla \cdot p_f \tag{3.16}$$

ε_{kk} is the total volumetric strain and ε_{kk}^p is the plastic strain component of the volumetric strain.

The balance of porosity, n can be further obtained as:

$$\frac{\partial n}{\partial t}-\left(\alpha_B-n\right)\left(\frac{1}{K_s}\frac{\partial p_f}{\partial t}+\frac{\partial \varepsilon_{kk}}{\partial t}\right)-\left(1-\alpha_B\right)\frac{\partial \varepsilon_{kk}^p}{\partial t}=0 \tag{3.17}$$

3.4. Laboratory characterizations and constitutive modeling

3.4.1. Laboratory characterizations

The laumontite-rich tight rock (glutenite) cores used in this study were collected from a vertical well located in Xinjiang oilfield, China. The formation has a buried depth of more than 4000 meters. Petrophysical and mineralogical tests are conducted on cores to obtain the mineralogical compositions, porosity, and pore structure characteristics. Triaxial tests are conducted on some samples to investigate the mechanical responses under different confining pressures and drained stress path conditions. As shown in Figure 3.1, laumontite-rich glutenite samples drilled from the target formation are loose and fragile with poor sorting. Cylindrical samples (25 mm in diameter and 50 mm in length) were retrieved from raw cores using a wire cutting machine. In order to characterize the mineralogy compositions of studying laumontite-rich tight rock samples, we also carried out X-ray powder diffraction (XRD) analysis on collected specimens. The results of XRD are included in Table 3.1, which indicates that laumontite, quartz, and feldspar are the dominant minerals. There are also some clay minerals and calcite, where most of the clay minerals are composed of swelling clay (I/S, illite/smectite mixture). The scanning electron microscope (SEM) analysis was also conducted and is displayed in Figure 3.1. The result indicates that the high laumontite content glutenite has a plate-like mineral structure of laumontite surrounded by the illite/smectite mixture. The Micro-CT image shows that pore space is mainly aligned around large aggregates. We also conducted the porosity measurement using N2 gas according to the approach of Boyle's law. In average, the studied rock has a porosity of 11.5%. But it should be noted that the chemical bound water takes up a certain amount of the pore space, thus the rock is treated as tight.

Triaxial compression tests on the rock samples were conducted by Yang et al. (2021) to investigate the geomechanical properties under different confining pressures. All

the tested samples were loaded under a drained stress path condition, where drainage was provided on the bottom and top ends of the cylindrical sample. Local displacement transducers were applied to measure the axial and radial strains. Confining pressures (σ_C) of 20, 35, 50, 65, and 80 MPa were applied to different samples to investigate the stress-strain behaviors. Detailed information on the strength and deformation behavior will be elaborated along with simulated results in the subsequent section.

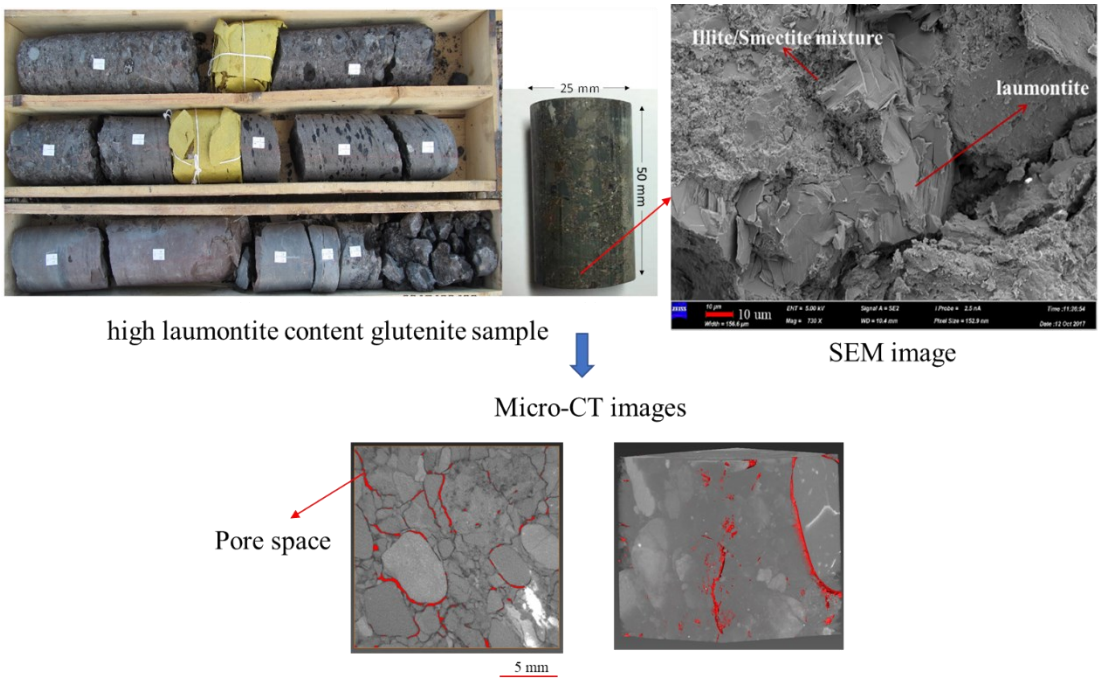

Fig. 3.1. Laumontite-rich tight rock cores were used in this study along with the SEM image showing dominant minerals and micro-CT images showing pore structure.

Table 3.1. Mineralogy composition and porosity data of glutenite samples (average values are given for samples from the same well).

Sampling Depth (m)	Mineralogy composition by weight (%)					Porosity (%)
	Clay	Quartz	Feldspar	Calcite	Laumontite	
4000-4007	3.32	31.66	13.2	1.2	50.62	11.5

3.4.2. Triaxial test simulation and calibration

We collected the experimental data from Yang et al. (2021) and found out that samples display shear to compaction yield transition behaviors under an increasing confining pressure condition. By mapping the critical stress data in the stress space, we were able to gain information on the initial yield stresses based on the thermodynamic-based viscoplastic model presented previously. The results of studying laumontite-rich samples are shown in Figure 3.2 where we illustrate the initial yield stress in the true stress space as derived from the critical stress at the onset of shear-enhanced compaction as published by Yang et al. (2021). The measured points shown in Figure 3.2 correspond to the yield strengths beyond which volumetric strain starts going toward dilation. The fitted parameters of the yield function displayed in Figure 3.2 are included in Table 3.2.

Table 3.2. Derived key parameters for the thermomechanics-based viscoplastic model based on triaxial test results.

Parameters	Values	Units
Initial critical pressure, p_c^0	150	MPa
μ	1.25	-
α	0.45	-
γ	0.9	-

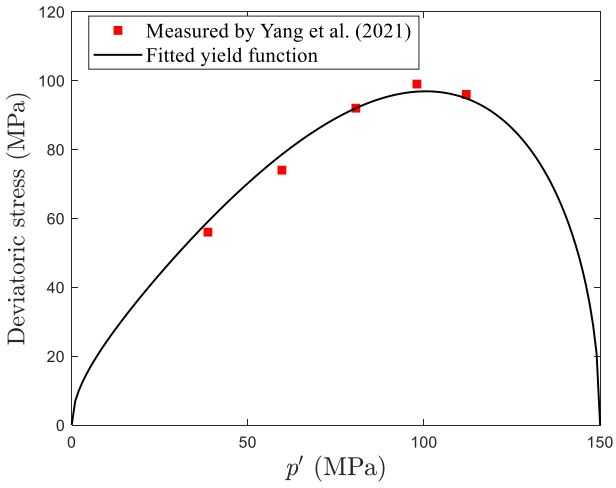

Fig. 3.2. Measured failure points and the fitted thermomechanics-based viscoplastic yield function of the laumontite rich rock based on triaxial test results.

For simulating the deformation behavior of laumontite-rich samples under triaxial loading conditions, we make use of an open-source finite element method (FEM) numerical package called LEMUR (Jacquey et al. 2021) which includes an implementation of the the thermomechanics-based viscoplastic model introduced in section 3.2. LEMUR was developed based on a high performance open-source FEM package with the Multi-physics Object Oriented Simulation Environment (MOOSE). Same to the laboratory tests by Yang et al. (2021), samples for the numerical tests also have a diameter of 25 mm and a height of 50 mm. The distribution of 3D mesh and the prescribed boundary conditions are illustrated in Figure 3.3. The cylinder geometry is discretized into 3500 hexahedra elements. The poroelastic and viscoplastic properties considered for triaxial calibration can be found in Table 3.3. A constant confining pressure is imposed on the vertical faces in the radial direction. The vertical displacement is fixed on the bottom face of the cylinder while the lateral displacements are fixed on two points on the bottom face to avoid rotation of the cylinder. The axial loading is modeled by imposing a constant downward velocity on the top face. The axial strain rate $\dot{\varepsilon}_a = 10^{-6}\,\mathrm{s}^{-1}$ was applied for all models. Fluid pressure is held at zero on the top and bottom faces to reproduce drained conditions.

Figure 3.4 shows the simulation results of deviatoric stress and volumetric strain under drained triaxial loading conditions at different confining pressures. As shown in Figure 3.4a for samples at confining pressures below 50 MPa the stress softening occurs after the peak strength, which indicates a brittle failure. Meanwhile, according to the volumetric axial strain curves presented in Figure 3.4b, there is an apparent deflection of volumetric strain after entering the yield stage. After the peak strength, the volumetric strain decreases in the opposite direction as the axial strain increases, and shear dilation occurs. Under high confining pressure (above 50 MPa), the amplitude of stress increasing with axial strain decreases after the yield point, which indicates the characteristics of stress hardening. The volumetric strain of rock continues to increase after the yield point, and shear-enhanced compaction occurs.

Generally, the simulated deviatoric stress vs. axial strain relations match well with the measured results. However, measured volumetric strain vs. axial strain relations are not well captured by our numerical tests (Figure 3.4b). The compaction/dilation trend can be

reproduced but the difference is more significant for cases with high confining pressures. During yield and failure processes, localization occurs within the rock samples. The dilation angle is known to be dependent on the particle size and in-homogeneity nature of disturbed samples. The present constitutive model focuses on the overall mechanical behavior of the simulated rocks from the macroscopic perspective; thus, a constant dilation angle is used in the simulation. For that reason, the changes in volumetric strain during the post-peak softening stage cannot be well characterized which can explain the discrepancies between modeling and experimental results. It is necessary to carry out micro-mechanical analysis in the mineral particle scale to understand the role of mineral geometry and heterogeneity on the overall rock mechanical behavior. Future work should focus on improving the current modeling approach when more experimental data are available for validations.

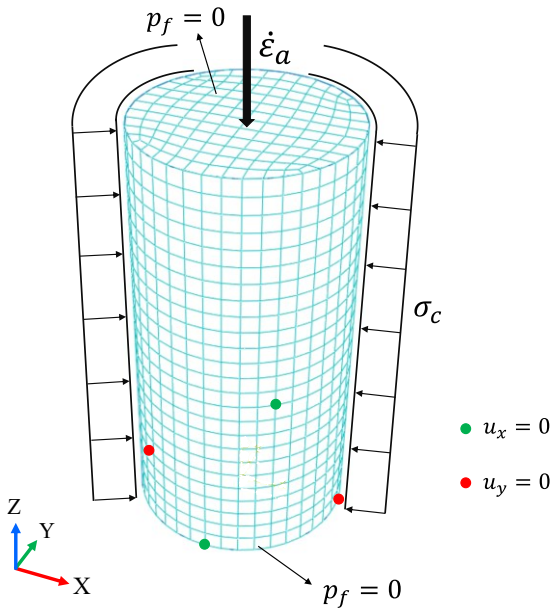

Fig. 3.3. Sketch showing the 3D finite element mesh along with the boundary conditions for the triaxial numerical test.

Table 3.3. Poroelastic and viscoplastic parameters of laumontite rich rock samples used for triaxial numerical tests.

Parameters		Symbols	Values	Units
Young's modulus		E	12.6	GPa
Permeability		k	9.87×10^{-16}	m^2
Fluid bulk modulus		K_f	2	GPa
Fluid viscosity		μ_f	1×10^{-3}	Pa.s
Solid modulus		K_s	35	GPa
Porosity		n	0.11	-
Poisson's ratio		ν	0.2	-
Biot coefficient		α_B	0.8	
Plastic viscosity		η	2×10^{-5}	$Pa^{-1}.s$
Plastic compressibilities	Dilation	Λ_d	1×10^{-3}	-
	Compression	Λ_c	2×10^{-2}	

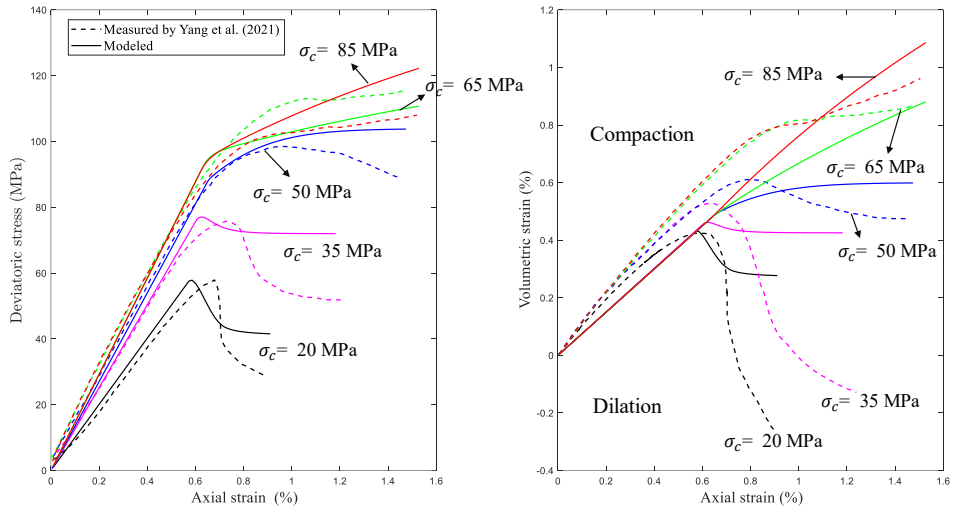

Fig. 3.4. Plots of measured and modeled (a) deviatoric stress and (b) volumetric strain versus axial strain for the laumontite rich rock samples under different confining pressures.

3.5. Poromechanical analysis of boreholes drilled in an over pressured reservoir

With the triaxial numerical test results, we proceed to conduct finite element numerical analysis of wellbores drilled in an over pressured reservoir, where laumontite-rich tight rocks are present. The poromechanical modeling is also based on the FEM package LEMUR. The numerical model is firstly validated using the available analytical solution for poroelastic analysis of boreholes drilled in a saturated porous media. Subsequently, plastic models are included to quantify the plastic yielding processes.

3.5.1. Validation with analytical solution

The poromechanics/poroelastic analytical solution for stress and pore pressure distribution induced by the drilling in a saturated porous media, was presented by Abousleiman and Nguyen (2005). The analytical solutions were developed within the framework of the coupled processes for both single porosity and double porosity media which accounts for coupled isothermal fluid flow and rock/fractures deformation. The pore pressure field near the borehole is perturbed by the excavation. Fluid diffusion leads to a

time-dependent redistribution of total and effective stresses. The plane-strain borehole problem can be decomposed into three individual problems: elastic, diffusion, and poroelastic deviatoric stress loading problems (Cui et al., 1997). The complete solutions are obtained by superposition of the three individual problem solutions following the decomposition of boundary conditions. The solution of mode 1 is purely elastic. Mode 2 is an uncoupled diffusion problem for pore pressure which is time-dependent, whereas the solution of mode 3 involves a full poroelastic coupling.

The analytical solutions for a wellbore drilled in an infinite poroelastic medium, subjected to a three-dimensional in situ state of stress and pore pressure are given as the following:

$$p_f = p_o + p_f^{(2)} + p_f^{(3)} \tag{3.18}$$

$$\sigma_{rr} = \sigma_m - \sigma_d \cos(2\theta) - \sigma_{rr}^{(1)} - \sigma_{rr}^{(2)} - \sigma_{rr}^{(3)} \tag{3.19}$$

$$\sigma_{\theta\theta} = \sigma_m + \sigma_d \cos(2\theta) - \sigma_{\theta\theta}^{(1)} - \sigma_{\theta\theta}^{(2)} - \sigma_{\theta\theta}^{(3)} \tag{3.20}$$

$$\sigma_{zz} = \sigma_V - 2v\sigma_m + v(\sigma_{rr} + \sigma_{\theta\theta}) + \alpha_B (1-2v)\left(p_f^{(2)} + p_f^{(3)}\right) \tag{3.21}$$

The solution of stress tensors in terms of cylindrical $\sigma_{rr}^{(1)}, \sigma_{rr}^{(2)}, \sigma_{rr}^{(3)}, \sigma_{\theta\theta}^{(1)}, \sigma_{\theta\theta}^{(2)}, \sigma_{\theta\theta}^{(3)}$ polar coordinates and pore pressures $p_f^{(2)}$, and $p_f^{(3)}$ are given in the Laplace domain and presented in the Appendix. The superscripts (1), (2), and (3) represent the solutions of the three loading modes of the modified plane strain problem. R is the radius of the well, r and θ are radial coordinates in the wellbore local coordinate. p_o denotes the original formation pore pressure before excavation. σ_H is the maximum horizontal stress, σ_h the minimum horizontal stress, and σ_V is the vertical stress. At the far field, when $r \to \infty$, the boundary conditions can be assumed around the domain as shown in Figure 3.5.

The terms of σ_m, and σ_d are given as:

$$\sigma_m = \frac{\sigma_H + \sigma_h}{2} \tag{3.22a}$$

$$\sigma_d = \frac{\sigma_H - \sigma_h}{2} \tag{3.22b}$$

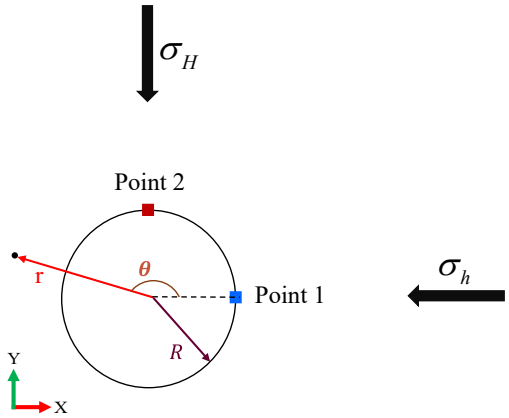

Fig. 3.5. Sketch showing in-situ stress directions along with the two monitoring points.

The prescribed boundary conditions and the domain size considered for the FEM numerical simulations are shown in Figure 3.6.

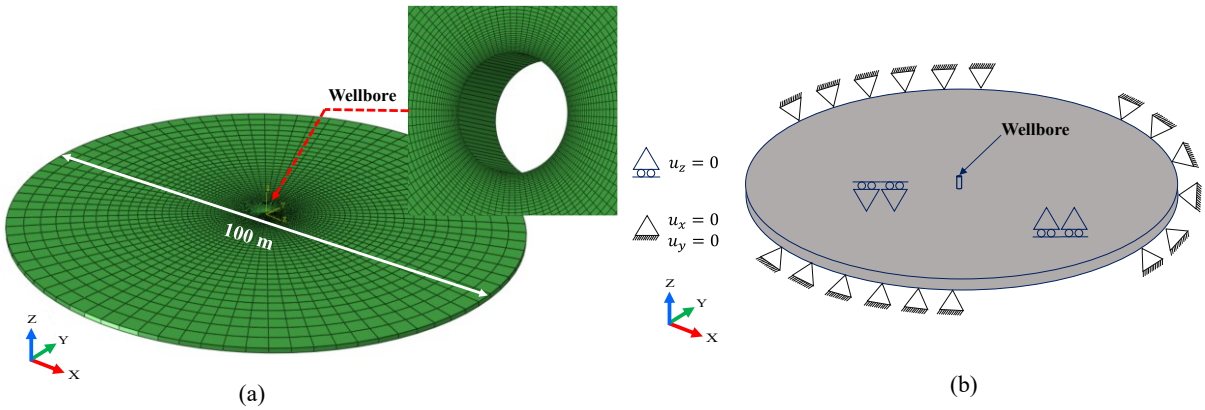

Fig. 3.6. Sketch showing (a) 3D mesh distribution and (b) boundary conditions for borehole stability analysis.

The depth of the wellbore was assumed to be 4500 m. The in-situ stresses and the wellbore geometry data are included in Table 3.4. The formation is over-pressured with a formation pressure gradient of 0.016 MPa/m. Information of in-situ stresses and formation pore pressure are according to Chen et al. (2020). The domain size around the wellbore was assumed to be 50 m which could be sufficient to ensure the negligible effect of the

external boundaries. The mesh size is selected sufficiently small to consider detailed plastic deformation. The numerical model was first validated with 1359 kg/m^3 of mud density based on the single porosity solutions of Abousleiman and Nguyen (2005).

Table 3.4. In situ stresses and well geometry parameters of the borehole drilled in Xinjiang oilfield, China.

Parameters	Symbols	Values	Units
In situ stresses			
Vertical stress	σ_V	112.5	MPa
Maximum horizontal stress	σ_H	103.5	MPa
Minimum horizontal stress	σ_h	81	MPa
Wellbore			
Radius	R	0.216	m
Initial pore pressure	p_o	72	MPa
Mud density	ρ_w	1359	kg/m^3
Depth	-	4500	m

The solution in time is solved by a numerical inversion method (Stehfest, 1970). The time domain solutions were put into implementation using MATLAB (Heidari et al., 2021). Figure 3.7 illustrates the comparison between the analytical solutions and the corresponding pore pressure, effective radial, tangential, and vertical stresses obtained from the simulations along the radial direction when $\theta = 0$ at three different times. The agreement between the two solutions shows the convergence of the mesh size and the robustness of the FEM numerical package.

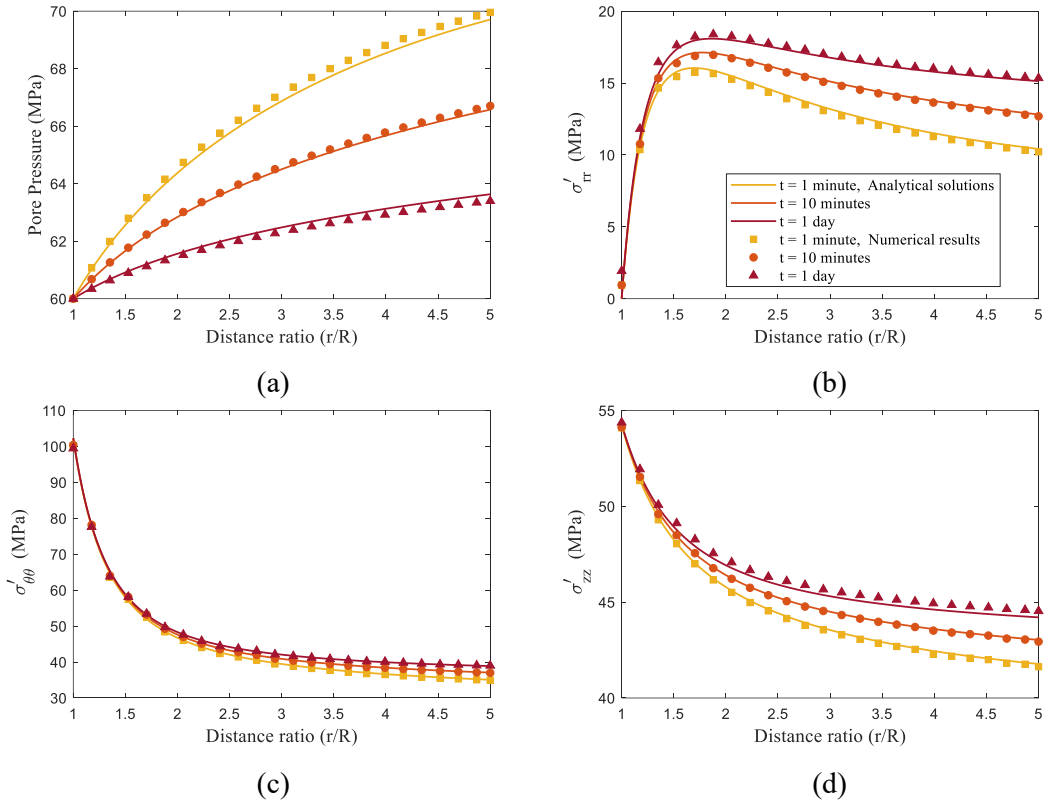

Fig. 3.7. Plots of analytical and modeled results of (a) pore pressure (b) effective radial stress (c) effective tangential stress and (d) effective vertical stress at different times.

3.5.2. Numerical modeling using the thermomechanics-based viscoplastic model

We applied the thermomechanics-based viscoplastic model in the poro-elastic-plastic analysis of the deeply drilled well. In order to investigate the impacts of hardening/softening viscoplastic model on the plastic yield zones developed around boreholes, we choose a set of cases for the borehole stability analysis. Detailed description of each model is summarized in Table 3.5. The well was analyzed under different mud pressures (with different drilling mud densities). Cases I, II, and III were chosen as initial models with three possible drilling mud densities to find out the reasonable value of the wellbore pressure. Other cases will be presented in the discussion section.

Table 3.5. Summary of inputs for different cases of wellbore poromechanical analysis.

Cases	σ_V (MPa)	σ_H (MPa)	σ_h (MPa)	ρ_w (kg/m^3)	Plasticity model*
I	112.5	103.5	81	1359	VP
II	112.5	103.5	81	1475	VP
III	112.5	103.5	81	1585	VP
IV	112.5	103.5	70	1585	VP
V	112.5	103.5	70	1585	DP

*Note: VP = thermomechanics-based viscoplastic; DP = Drucker Prager

Figure 3.8a shows the equivalent plastic strain distribution with three different fluid pressures. The results show that plastic zones are very significant in cases with mud densities of 1359 kg/m^3 and 1475 kg/m^3. Plastic zones are mainly developed around Point 1, which is in line with the direction of minimum horizontal stress (Figure 3.5). A drilling mud with a density of ρ_w = 1585 kg/m^3 yields a safe well with no significant plastic strain developed around the borehole. As is show in Figure 3.8b, the plastic yielding process for cases I and II can be illustrated by the effective stress paths of two selected monitoring points. The stress path for point 1 indicates an increase in the mean and deviatoric stresses and plastic yield is confirmed by the intersection with the yield surface. The softening stage is followed by a decrease in mean and deviatoric stresses. On the other hand, the stress path of point 2 continues to ascend towards but does not touch the failure surface. In addition, the mean effective stress for Point 2 always displays a decreasing trend.

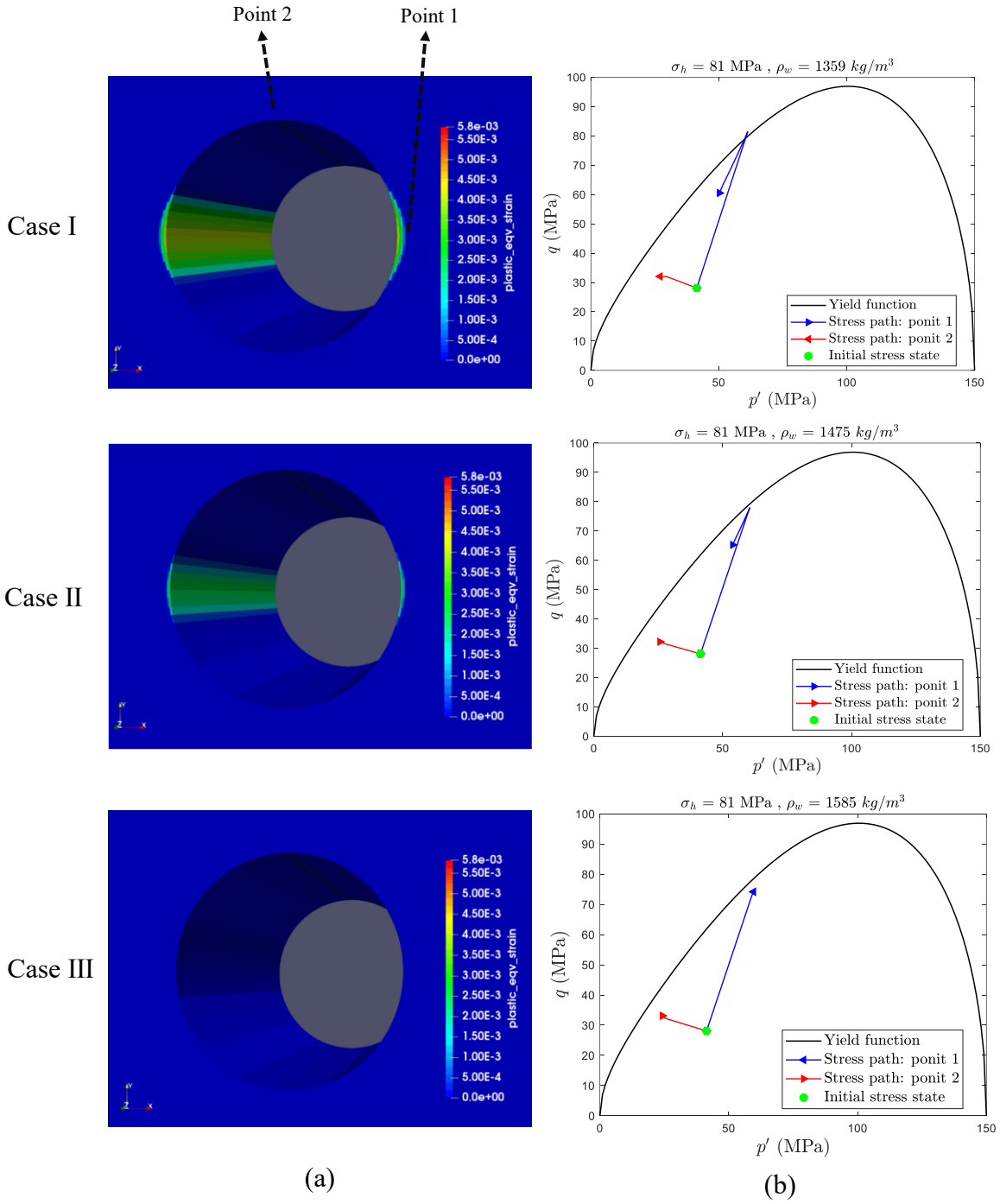

Fig. 3.8. Plots showing: (a) accumulated plastic equivalent strain at t = 2 days under different drilling fluid pressures and (b) viscoplastic failure surface, stress paths of the selected points.

3.6. Discussios

3.6.1. Impact of in situ stress

For a deep petroleum reservoir like the tight glutenite formation considered in this study, there are uncertainties in in-situ stress measurements. The variation of in-situ stress can be due to regional heterogeneity in lithology (Liu et al., 2022; Ma et al., 2022) or long-term petroleum production induced disturbance to the original in-situ stress (Chen et al., 2022). The impact of in-situ stress variation on wellbore stability was extensively studied in the literature (Abdollahipour et al., 2019; Hu et al., 2018). Shown in Table 3.5, we will consider a possible case with a different set of in-situ stress (case IV: the minimum horizontal stress is decreased from 81 to 70 MPa) to demonstrate the change in the produced plastic zone. The results of plastic zone and stress paths of key monitoring points are displayed in Figure 3.9. The transition of in situ stress is accompanied by an increase in the deviatoric part of the effective stress tensor, which leads to the development of localized plastic shear zone.

Case IV

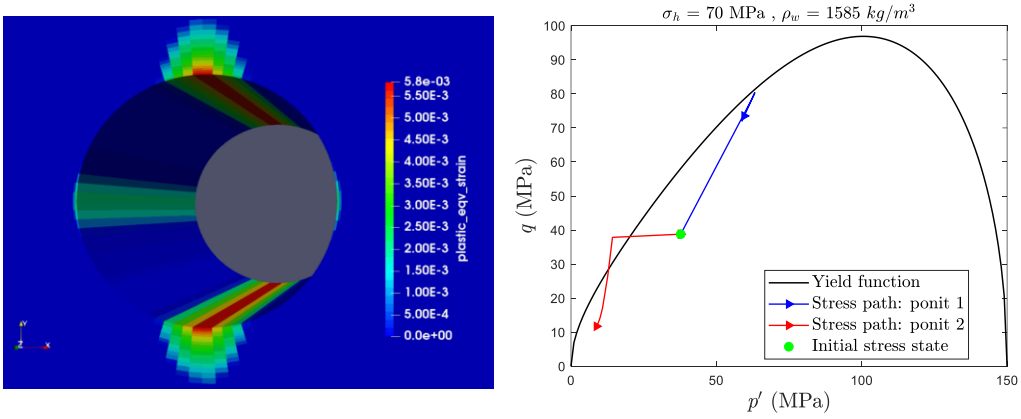

(a) (b)

Fig. 3.9. Plots showing: (a) accumulated plastic equivalent strain and (b) stress paths of the selected points for a wellbore drilled in a formation with highly anisotropic in-situ stresses.

For this case, the initial stress state is closer to the yield surface, and plastic zones are developed around both point 1 and point 2, which can be demonstrated in the stress path curves (Figure 3.9b). In particular, the zone around point 2 displays a trend of

developing tensile stress to approach the yield locus. Our simulation demonstrates the significant impact of in-situ stress on the plastic zone development around a wellbore.

3.6.2. Comparison with cases using traditional plastic model

Traditional plastic models (e.g., Drucker-Prager model and Mohr-Coulomb model) are also frequently considered in poromechanical analysis of wellbore stability (Li et al., 2018a) due to their convenience. The Drucker–Prager yield envelope is a smoother version of the classical Mohr-Coulomb failure criterion, and the parameters conversion should be carried out based on matching yielding curves in the meridian plane at different Lode angles (Drucker, 1950; Jiang and Xie, 2011; Puzrin, 2012). The Drucker–Prager yield criterion is concisely expressed as:

$$q - p' \tan\beta - d = 0 \tag{3.23}$$

where β is the rock's friction angle based on Drucker–Prager model and d is the corresponding cohesion strength.

We also have conducted numerical simulations using the previously mentioned FEM package for a case using Drucker-Prager (DP) criteria and investigated the difference in generating plastic zones (Table 3.5). After taking four tests' peak strengths, we obtained the strength parameters after displaying strength measurement in equivalent mean stress equivalent shear stress ($p' - q$ stress space) and fitting the measured results with the linear Drucker-Prager model. Before the field scale simulation, triaxial numerical tests were also conducted as a calibration to obtain critical mechanical parameters. Modeled stress-strain curves at different confining pressures are shown in Figure 3.10. For an axial strain lower than 0.6%, the samples display a linear elastic trend. The strain hardening effect is noticed when the applied stress is beyond the yield limit, which is also an indication of high plastic behavior in such high confining pressure conditions. While using the traditional Drucker-Prager, the numerical tests cannot capture the strain softening behavior. Thus, there are major differences in the stress-strain relations among measured and modeled results in the

post-peak softening stage. It should also be noted that a lower bound of strength has been selected for matching the stress-strain curves.

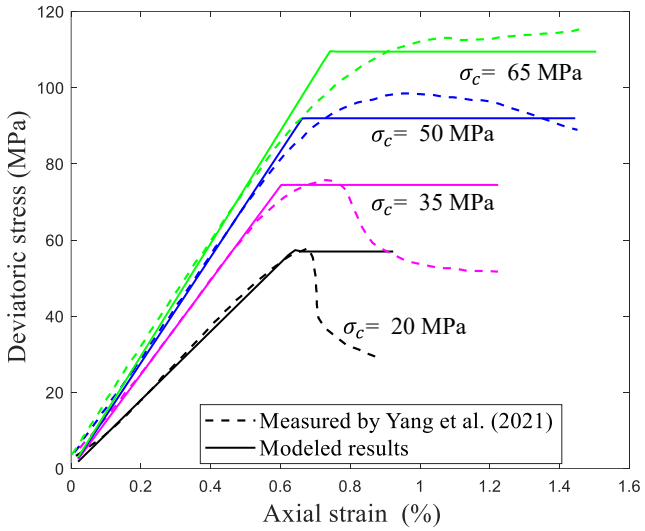

Fig. 3.10. Plots of measured and modeled deviatoric stress versus axial strain for the laumontite rich rock samples using the Drucker-Prager model.

For the field scale analysis, we carried out Case IV using DP model with same in-situ stress condition as of Case IV (Table 3.5). Similarly, the results of plastic zones and stress path curves are shown in Figure 3.11. Compared to the results from Cases IV, there are much less plastic zone developed. Even though the calibration has been conducted from a conservative side, there is still less plastic strain both in terms of magnitude and plastic zone size. In a future poromechanical analysis related to hydraulic fracturing processes, where compaction to dilation transition is more important (Chen et al. 2020), our model is potentially giving more reasonable results for fracturing design and injection optimization.

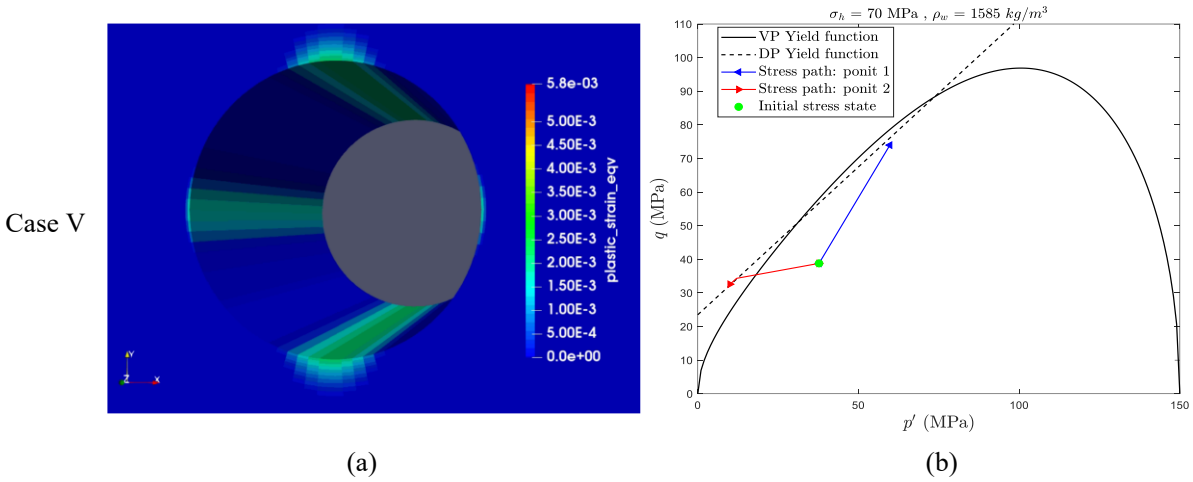

Fig. 3.11. Plots showing the simulation results by using DP model: (a) accumulated plastic equivalent strain and (b) stress paths of the selected points.

3.6.3. Advantages and limitations of the study

In the present study, the constitutive modelling is carried out based on a thermomechanics-based viscoplastic model implemented using the finite element method. The advantage is that both the laws of thermodynamics and non-associated flow rule are fulfilled. With the increase of confining pressures, the transition from shear dilation to volumetric compression can be well characterized. All the model parameters have clear physical meanings and can be conveniently obtained based on traditional triaxial tests. From the laboratory to the borehole scale, the simulation tasks can be completed in several hours using a standard desktop computer. If the modeling approach is applied to simulate regional-scale numerical analysis like basin compaction process or in-situ stress changes due to geo-energy productions, which requires a super large computing capacity, the scalability of the numerical framework will be an important asset. However, the present simulation only provides the developed plastic zone around a wellbore. The whole borehole failure process cannot be well captured. The Discrete Element based models (DEM) are also commonly used to simulate the poromechanical response of boreholes (Li and Zhang, 2022), and the micro-scale failure mechanisms can be well captured. However, DEM simulations required more calibrated parameters. There is a trade-off between FEM-based

and DEM-based modelling, and the choice of the numerical method depends on the specific demand and the goal of the analysis.

3.7. Conclusion

In this study, we applied a thermomechanics-based viscoplastic model to simulate the stress-strain characteristics of a laumontite-rich tight rock. The constitutive modeling scheme is further included in the poromechanical analysis of deeply drilled wells in an over pressured reservoir for tight oil production. Several conclusions are drawn as the following:

- Petrophysical characterizations on mineral compositions and micro-structures of the glutenite cores show that the dominant mineral is laumontite and pore space is mainly aligned around large aggregates. The highly porous and heterogeneity characteristics of the studying laumontite-rich tight rock formation contribute to its strong confining pressure dependent mechanical behaviors.
- Under a low confining pressure, the laumontite-rich tight rock displays a strain hardening followed by post-peak softening behavior. With an increase of the confining pressure, there is a transition from dilation to acompression regime. The complicated constitutive behavior can be well quantified by using the thermomechanics-based viscoplastic model, where both laws of thermodynamics and non-associated flow rule are fulfilled.
- The finite element numerical modeling of the plastic zone development around a borehole drilled in an over pressured reservoir shows the advantage of the applied thermomechanics-based viscoplastic model. The modeling scheme used in this study is potentially applicable to other soft rock formations involved other deep geo-energy production or geological engineering projects.

Appendix A

Single-Porosity Poroelastic Solution

The analytical solutions of $\sigma_{rr}^{(1)}, \sigma_{rr}^{(2)}, \sigma_{rr}^{(3)}, \sigma_{\theta\theta}^{(1)}, \sigma_{\theta\theta}^{(2)}, \sigma_{\theta\theta}^{(3)}, p_f^{(2)}$, and $p_f^{(3)}$ in the Laplace domain are given as follows (Abousleiman and Nguyen, 2005)

$$\bar{\sigma}_{rr}^{(1)} = \left(\sigma_m - p_w\right)\frac{R^2}{r^2}H\left(t\right) \tag{A1}$$

$$\bar{\sigma}_{\theta\theta}^{(1)} = -\left(\sigma_m - p_w\right)\frac{R^2}{r^2}H\left(t\right) \tag{A2}$$

$$\bar{\sigma}_{rr}^{(2)} = -\frac{2\chi_t}{s}\left(p_o - p_w\right)\left[\frac{K_1\left[\xi r\right]}{\xi r K_0\left[\xi R\right]} - \frac{R K_1\left[\xi R\right]}{\xi r^2 K_0\left[\xi R\right]}\right] \tag{A3}$$

$$\bar{\sigma}_{\theta\theta}^{(2)} = \frac{2\chi_t}{s}\left(p_o - p_w\right)\left[\frac{K_0\left[\xi r\right]}{K_0\left[\xi R\right]} + \frac{K_1\left[\xi r\right]}{\xi r K_0\left[\xi R\right]} - \frac{R K_1\left[\xi R\right]}{\xi r^2 K_0\left[\xi R\right]}\right] \tag{A4}$$

$$\bar{\sigma}_{rr}^{(3)} = \frac{\sigma_d}{s}\left[C_1\left(\frac{1}{\xi r}K_1\left[\xi r\right] + \frac{6}{\left(\xi r\right)^2}K_2\left[\xi r\right]\right) - C_2\frac{R^2}{r^2} - 3C_3\frac{R^4}{r^4}\right]\cos\left(2\theta\right) \tag{A5}$$

$$\bar{\sigma}_{\theta\theta}^{(3)} = \frac{\sigma_d}{s}\left[-C_1\left(\frac{1}{\xi r}K_1\left[\xi r\right] + \left(1 + \frac{6}{\left(\xi r\right)^2}\right)K_2\left[\xi r\right]\right) + 3C_3\frac{R^4}{r^4}\right]\cos\left(2\theta\right) \tag{A6}$$

$$\bar{p}_f^{(2)} = -\frac{\left(p_o - p_w\right)}{s}\frac{K_0\left[\xi r\right]}{K_0\left[\xi R\right]} \tag{A7}$$

$$\bar{p}_f^{(3)} = \frac{\sigma_d}{2s}\left[\frac{C_1}{\chi_t}K_2\left[\xi r\right] + \frac{fC_2}{Gh/K_v + 1}\frac{R^2}{r^2}\right]\cos\left(2\theta\right) \tag{A8}$$

Where G is the shear modulus, t is time, $H\left(\bullet\right)$ is the Heaviside unit step function, s is the Laplace transform variable, $\bar{\bullet}$ denotes the Laplace transformation, and K_n is the modified Bessel function of the second kind of nth order.

$$\xi = \sqrt{\frac{s}{c}} \tag{A9}$$

In which c is the diffusion coefficient given as:

$$\frac{1}{c} = \frac{1}{\mathcal{K} M_b} + \frac{{\alpha_B}^2}{\mathcal{K} K_v} \tag{A10}$$

Where $\mathcal{K}$ is the fluid mobility which can be obtained by permeability and fluid viscosity:

$$\mathcal{K} = \frac{k}{\mu_f} \tag{A11}$$

K_v is the elastic constant defined as:

$$K_v = K + \frac{4}{3} G \tag{A12}$$

The material coefficients can be found by:

$$\chi_t = \alpha_B \frac{1-2\nu}{2(1-\nu)} \tag{A13}$$

$$f = \frac{\alpha_B c}{\mathcal{K} K_v} \tag{A14}$$

$$h = \alpha_B f - 1 \tag{A15}$$

$$C_1 = -4f\ \chi_t \frac{\xi R}{D_2 - D_1}, \qquad C_2 = \frac{4 D_2}{D_2 - D_1},$$
$$C_3 = -\frac{\xi R\left(D_2 + D_1\right) + 8f\ \chi_t K_2\left[\xi R\right]}{\xi R\left(D_2 - D_1\right)} \tag{A16}$$

With

$$D_1 = 2f\ \chi_t K_1\left[\xi R\right],$$
$$D_2 = \xi R\left(Gh/K_v + 1\right) K_2\left[\xi R\right] \tag{A17}$$

Chapter 4

Stability analysis of a super deep petroleum well drilled in strike-slip fault zones in the Tarim Basin, NW China[†]

4.1. Abstract

The deeply buried petroleum reservoirs are usually associated with fault zones resulting from substantial tectonic activities. Thus, the issue of wellbore stability is particularly important since these natural fractures are quite abundant in fault zones. In this study, we focus on the wellbore stability of a deeply buried petroleum well located in the Tarim area of China. The well was drilled into an Ordovician limestone formation with a buried depth of 8000 meters. Laboratory tests were conducted on rock samples to characterize the mineral compositions, micro-structures, and strength properties. Dual-porosity theories of poromechanics were employed to derive stress and pore pressure distributions in the limestone formation surrounding the wellbore. The risk of wellbore instability was analyzed accordingly. Our results show that stress distribution is susceptible to borehole azimuth. In addition, effective stresses in the rock matrix and fractures surrounding the borehole were derived and analyzed separately, where two failure criteria were applied to rock matrix and fracture, respectively. Given the in-situ stress conditions, the importance of selecting the optimum well trajectory is highlighted. Time-dependent solutions were used to show the importance of including fracture strength in stability analysis of wellbores drilled in fractured porous media.

Keywords: Wellbore stability, poroelasticity, Ordovician limestone, fractured porous media, Dual-porosity.

[†] A version of this manuscript has been published in *Arabian Journal of Geosciences* (2021).

4.2. Introduction

Petroleum production is inherently linked to drilling technology, which ranges from exploration to production, from monitoring to remediation and environmental restoration. With the increasing demand for petroleum resources, deep drilling activities are becoming prevalent in recent years (Ezati et al., 2020; Zeng et al., 2018). For instance, super deep petroleum wells were drilled into an Ordovician limestone reservoir formation with a buried depth about 8000 meters located in the Tarim Basin, China (Méndez et al., 2020; Tian et al., 2019). Previous studies show that the deeply buried "sweet spot" petroleum reservoir was located within strike-slip fault zones of the Tarim intracratonic basin (Ding et al., 2012; Deng et al. 2019; Tian et al., 2019; G. Wu et al., 2019a, 2019b, 2020). Tian et al. (2019) performed geological and geophysical characterizations of deeply buried fractured carbonate reservoirs in the Ordovician reservoir of the Tarim Basin. Wu et al. (2020) extensively used cores, logs, and petroleum production data to characterize the petrophysical and fracture properties of Ordovician limestones in Tarim Basin strike-slip fault zones. These previous characterization results disclose the abundance of natural fractures in Ordovician carbonate reservoirs due to tectonic activities (Ding et al., 2012; Li et al., 2013). The permeability distributions at different scales in carbonate damage zones were also presented (Wu et al. 2020). The existing heterogeneities along these fault damage zones pose a challenge for the exploitation of oil and gas from these carbonate reservoirs (Dashti et al., 2018). Fluid flows and sliding instabilities in fractured zones have high uncertainties due to the variation in fracture roughness (Fang et al., 2018; Li et al., 2014) and infilled minerals (An et al., 2020a; An et al., 2020b; Zhang et al., 2020). Drilling in deeply buried reservoirs are challenged by the complex geological conditions. Inclined boreholes were usually applied to promote well productivity in deep reservoirs, which adds to the complexity of the situation (Ding et al., 2020). The wellbore stability issue is particularly crucial since natural fractures are quite abundant in those fault zones. Even though strength data of Ordovician limestones is critical for wellbore stability analysis, currently there are very limited laboratory results on strength properties available. The reason could be due to the difficulty in sampling in fault damage zones. In addition, performing triaxial mechanical tests under a high confining pressure comparable to the in-situ stress condition is also challenging. It is indispensable to analyze the stability of

wellbores for the determination of well trajectory and drilling mud pressure. In the context of studied Ordovician carbonate reservoirs in fault zones, natural fractures mechanically weaken the rock matrix and provide local conduits for the pore fluid to disperse. The study of wellbore stability should consider the dual-porosity and dual-permeability behaviors of rock fractures and rock matrix (Abousleiman and Ekbote 2005). The analytical solutions by Abousleiman and Nguyen (2005) accurately capture the stresses and pore-pressure variations in both the rock matrix and fractures for wellbore stability analysis. However, the effect of fracture strength on wellbore stability was not considered.

In this study, we performed laboratory tests on Ordovician limestone samples retrieved from wells from a depth of more than 7600 m in order to characterize mineral compositions, microstructures, and strength. We employed the dual-porosity poromechanical analytical solution to analyze the borehole stability condition at critical depth. We demonstrate the importance of considering fracture strength in the borehole stability analysis.

4.3. Integrated characterizations on Ordovician limestone samples

4.3.1. General geology

The studied area is located in Shunbei V fault zone, Tarim Basin, China (Figure 4.1). The Shunbei V fault zone is known as the most extended intracratonic strike-slip fault zone in the Shunbei area within the Tarim Basin (Deng et al. 2019). The Ordovician carbonate reservoirs are buried at a depth ranging from 6500–8000 m and gently dipping to the south of the basin. These reservoirs are generally classified into reef-shoal and paleo-karst reservoirs, which are controlled by microfacies and karstification, respectively (Zhang et al., 2018). Experimental results by Wu et al. (2020) show that the permeability of fault zones is up to two orders of magnitude larger than that found in matrix reservoirs without fractures. Late fracturing and dissolution are the dominant controlling factors affecting permeabilities of rocks from these carbonate reservoirs. Multiple faulting and diagenetic events result in complex permeability distributions along the carbonate damage zones.

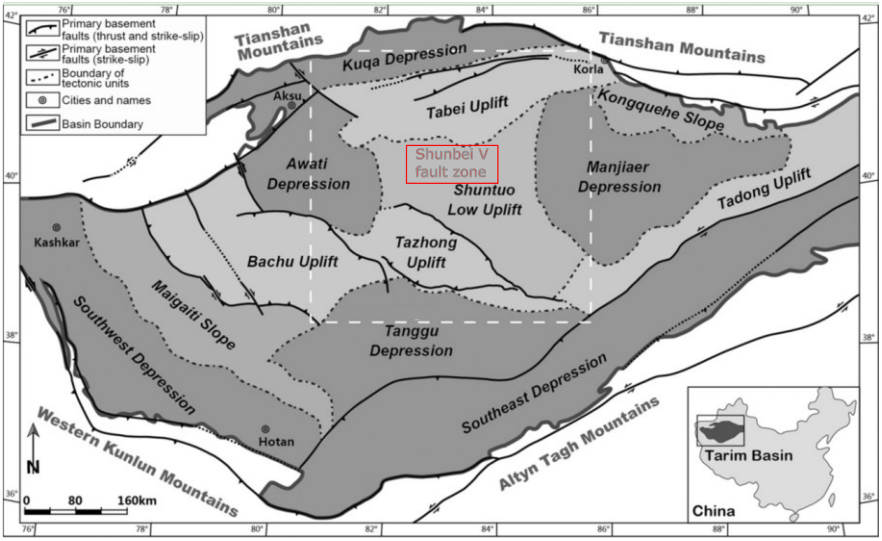

Fig. 4.1. Geological map of the major tectonic units in the Tarim Basin with the study area marked (modified from Deng et al. 2019).

Rock samples were retrieved from 3 different wells (Well-1, Well-2, and Well-3) and laboratory characterizations were conducted to determine mineral composition, microstructures, and strength. Due to the strong tectonic activities in the fault zone, the rock formation was strongly affected, and it was challenging to retrieve many intact rock samples. Among those samples, only intact samples from Well-2 were available for triaxial tests to obtain strength parameters.

4.3.2. Mineral composition and SEM image analysis

We carried out the X-ray powder diffraction (XRD) analysis on collected specimens according to petroleum testing standards (Allen et al. 1988). The tests were applied to characterize the mineralogical content and compositions of samples or specimens. Mineralogy compositions of samples from Well-1 and Well-2 are included in Table 4.1, which shows that the studied limestone is mainly composed of calcite and dolomite with a small fraction of quartz. Samples from Well-3 display strong heterogeneity; thus we conducted more tests and summarized them in Table 4.2. It should be noted that samples with the same depth in meter were retrieved from the same core sampling tube and they were marked as the upper, the middle, or the bottom parts of the core.

Table 4.1. Mineralogy composition of Ordovician limestone samples retrieved from Well-1 and Well-2. Qz = Quartz; Plag = Plagioclase feldspar; Cal = Calcite; Dol = Dolomite; Anal = Analcite; Hem = Hematite.

Well name and Sample depth	Mineral composition（%）						
	Qz	Plag	Cal	Dol	Anal	Hem	Clay
Well-1 (7470.15 m-7470.21 m)	2.9	0	72.1	23.7	0	1.3	0
Well-2 (7560.23 m -7560.38 m)	2.5	0.6	96.9	0	0	0	0

Table 4.2. Mineralogy composition of Ordovician limestone samples retrieved from Well-3. Qz = Quartz; K-feld = Potassic feldspar; Plag = Plagioclase feldspar; Cal = Calcite; Dol = Dolomite; Anal = Analcite; Anhy = Anhydrite.

Depth (m)	Note	Mineral composition（%）									
		Qz	K-feld	Plag	Cal	Dol	Anal	Barite	Augite	Anhy	Clay
7126	Upper	0.5	0	0.2	67.6	18	0	0	0	0	13.7
	Middle	0.7	0.4	0.2	80.2	17.9	0	0	0	0	0.6
	Bottom	20.3	0	0	0	77.1	0	0	0	0	2.6
7235	Upper	0.8	0.1	0.4	96.7	0	0	0	0	0	2
	Middle	0.7	0	0.2	96.9	0	0	0.1	0	0	2.1
	Bottom	1.6	0	0.5	1.5	53.9	0	0	1.7	0	40.8
7260	Upper	2.8	0	0.8	2.7	91.2	0	0	0	0	2.5
	Middle	0.8	0	0.2	0.9	76	0.2	0	0	0	21.9
	Bottom	42.4	5.8	12.7	33	0	0	0	0	6.1	0

The strong heterogeneity is shown by the significant difference in mineral contents of samples with the same sampling depth. The result also shows the presence of clay minerals and anhydrite. FEI Quanta 200F Quanta Scanning Electron Microscope was used to observe the microstructure of rock specimens. Dominant minerals (e.g., dolomite and calcite) of rock samples from Well-3 are identified and displayed in Figure 4.2. Images showing fracture tomography in the studied limestone samples from Well-3 are displayed in Figure 4.3. Those intergranular fractures shown in Figure 4.3, indicate strong stress concentration present in the rock formations. These fractures can be created during tectonic activities, which leads to strong heterogeneity in rock samples.

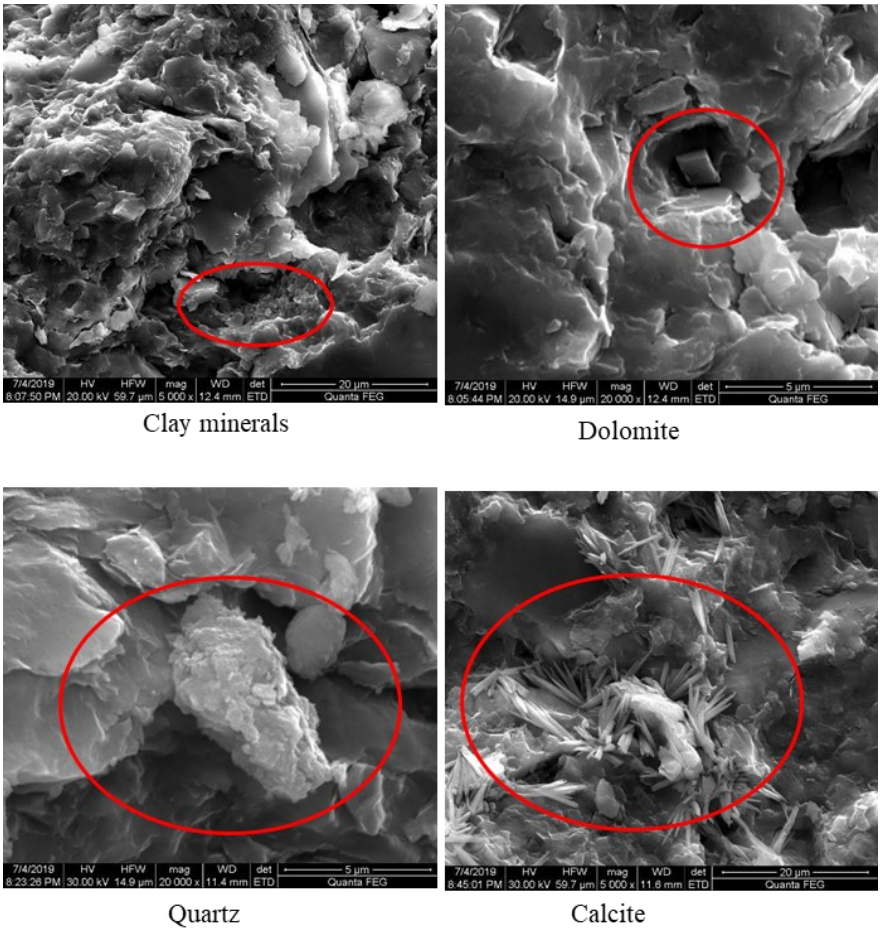

Fig. 4.2. SEM images showing dominant minerals presented in the studied formation (Well-3).

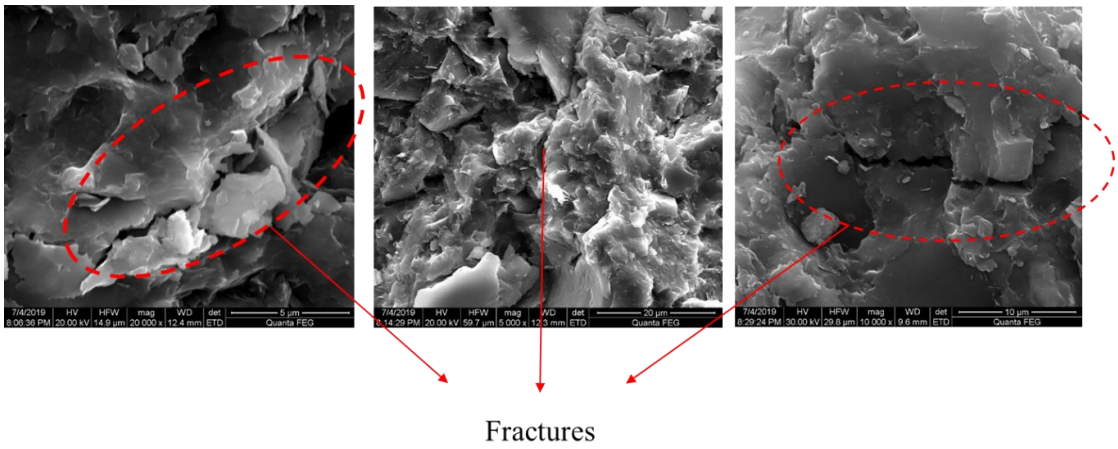

Fig. 4.3. SEM images showing fracture tomography in the studied limestone samples (Well-3).

4.3.3. Triaxial test

The geomechanical behavior of the studied limestone samples were measured through triaxial compression tests under various confining pressures. The triaxial compression tests were conducted using a GCTS triaxial test system (RTR1500). Intact samples from Well-2 from a depth of 7560m were used for the test. The proposed triaxial tests were supposed to measure the matrix strength of the studied limestone. Samples used in the tests had a diameter of 25 mm and a height of 50 mm. The mineral composition of those samples can be found in Table 4.1, which shows the abundance of Calcite mineral. Triaxial tests were conducted at confining pressures of 65 MPa, 75 MPa, and 85 MPa, respectively. The applied confining pressure is comparable to the in-situ effective stress condition reported by Ding et al. (2012). To reduce the difficulty, we did not conduct pore pressure measurements for those tests. Photographs of rock samples before and after triaxial testing were obtained and displayed in Figure 4.4. Under such a high confining pressure condition, samples still maintain general integrity after triaxial tests, indicating high plastic behavior.

Measured stress-strain curves at different confining pressures are shown in Figure 4.5a. For an axial strain lower than 0.5%, the samples display a linear elastic trend, and the impact from the applied confining pressure is negligible.

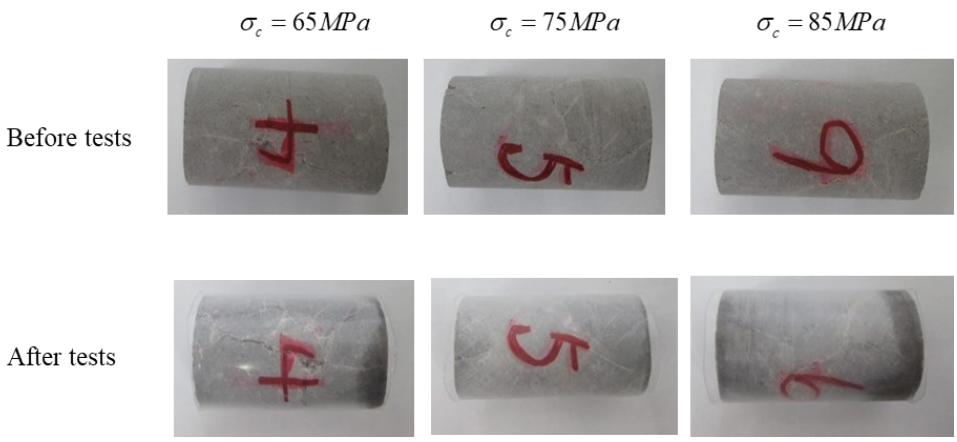

Fig. 4.4. Photographs showing rock samples before and after triaxial testing (Well-2, depth = 7560m).

The strain hardening effect is noticed when the applied stress is beyond the yield limit, which is also an indication of high plastic behavior in such high confining pressure conditions. The strain hardening plastic behavior under high confining pressure condition is consistent with that of limestone samples reported by Paterson and Wong (2005). After taking three tests' peak strengths, we obtained the strength parameters after displaying strength measurement in equivalent mean stress-equivalent shear stress (p-q stress space) and fitting the measured results with the linear Drucker-Prager model (Figure 4.5b).

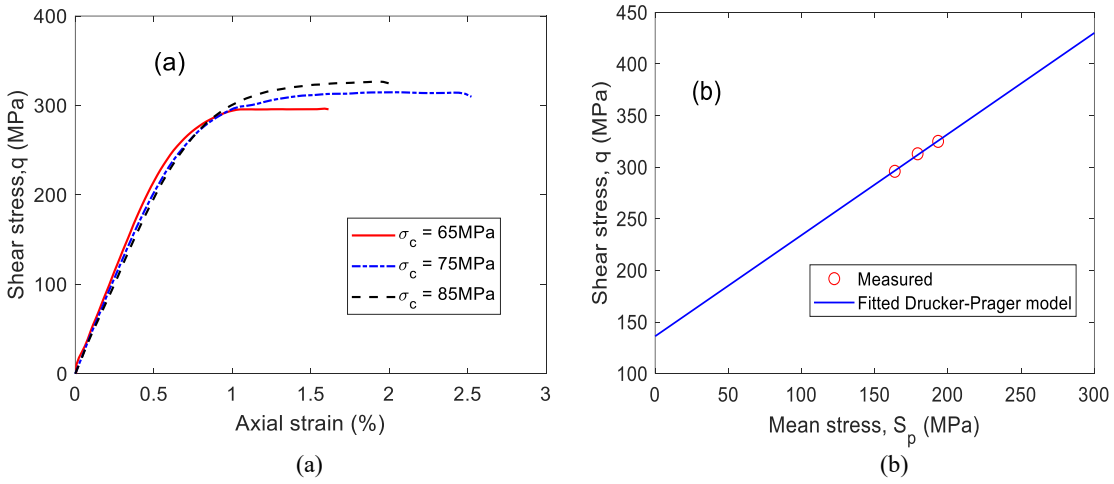

Fig. 4.5. Measured triaxial test results shown in (a) stress-strain curves and (b) strength data in mean stress-shear stress space (σ_c = confining pressure).

The linear Drucker-Prager model is expressed as:

$$F = q - S_p \tan\beta - d = 0 \tag{4.1}$$

where S_p is the mean effective stress, and q is the von Mises shear stress. Under a triaxial testing condition, $S_p = (\sigma_1 + 2\sigma_3)/3$ and $q = \sigma_1 - \sigma_3$. It should be noted that parameters β and *d,* are not the same as the commonly used friction angle (φ) and cohesion strength (*c*). They are related to φ and *c* as $\tan\beta = \frac{6\sin\varphi}{3-\sin\varphi}$ and $d = \frac{6c\cos\varphi}{3-\sin\varphi}$ (Puzrin 2012). The obtained β and *d* for the studied limestone are critical strength parameters for the subsequent wellbore stability analysis.

4.4. Poromechanical analysis of wellbore stability

4.4.1. Dual porosity poro-mechanical theory

A representative elementary volume (REV) shown in Figure 4.6a can be used to describe the dual-porosity theory, which includes the rock matrix and the embedded fractures. The system contains two separate and overlapping fluid-saturated porous media: one represents the primary porosity matrix, and the other represents the secondary porosity medium fractures. Each medium is assumed to have its own poro-mechanical and physical properties such as elastic moduli, Biot's effective stress coefficients, and fluid mobilities. The two media communicate and may exchange fluid mass (Figure 4.6b). At any REV, it is assumed that there are two separate continua, each with its own pressure field, and separate constitutive laws and governing equations are considered for each region (Abousleiman and Nguyen 2005). In some formations, fractures are filled with minerals with reduced strength parameters. The slippage behavior of different parts alongside the fractured area shown in Figure 4.6c is potentially contributing to wellbore instability issues.

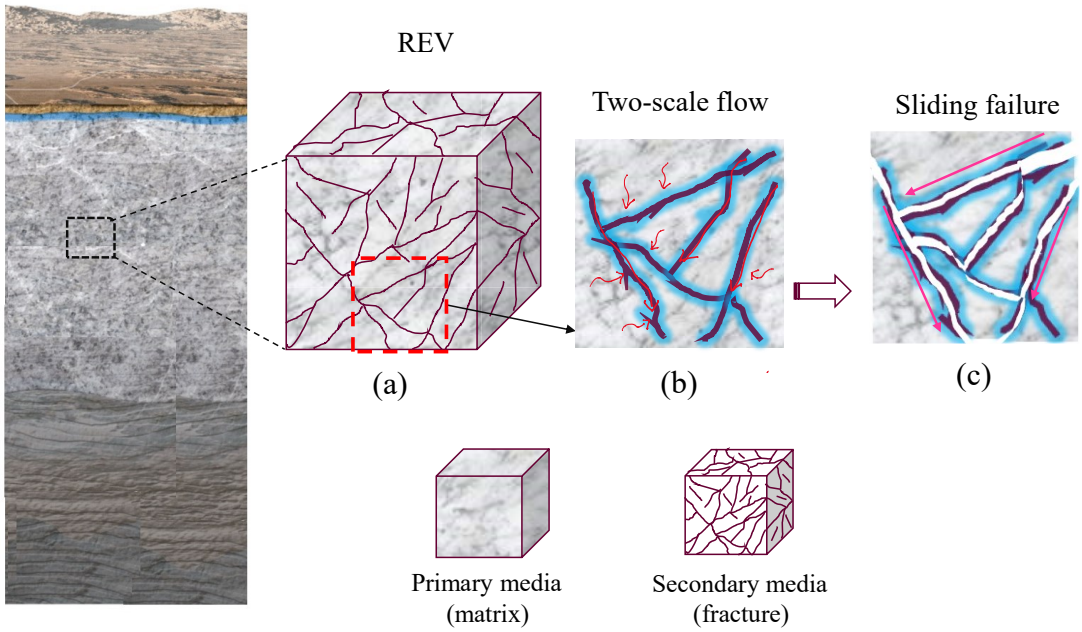

Fig. 4.6. Sketch showing the representative elementary volume (REV) of dual porosity-dual permeability model of (a) fractured rock containing matrix and fracture, (b) flow among matrix and fractures, (c) sliding failure along fractures, modified after Abousleiman and Nguyen (2005).

The total stresses and resultant strains cannot be expressed separately for each medium. However, effective stresses in matrix and fracture will be different due to the difference in pore pressure. On the macroscopic REV boundary, the stresses and strains in the REV must be referred to. Under the assumption that each porous medium is homogeneous and isotropic, the constitutive equations for the porous medium or naturally fractured rock formation can be written as (Aifantis 1979):

$$\sigma_{ij} = 2G\varepsilon_{ij} + \left(K - \frac{2}{3}G \right)\varepsilon_{kk}\delta_{ij} - \left(\frac{K\alpha^{I}}{K^{I}} p^{I} + \frac{K\alpha^{II}}{K^{II}} p^{II} \right)\delta_{ij} \tag{4.2a}$$

$$p^{I} = M^{I}\left(\zeta^{I} - \frac{K\alpha^{I}}{K^{I}}\varepsilon_{kk} \right) \tag{4.2b}$$

$$p^{II} = M^{II}\left(\zeta^{II} - \frac{K\alpha^{II}}{K^{II}}\varepsilon_{kk} \right) \tag{4.2c}$$

In the above equations, superscripts I and II refer to the porous rock matrix and the porous fractures medium, respectively. σ_{ij} is the total stress tensor and ε_{ij} is the strain tensor. G and K are the overall shear modulus and the bulk modulus, respectively. α and M are Biot effective stress coefficient and Biot modulus, respectively. p is pore pressure; ζ is the fluid content variation in the corresponding medium. The Navier-type field equation is given based on the equilibrium equation combined with the stress–strain–pressure relations (Wilson and Aifantis, 1982).

$$G\nabla^2 u_i + (\lambda + G)\frac{\partial^2 u_k}{\partial x_i \partial x_k} = \frac{K\alpha^I}{K^I}\frac{\partial p^I}{\partial x_i} + \frac{K\alpha^{II}}{K^{II}}\frac{\partial p^{II}}{\partial x_i} \tag{4.3}$$

where λ = Lamé constant and u_i = displacement vector.

In terms of fluid pore pressures, the diffusion equations in the matrix and fracture are expressed as:

$$\frac{1}{M^I}\frac{\partial p^I}{\partial t} + \frac{K\alpha^I}{K^I}\frac{\partial \varepsilon_{kk}}{\partial t} = \frac{k^I}{\mu}\nabla^2 p^I + \Gamma\left(p^I - p^{II}\right) \tag{4.4a}$$

$$\frac{1}{M^{II}}\frac{\partial p^{II}}{\partial t} + \frac{K\alpha^{II}}{K^{II}}\frac{\partial \varepsilon_{kk}}{\partial t} = \frac{k^{II}}{\mu}\nabla^2 p^{II} - \Gamma\left(p^{II} - p^I\right) \tag{4.4b}$$

where ε_{kk} = total volumetric strain, and ∇^2 = Laplacian operator.

In the Equations from 4.2 to 4.4, tension positive convention of solid mechanics has been used, which is for the benefit of deriving hydro-mechanical coupled equations. In all other equations within this paper, the compression positive convention has been applied.

4.4.2. Analytical solution for inclined wellbores embedded in fractured porous media.

As shown in Figure 4.7, an inclined borehole is defined with two coordinates. The coordinate of x', y', z' is coincident with the *in-situ* principal stress axes to which the axis of wellbore is inclined. A local coordinate system (x, y, z) is used to establish the

analytical solution where the z axis coincides with the borehole axis. The wellbore azimuth φ_b is a rotation angle of borehole axis and the inclination angle γ_b is the inclination of the borehole.

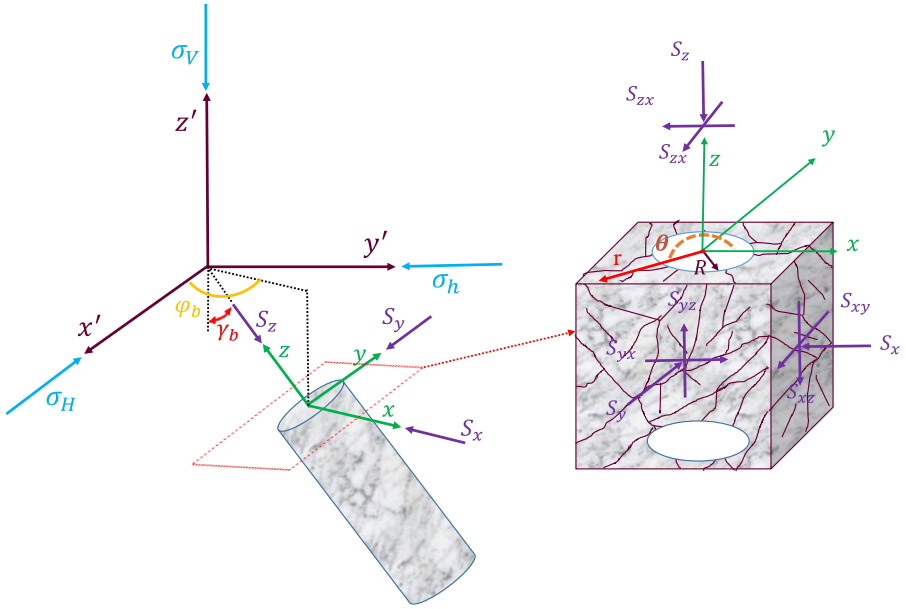

Fig. 4.7. Schematic view of an inclined wellbore drilled in naturally fractured rock formations, modified after Abousleiman and Nguyen (2005) (φ_b and γ_b are wellbore azimuth and inclination angles; r and θ are radial coordinate in the wellbore local coordinate).

In the borehole coordinate system, stress transformation was used to convert the in-situ stresses to normal and shear far field stresses, which the borehole is subjected to. The transformation equation (Equation 4.5) was given in Fjaer et al. (1992).

$$\begin{Bmatrix} S_x \\ S_y \\ S_z \\ S_{xy} \\ S_{yz} \\ S_{xz} \end{Bmatrix} = \begin{pmatrix} l_{xx'}^2 & l_{xy'}^2 & l_{xz'}^2 \\ l_{yx'}^2 & l_{yy'}^2 & l_{yz'}^2 \\ l_{zx'}^2 & l_{zy'}^2 & l_{zz'}^2 \\ l_{xx'}l_{yx'} & l_{xy'}l_{yy'} & l_{xz'}l_{yz'} \\ l_{yx'}l_{zx'} & l_{yy'}l_{zy'} & l_{yz'}l_{zz'} \\ l_{zx'}l_{xx'} & l_{zy'}l_{xy'} & l_{zz'}l_{xz'} \end{pmatrix} \begin{Bmatrix} \sigma_H \\ \sigma_h \\ \sigma_V \end{Bmatrix} \tag{4.5}$$

where S_x, S_y, S_z, S_{xy}, S_{xy}, and S_{xy} are six stress components of far field stresses around a borehole (Figure 4.7); σ_H is the maximum horizontal stress; σ_h is the minimum horizontal stress; and σ_V is the vertical stress.

The inputs in the transformation matrix are given by:

$$\begin{bmatrix} l_{xx'} & l_{xy'} & l_{xz'} \\ l_{yx'} & l_{yy'} & l_{yz'} \\ l_{zx'} & l_{zy'} & l_{zz'} \end{bmatrix} = \begin{bmatrix} \cos\varphi_b \cos\gamma_b & \sin\varphi_b \cos\gamma_b & -\sin\gamma_b \\ -\sin\varphi_b & \cos\varphi_b & 0 \\ \cos\varphi_b \sin\gamma_b & \sin\varphi_b \sin\gamma_b & \cos\gamma_b \end{bmatrix} \tag{4.6}$$

The complete analytical solution for the inclined wellbore drilled fractured-rock formation are given as (Abousleiman and Nguyen 2005).

$$p^{\mathrm{I}} = p_0 + \mathrm{P}^{\mathrm{I}(2)} + \mathrm{P}^{\mathrm{I}(3)} \tag{4.7}$$

$$p^{\mathrm{II}} = p_0 + \mathrm{P}^{\mathrm{II}(2)} + \mathrm{P}^{\mathrm{II}(3)} \tag{4.8}$$

$$\sigma_{rr} = \sigma_m - \sigma_d \cos\left[2\left(\theta - \theta_r\right)\right] - \sigma_{rr}^{(1)} - \sigma_{rr}^{(2)} - \sigma_{rr}^{(3)} \tag{4.9}$$

$$\sigma_{\theta\theta} = \sigma_m + \sigma_d \cos\left[2\left(\theta - \theta_r\right)\right] - \sigma_{\theta\theta}^{(1)} - \sigma_{\theta\theta}^{(2)} - \sigma_{\theta\theta}^{(3)} \tag{4.10}$$

$$\sigma_{zz} = S_{zz} - 2v\sigma_m + v\left(\sigma_{rr} + \sigma_{\theta\theta}\right) + \left(1-2v\right)\left[\beta^I\left(p^{\mathrm{I}} - p_0\right) + \beta^{II}\left(p^{\mathrm{II}} - p_0\right)\right] \tag{4.11}$$

$$\sigma_{r\theta} = -\sigma_d \sin\left[2\left(\theta - \theta_r\right)\right] + \sigma_{r\theta}^{(3)} \tag{4.12}$$

$$\sigma_{rz} = -\left(S_{xz}\cos\theta + S_{yz}\sin\theta\right)\left[1 - \frac{R^2}{r^2}\right] \tag{4.13}$$

$$\sigma_{\theta z} = \left(S_{xz}\sin\theta - S_{yz}\cos\theta\right)\left[1 + \frac{R^2}{r^2}\right] \tag{4.14}$$

The solution of stress tensors $\sigma_{\mathrm{rr}}^{(1)}$, $\sigma_{\mathrm{rr}}^{(2)}$, $\sigma_{\mathrm{rr}}^{(3)}$, $\sigma_{\theta\theta}^{(1)}$, $\sigma_{\theta\theta}^{(2)}$, $\sigma_{\theta\theta}^{(3)}$, $\sigma_{\mathrm{r}\theta}^{(3)}$ in terms of cylindrical polar coordinates and dual pore pressures $\mathrm{P}^{\mathrm{I}(2)}$, $\mathrm{P}^{\mathrm{I}(3)}$, $\mathrm{P}^{\mathrm{II}(2)}$ and $\mathrm{P}^{\mathrm{II}(3)}$ are given in the Laplace domain which can be found in Appendix B. R is the radius of the well, r and θ are radial coordinates in the wellbore local coordinate. p_0 denotes the original formation pore

pressure before excavation, v is the overall Poisson's ratio, β^I and β^{II} are lumped pore pressure coefficients defined in Appendix B. The terms of σ_m, σ_d and θ_r are given as:

$$\sigma_m = \frac{S_x + S_y}{2} \tag{4.15a}$$

$$\sigma_d = \sqrt{\left(\frac{S_x - S_y}{2}\right)^2 + S_{xy}{}^2} \tag{4.15b}$$

$$\theta_r = \frac{1}{2}\tan^{-1}\left[\frac{2S_{xy}}{S_x - S_y}\right] \tag{4.15c}$$

At the far field, when $r \to \infty$, the boundary conditions can be assumed around the domain using the cubic REV as shown in Figure 4.7. The solution in time is solved by a numerical inversion method (Stehfest 1970). We put the time domain solution into implementation using MATLAB. The numerical code has been validated using a dual porosity porous media case study presented in Abousleiman and Nguyen (2005) and a single porosity example from Abousleiman and Cui (1998). Our numerical code yields the same results as that from Abousleiman and Nguyen (2005) and Abousleiman and cui (1998).

4.4.3. Poromechanical analysis of an inclined well in China's Tarim Basin

China Sinopec reported that borehole failure and drilling bit jamming are common in some wells at the depth about 8000 meters in the reservoir formation of Tarim Basin. After borehole failure, borehole cleaning and recovery required substantial time and effort, which has resulted in a major economic loss. The wellbore stability issues are closely related to instability of fractured Ordovician limestone formation since the study area is within the strike-slip fault zones of the Tarim intracratonic basin. The preliminary wellbore stability analysis conducted by a drilling company in the studying area was based on theories for intact rocks and the two-scale flow behavior between rock matrix and fractures were not considered. In order to improve the reliability of the determinations of well

trajectory and drilling mud pressure, we have applied the above-mentioned analytical solution to analyze the stress and pore pressure distribution of an inclined wellbore at a depth of 7800 m. In situ stresses and an inclined wellbore geometry data provided by our drilling company partner are included in Table 4.3. We will also try to investigate the cases with different well trajectory and drilling mud pressures. The results can be used as guidance for drilling activities in the study area. The poromechanics parameters of Ordovician limestones shown in Table 4.4 are adopted for the stability analysis. For the limestone samples retrieved from depths larger than 6000 m, the matrix's porosity is less than 5%, and fracture porosity is negligible because the fracture aperture is too small (Wu et al. 2020). The permeability values of 0.002 mD and 0.2 mD for matrix and fractures are based on the laboratory core analysis in carbonate fault damage zones performed by Wu et al. (2020). Wu et al. (2020) also presented a range of permeability intervals for intact and fractured cores. We select one possible, but representative case to be used for our analysis. The mechanical properties of the matrix are based on our triaxial test results. Other poro-mechanical and fluid properties are from Abousleiman and Nguyen (2005).

Table 4.3. In situ stresses and well geometry parameters of an inclined borehole drilled in Shunbei V fault zone, Tarim Basin, China

Parameters	**Units**	**Values**		**Parameters**	**Units**	**Values**	
In situ stresses				**Wellbore**			
σ_V	MPa	195	Overburden pressure	R	m	0.15	Radius
σ_H	MPa	179	Maximum horizontal stress	φ_b	Degree	115	Azimuth
σ_h	MPa	146	Minimum horizontal stress	γ_b	Degree	37	Inclination
p_0	MPa	90	Formation pore pressure	Depth	m	7800	-
				ρ_w	kg/ m^3	1430	Mud density

Table 4.4. Poromechanical parameters of studied Ordovician limestone used for wellbore stability analysis.

Parameters	Units	Values	
Dual porosity			
E	GPa	40	Overall Young's modulus
K^{I}	GPa	24	Matrix bulk modulus
G^{I}	GPa	16	Matrix shear modulus
ν	-	0.23	Poisson's ratio
K_s	GPa	80	Grain bulk modulus
K_f	MPa	1744	Fluid bulk modulus
K^{II}	GPa	8	Fracture bulk modulus
G^{II}	GPa	5	Fracture shear modulus
k^{I}	m^2	2×10^{-18}	Matrix permeability
α^{I}	-	0.7	Matrix Biot's coefficient
ϕ^{I}	-	0.04	Matrix porosity
k^{II}	m^2	2×10^{-16}	Fracture permeability
α^{II}	-	0.9	Fracture Biot's coefficient
ϕ^{II}	-	0.004	Fracture porosity
μ	Pa.s	10^{-3}	Fluid viscosity
Γ	$(\mathrm{MPa.s})^{-1}$	10^{-9}	Interporosity flow
Drucker–Prager yield criterion			
d	MPa	136.2	Cohesion
β	Degree	44.4	Angle of friction

We applied different approaches to calculate the total stress distribution around a borehole. Shown in Figure 4.8, the time evolution of total stress for dual media is the same as the single porosity case since the developed stress field is only dependent of stress boundary conditions; thus, the total stress will be approximately the same for both media after t = 1 day.

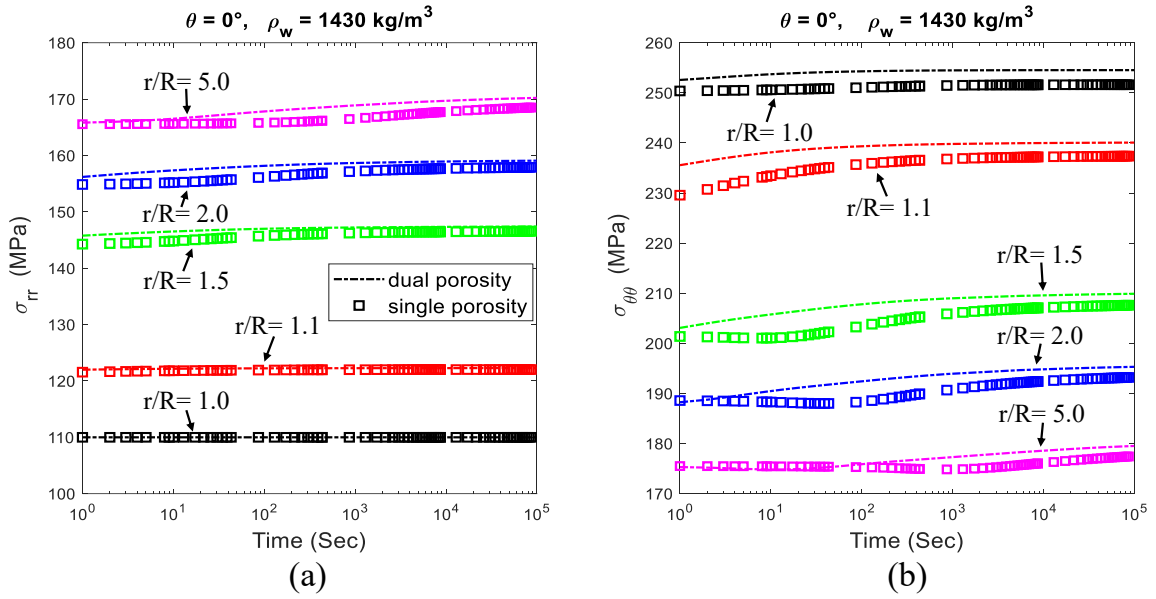

Fig. 4.8. Variation of total (a) radial stress, and (b) tangential stress with respect to time at different radial distances.

Figure 4.9 shows the history of pore pressure in both matrix and fractures at two different radial distances around the wellbore. At a point far from the well (r/R = 2), the mobilization of initial pore pressure (90 MPa) takes more time since the flow path is longer. The virgin formation pore pressure at a point close to the well (r/R = 1.05) comes into balance with mud pressure before t = 1 day. We plot the evolution of dual pore pressure and tangential effective stresses along the radial distance in Figure 4.10 to have a detailed analysis. At t = 10 seconds, two distinct pore pressures are observed (Figure 4.10a).

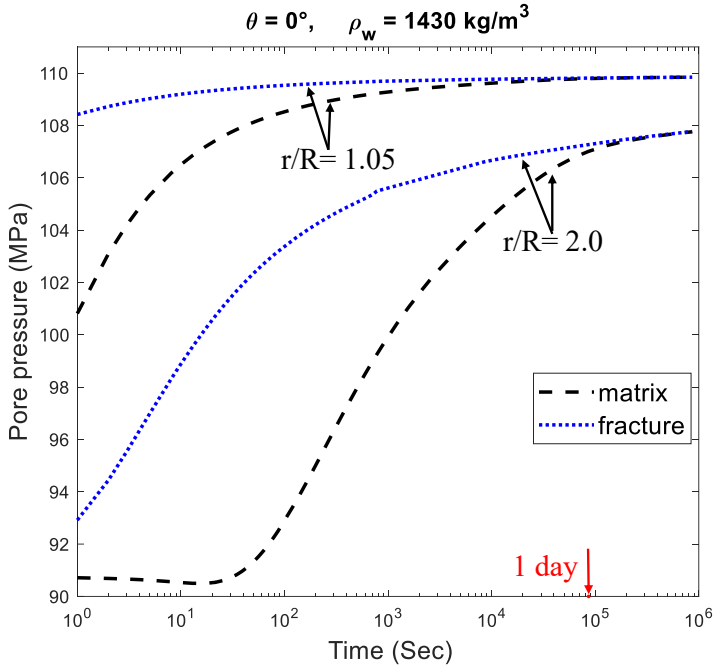

Fig. 4.9. Time history of pore pressure in matrix and fractures at different distances to wellbore wall.

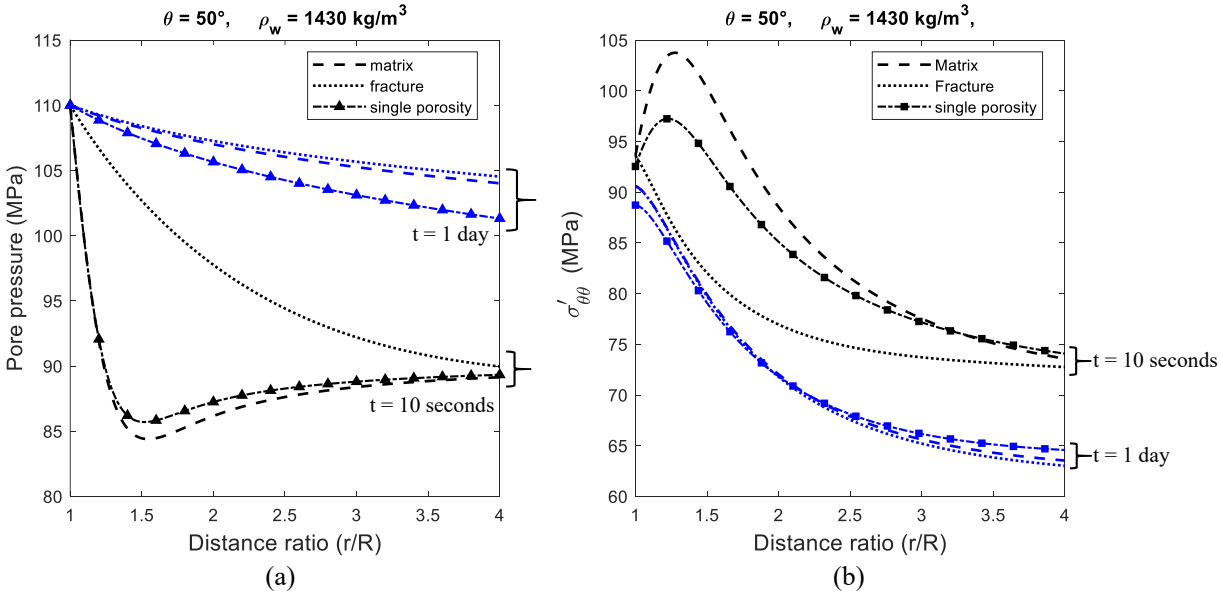

Fig. 4.10. Distributions of (a) pore pressure and (b) tangential effective stresses for dual media at t = 10 sec, and t =1 day.

Fracture pore pressure dissipates faster because of high fracture permeability when compared with the rock matrix. As time goes on, the distribution of pore pressure becomes more uniform for both media. In Figure 4.10b, the matrix media displays a higher effective stress than that from the single porosity case. The difference in effective stress between single and dual-media shows the necessity of applying dual-porosity theory to conduct a stability analysis. Our results indicate that the most critical time slot is the moment after drilling.

For stability analysis, we have applied Drucker-Prager failure criteria shown in Equation 4.1 to evaluate the stability of excavation affected zones surrounding the borehole. The mean effective stress S_p^I and von Mises shear stress q in the rock matrix were calculated using Equations 4.16 and 4.17, respectively.

$$S_p^I = \frac{\sigma_{rr} + \sigma_{\theta\theta} + \sigma_{zz}}{3} - p^I \tag{4.16}$$

$$q = \frac{1}{\sqrt{2}}\left[\left(\sigma_{rr} - \sigma_{\theta\theta}\right)^2 + \left(\sigma_{rr} - \sigma_{zz}\right)^2 + \left(\sigma_{\theta\theta} - \sigma_{zz}\right)^2 + 6\sigma_{r\theta}^2 + 6\sigma_{rz}^2 + 6\sigma_{\theta z}^2\right]^{\frac{1}{2}} \tag{4.17}$$

We applied the "stress cloud" technique by Bradley (1978) to show the stress distributions (with θ ranging from $0°$ to $360°$) in the limestone formation around the borehole, where the plot of stresses are displayed in the $S_p - q$ space. In the studying area, a borehole inclination ($37°$) was established by our partner company to achieve the best petroleum production. The selection of this borehole inclination was based on the reservoir characterization result. Thus, we did not conduct a parametric study by changing the borehole inclinations. Instead, the parametric study of the effect of borehole azimuth values was conducted and displayed in Figure 4.11. Our results show that stress cloud distributions are sensitive to borehole azimuth. Within an azimuth window from $100°$ to $115°$, an azimuth larger than $105°$ brings a high risk of borehole instability, which is shown by the intersection of stress cloud and rock failure line. By contrast, the well will be stable at an azimuth lower than $105°$. For the case of $\varphi_b = 100°$ (determined as the safest case in the

previous analysis), we conducted a parametric study to establish the effect of changing drilling mud densities.

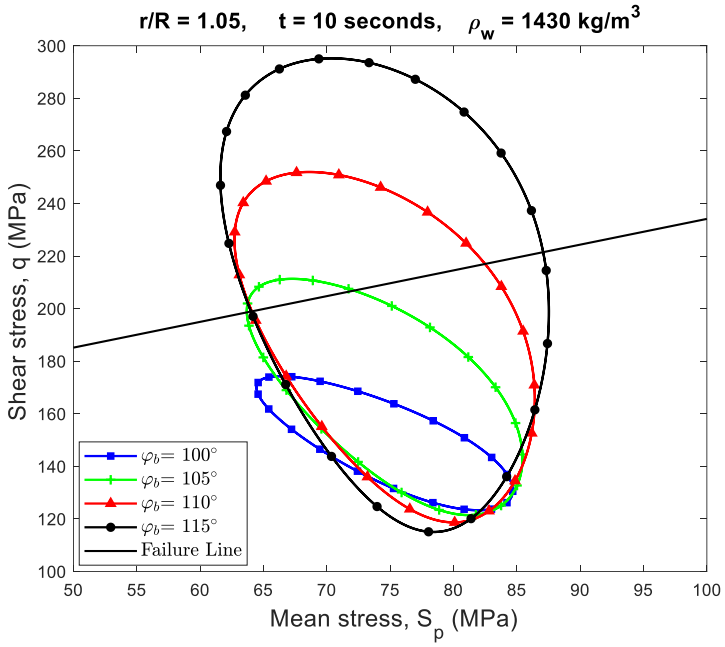

Fig. 4.11. Plots showing the wellbore azimuth effect on the stress clouds (a stress cloud is a representation of stresses around the wellbore with different θ).

The stress clouds for cases with three possible drilling mud densities are derived and plotted in Figure 4.12. Our results show that all those three different drilling mud densities yield a safe well with the given φ_b =100°. The evolution of the stress cloud for the case with φ_b =100° and ρ_w = 1430 kg/m^3 is shown in Figure 4.13. The cloud at different times does not change noticeably since the fluid at the points near the wall depletes after 10 minutes (Figure 4.9). It should be noted that all previous analysis was based on the strength of the rock matrix, and the consideration of fracture strength will be addressed in the subsequent section.

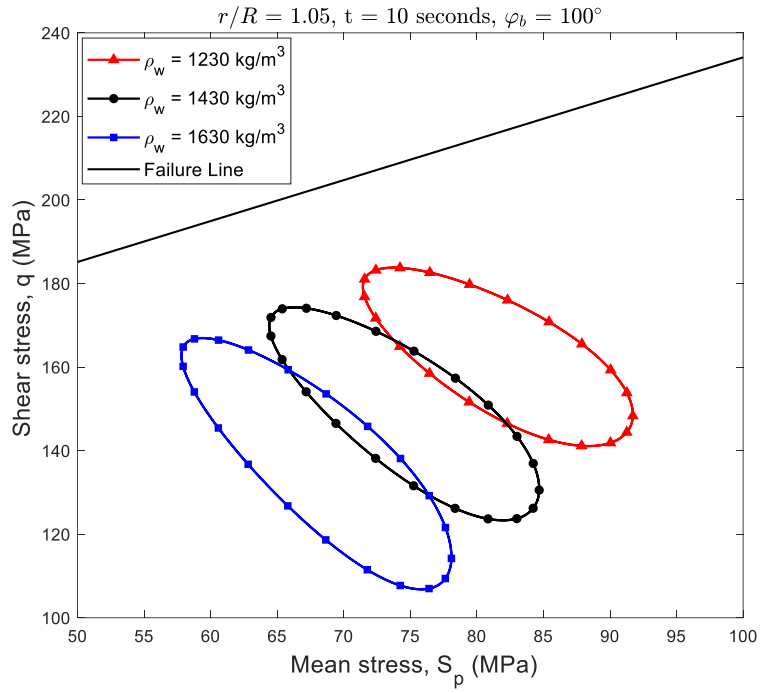

Fig. 4.12. Plots showing the changing of drilling mud densities on the development of stress clouds.

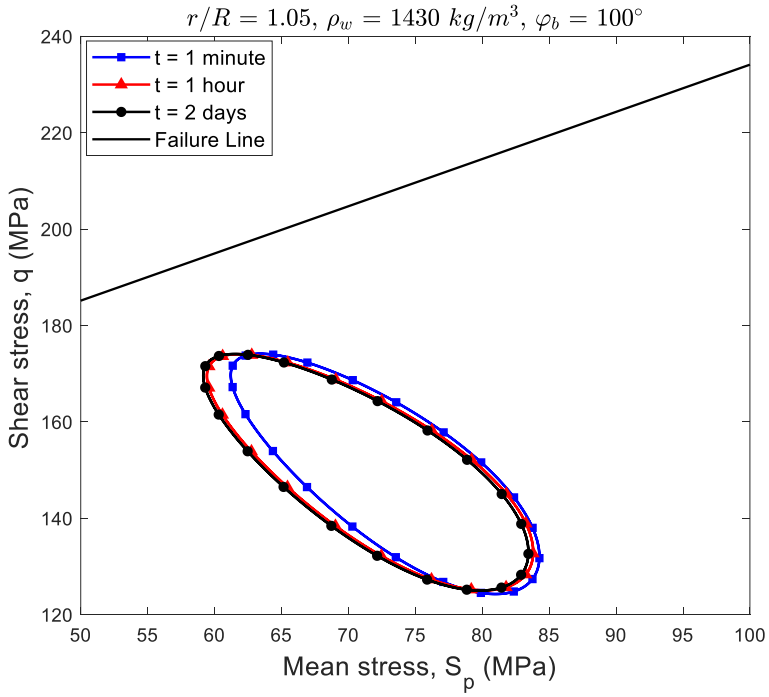

Fig. 4.13. Plots showing the development of stress clouds with the elapsed time.

4.5. Discussion

4.5.1. Consideration of fracture strength

The previous poro-mechanical analysis applied the strength of the rock matrix as the failure criterion. However, the studied Ordovician limestones contain different scales of fractures (Wu et al. 2019a,b). The narrow aperture fractures present were mainly infilled by cements (Figure 4.14a) and the wider aperture were infilled by calcite cement or bitumen (Figure 4.14b). Even though those infills may contribute to the cohesion strength of the fracture under the in-situ high confining stress condition, the strength of fractures or joints is certainly less than the intact rock. When the rock formation loses its stability, it tends to slide along those weak fracture planes (Figure 4.6). As described in Section 4.3, the total stresses in the matrix and fractures are treated the same, since the total stresses and resultant strains cannot be expressed separately for each medium.

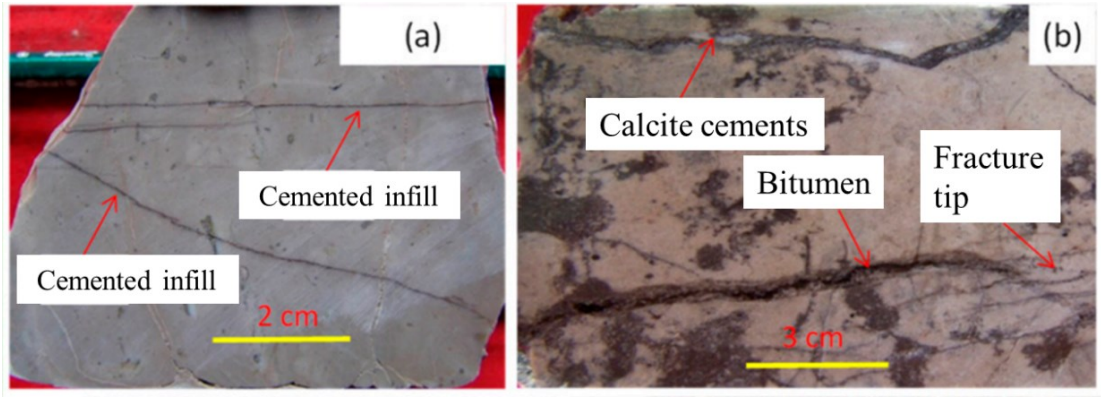

Fig. 4.14. Photographs showing fractures in Ordovician carbonate cores with (a) narrow aperture with cemented infill, and (b) wider aperture infilled by calcite cements or bitumen, modified after Wu et al. (2019a,b).

In order to evaluate the stability within the rock matrix and fractures separately, two separate pore pressure fields should be used in calculating effective stresses. Since the von Mises equivalent shear stress q is calculated based on total stresses (Equation 4.17), shear stresses in matrix and fractures are equal. By contrast, other than the mean effective stress given for the rock matrix (Equation 4.16), the mean effective stress in fractures S_p^{II} will be given by Equation 4.18.

$$S_p^{II} = \frac{\sigma_{rr} + \sigma_{\theta\theta} + \sigma_{zz}}{3} - p^{II} \tag{4.18}$$

As presently we do not have the experimental result of fracture strength, laboratory tests on the strength of fractures are recommended for a future study. We have used reduced cohesion (70% of the intact rock) to represent the cohesion of infills in rock fractures. Considering the case with $\varphi_b = 100°$ and $\rho_w = 1430$ kg/m^3, the well was treated as safe both in the analysis based on a single porosity solution and in the analysis based on a dual-porosity solution but setting rock matrix strength as the failure line (Figure 4.15). However, the well is analyzed as not stable if the stress cloud for fracture is included with a reduced cohesion strength applied in the failure line. The observed stability issue of the studied super deep well drilled in Tarim Basin can be primarily related to rock fractures' failure behavior.

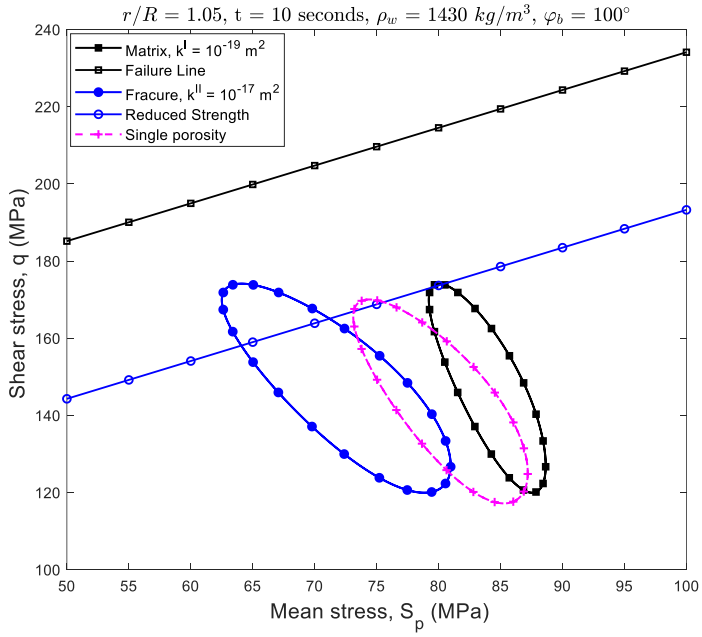

Fig. 4.15. A comparison of stress clouds of matrix and fractures with the corresponding failure criteria.

4.5.2. Plastic behavior and thermal impacts

The study is at the preliminary stage of stability analysis of drilled boreholes. Our triaxial test results show that the studied limestone displays significant strain hardening at a high confining pressure condition. However, our applied analytical solution is based on linear elastic constitutive laws and cannot consider the progressive hardening effect at a high-pressure condition. The applied linear Drucker-Prager model is easier for displaying stress clouds in the $S_p - q$ space, however, it does not contain the Lode angle, thus the 3D stress effect cannot be considered. Numerical modeling with advanced constitutive models is recommended to investigate the progress development of the yield zone (Akhtar and Li, 2020; B. Li et al., 2018). In addition, such a deep well is related to a high temperature environment. The plastic behavior of limestone will be more significant at a high temperature condition (Paterson and Wong 2005). Temperature and fluid pressurization effects on frictional stability of natural fractures and wellbore integrity should also be considered (An et al., 2020a; Norouzi et al., 2019). Since our triaxial tests were carried out at ambient temperature condition, high temperature and high pressure triaxial tests are recommended to achieve more accurate strength measurements.

4.6. Conclusion

We performed the stability analysis of a deeply buried petroleum well located in Xinjiang area of China using laboratory characterization results and dual-porosity poroelastic analytical solutions. The conclusions are drawn as the following:

- Our laboratory characterization on mineral compositions and micro-structures of Ordovician limestone samples confirms the dominant minerals as calcite and dolomite. Under a high confining pressure condition, strain hardening effect is noticed when the applied stress is beyond the yield limit. Before yielding, this Ordovician limestone displays linear elastic behavior regardless of the magnitude of applied confining pressures.
- The applying of dual-porosity theories yields more reasonable stress analysis since the diffusion behavior among rock matrix and fractures is considered. The

difference in effective stresses in the rock matrix and fractures is significant in the early excavation period. Given the in-situ stress condition, stress distributions in such deeply buried formations surrounding a wellbore are very sensitive to the borehole azimuth. Thus, an accurate characterization of the in-situ stress directions and magnitudes is essential to the whole project.

- Our results demonstrate the importance of considering fracture strength in the poromechanical analysis of borehole stability in fractured porous media. The observed issues of borehole failure and drilling bit jamming in the studying area can be primarily related to the failure behavior of rock fractures.

Appendix B

Double-Porosity Poroelastic Solution

The solution of $\sigma_{rr}^{(1)}$, $\sigma_{rr}^{(2)}$, $\sigma_{rr}^{(3)}$, $\sigma_{\theta\theta}^{(1)}$, $\sigma_{\theta\theta}^{(2)}$, $\sigma_{\theta\theta}^{(3)}$, $\sigma_{r\theta}^{(3)}$, $\mathrm{P}^{\mathrm{I}(2)}$, $\mathrm{P}^{\mathrm{I}(3)}$, $\mathrm{P}^{\mathrm{II}(2)}$ and $\mathrm{P}^{\mathrm{II}(3)}$ in the Laplace domain are given as (Abousleiman and Nguyen, 2005):

$$\bar{\sigma}_{rr}^{(1)} = \left(\sigma_m - p_w\right)\frac{R^2}{r^2}H\left(t\right) \tag{B1}$$

$$\bar{\sigma}_{\theta\theta}^{(1)} = -\left(\sigma_m - p_w\right)\frac{R^2}{r^2}H\left(t\right) \tag{B2}$$

$$\bar{\mathrm{P}}^{\mathrm{I}(2)} = -\frac{1}{s}\left(\frac{p_o - p_w}{m^I - m^{II}}\right)\times\left\{\begin{array}{c}\left(1-m^{II}\right)\Phi\left[\xi^{\mathrm{I}}\right]\\ -\left(1-m^{I}\right)\Phi\left[\xi^{\mathrm{II}}\right]\end{array}\right\} \tag{B3}$$

$$\bar{\mathrm{P}}^{\mathrm{II}(2)} = -\frac{1}{s}\left(\frac{p_o - p_w}{m^I - m^{II}}\right)\times\left\{\begin{array}{c}m^I\left(1-m^{II}\right)\Phi\left[\xi^{\mathrm{I}}\right]\\ -m^{II}\left(1-m^{I}\right)\Phi\left[\xi^{\mathrm{II}}\right]\end{array}\right\} \tag{B4}$$

$$\bar{\sigma}_{rr}^{(2)} = -\frac{1}{s}\frac{2G}{K_v}\left(\frac{p_o - p_w}{m^I - m^{II}}\right)\times\left\{\begin{array}{c}h^I\left(1-m^{II}\right)\Lambda\left[\xi^{\mathrm{I}}\right]\\ -h^{II}\left(1-m^{I}\right)\Lambda\left[\xi^{\mathrm{II}}\right]\end{array}\right\} \tag{B5}$$

$$\bar{\sigma}_{\theta\theta}^{(2)} = \frac{1}{s}\frac{2G}{K_v}\left(\frac{p_o - p_w}{m^I - m^{II}}\right)\times\left\{\begin{array}{c}h^I\left(1-m^{II}\right)\left(\Phi\left[\xi^{\mathrm{I}}\right]+\Lambda\left[\xi^{\mathrm{I}}\right]\right)\\ -h^{II}\left(1-m^{I}\right)\left(\Phi\left[\xi^{\mathrm{II}}\right]+\Lambda\left[\xi^{\mathrm{II}}\right]\right)\end{array}\right\} \tag{B6}$$

$$\bar{\mathrm{P}}^{\mathrm{I}(3)} = \frac{\sigma_d}{2s}K_v\cos\left[2\left(\theta-\theta_r\right)\right]\times\left\{C_1\mathrm{K}_2\left[\xi^{\mathrm{I}}\mathrm{r}\right]-C_2\mathrm{K}_2\left[\xi^{\mathrm{II}}\mathrm{r}\right]+f^I C_3\frac{R^2}{r^2}\right\} \tag{B7}$$

$$\begin{aligned}\bar{\mathrm{P}}^{\mathrm{II}(3)} = &\frac{\sigma_d}{2s}K_v\cos\left[2\left(\theta-\theta_r\right)\right]\\ &\times\left\{m^I C_1\mathrm{K}_2\left[\xi^{\mathrm{I}}\mathrm{r}\right]-m^{II}C_2\mathrm{K}_2\left[\xi^{\mathrm{II}}\mathrm{r}\right]+f^{II}C_3\frac{R^2}{r^2}\right\}\end{aligned} \tag{B8}$$

$$\bar{\sigma}_{rr}^{(3)} = \frac{\sigma_d}{s}\cos\left[2\left(\theta-\theta_r\right)\right]\times\left\{\begin{array}{l} G\left(h^I C_1 \Theta\left[\xi^{\mathrm{I}}\right] - h^{II} C_2 \Theta\left[\xi^{\mathrm{II}}\right]\right) \\ -\left(Gh+K_v\right)C_3\frac{R^2}{r^2} - 3C_4\frac{R^4}{r^4} \end{array}\right\} \tag{B9}$$

$$\bar{\sigma}_{\theta\theta}^{(3)} = -\frac{\sigma_d}{s}\cos\left[2\left(\theta-\theta_r\right)\right]\times\left\{G\left(h^I C_1 \Omega\left[\xi^{\mathrm{I}}\right] - h^{II} C_2 \Omega\left[\xi^{\mathrm{II}}\right]\right) - 3C_4\frac{R^4}{r^4}\right\} \tag{B10}$$

$$\bar{\sigma}_{r\theta}^{(3)} = \frac{\sigma_d}{s}\sin\left[2\left(\theta-\theta_r\right)\right]\times\left\{\begin{array}{l} 2G\left(h^I C_1 \Psi\left[\xi^{\mathrm{I}}\right] - h^{II} C_2 \Psi\left[\xi^{\mathrm{II}}\right]\right) \\ -\frac{\left(Gh+K_v\right)}{2}C_3\frac{R^2}{r^2} - 3C_4\frac{R^4}{r^4} \end{array}\right\} \tag{B11}$$

In Equations B1 to B11, deviatoric stress σ_d and mean stress σ_m are defined in Equation 4.15.

$$\frac{1}{K} = \frac{1}{K^I} + \frac{1}{K^{II}} \tag{B12}$$

$$\frac{1}{G} = \frac{1}{G^I} + \frac{1}{G^{II}} \tag{B13}$$

$$\beta^{(N)} = \frac{\alpha^{(N)}K^{(N)}}{K} \qquad N = I, II \tag{B14}$$

$$\Phi\left[\xi\right] = \frac{K_0\left[\xi \mathrm{r}\right]}{K_0\left[\xi \mathrm{R}\right]} \tag{B15}$$

$$\Lambda\left[\xi\right] = \frac{K_1\left[\xi \mathrm{r}\right]}{\xi \mathrm{r} K_0\left[\xi \mathrm{R}\right]} - \frac{RK_1\left[\xi \mathrm{R}\right]}{\xi r^2 K_0\left[\xi \mathrm{R}\right]} \tag{B16}$$

$$\Theta\left[\xi\right] = \frac{1}{\xi r}K_1\left[\xi \mathrm{r}\right] + \frac{6}{\left(\xi \mathrm{r}\right)^2}K_2\left[\xi \mathrm{r}\right] \tag{B17}$$

$$\Omega\left[\xi\right] = \frac{1}{\xi r}K_1\left[\xi \mathrm{r}\right] + \left(1+\frac{6}{\left(\xi \mathrm{r}\right)^2}\right)K_2\left[\xi \mathrm{r}\right] \tag{B18}$$

$$\Psi\left[\xi\right]=\frac{1}{\xi r}K_1\left[\xi \mathrm{r}\right]+\frac{3}{\left(\xi \mathrm{r}\right)^2}K_2\left[\xi \mathrm{r}\right] \tag{B19}$$

ξ^I and ξ^{II} are two positive roots of the following characteristic equation.

$$\left(\xi^2-M_{11}\right)\left(\mathcal{K}_r\xi^2-M_{22}\right)-M_{12}M_{21}=0 \tag{B20}$$

$\mathcal{K}_r$ is mobility ratio which can be found by fluid mobility $\mathcal{K}$ as

$$\mathcal{K}_r=\frac{\mathcal{K}^{II}}{\mathcal{K}^I} \quad and \quad \mathcal{K}^{(N)}=\frac{k^{(N)}}{\mu^{(N)}}, \quad N=I,II \tag{B21}$$

In which k^I and k^{II} are the permeability of matrix and fracture respectively.

$\mathrm{M}_{11}, \mathrm{M}_{22}, \mathrm{M}_{21}$ and M_{12} are lumped coefficients defined as

$$M_{11}=\frac{s}{\mathcal{K}^I}\left(\frac{1}{M^I}+\frac{\left(\beta^I\right)^2}{K_v}\right)+\frac{\Gamma}{\mathcal{K}^I} \tag{B22}$$

$$M_{12}=M_{21}=\frac{s}{\mathcal{K}^I}\left(\frac{\left(\beta^I\beta^{II}\right)^2}{K_v}\right)-\frac{\Gamma}{\mathcal{K}^I} \tag{B23}$$

$$M_{22}=\frac{s}{\mathcal{K}^I}\left(\frac{1}{M^{II}}+\frac{\left(\beta^{II}\right)^2}{K_v}\right)+\frac{\Gamma}{\mathcal{K}^I} \tag{B24}$$

in which the material coefficients can be founded by

$$\frac{1}{\mathrm{M}^{\mathrm{I}}}=\left(\frac{\alpha^{\mathrm{I}}-\phi^{\mathrm{I}}}{\mathrm{K_s}}+\frac{\phi^{\mathrm{I}}}{\mathrm{K_f}}\right) \tag{B25}$$

$$\frac{1}{\mathrm{M}^{\mathrm{II}}}=\left(\frac{\alpha^{\mathrm{II}}-\phi^{\mathrm{II}}}{\mathrm{K_s}}+\frac{\phi^{\mathrm{II}}}{\mathrm{K_f}}\right) \tag{B26}$$

$$h^{(N)} = \beta^{I} + \beta^{II} m^{(N)}, \quad N = I, II \tag{B27}$$

$$h = \beta^{I} f^{I} + \beta^{II} f^{II} - 1 \tag{B28}$$

$$m^{(N)} = \frac{\left[\left(\xi^{(N)}\right)^2 - M_{11}\right]}{M_{12}}, \quad N = I, II \tag{B29}$$

$$\begin{Bmatrix} f^{I} \\ f^{II} \end{Bmatrix} = \frac{s}{\mathcal{K}^{I} K_v} \begin{bmatrix} M_{11} & M_{12} \\ M_{21} & M_{22} \end{bmatrix}^{-1} \begin{Bmatrix} \beta^{I} \\ \beta^{II} \end{Bmatrix} \tag{B30}$$

$$C_1 = -4\xi^{\mathrm{I}}\mathrm{R}\frac{D_2}{D_4}, \qquad C_2 = -4\xi^{\mathrm{II}}\mathrm{R}\frac{D_1}{D_4}, \qquad C_3 = 4\frac{D_3}{D_4} \tag{B31}$$

$$C_4 = \frac{1}{D_4}\begin{bmatrix} 2Gh^{II} D_1 \left(K_1\left[\xi^{\mathrm{II}} R\right] + \dfrac{4}{\xi^{\mathrm{II}} R} K_2\left[\xi^{\mathrm{II}} R\right] \right) \\ -2Gh^{I} D_2 \left(K_1\left[\xi^{\mathrm{I}} R\right] + \dfrac{4}{\xi^{\mathrm{I}} R} K_2\left[\xi^{\mathrm{I}} R\right] \right) - \left(Gh + K_v\right) D_3 \end{bmatrix} \tag{B32}$$

Where

$$D_1 = \xi^{\mathrm{I}}\left(f^{II} - f^{I} m^{I}\right)\ \mathrm{K}_2\left[\xi^{\mathrm{I}}\mathrm{R}\right] \tag{B33}$$

$$D_2 = \xi^{\mathrm{II}}\left(f^{II} - f^{I} m^{II}\right)\ \mathrm{K}_2\left[\xi^{\mathrm{II}}\mathrm{R}\right] \tag{B34}$$

$$D_3 = \xi^{\mathrm{I}}\xi^{\mathrm{II}}\mathrm{R}\left(m^{I} - m^{II}\right)\mathrm{K}_2\left[\xi^{\mathrm{I}}\mathrm{R}\right]\mathrm{K}_2\left[\xi^{\mathrm{II}}\mathrm{R}\right] \tag{B35}$$

$$D_4 = 2\mathrm{G}\left(h^{II} D_1 \mathrm{K}_1\left[\xi^{\mathrm{II}}\mathrm{R}\right] - h^{I} D_2 \mathrm{K}_1\left[\xi^{\mathrm{I}}\mathrm{R}\right]\right) + \left(Gh + K_v\right) D_3 \tag{B36}$$

Chapter 5

Finite element modeling of wellbore stability in a fractured formation for the geothermal development in northern Quebec, Canada[†]

5.1. Abstract

Previous studies showed that deep geothermal energy can be a promising solution to support Canada's energy transition, which is particularly valuable for remote northern communities. Geological formations containing natural fractures in fault zones of the Canadian Shield prove advantageous for geothermal development from the perspective of permeability enhancement. However, it is crucial to ensure wellbore stabilities throughout the drilling and energy production processes. In remote communities, there is a lack of research investigating the overall performance of boreholes embedded in fractured formations under non-isothermal conditions. In this study, we carry out finite element modeling on poromechanical analysis of boreholes in fractured rock formations of a potential deep geothermal engineering site in northern Canada. Both plastic yielding in the rock matrix and sliding potential along specific fractures are quantified with the consideration of non-isothermal impacts. Our results indicate that the cooling effect should be given attention when drilling through rock formations containing natural fractures as excess pore pressure can be built up due to the enhanced flows through fractures. Even though the fractures are not intersecting with the borehole wall surface, sliding tends to be triggered along tilted fractures. In addition, more plastic zones tend to be generated due to the cooling effect of drilling fluid. Findings from the present research are also closely relevant to deep geoenergy engineering projects in other studying areas with fractured geological formations.

[†] A version of this manuscript has been submitted to *Geoenergy Science and Engineering* Journal (2023).

Keywords: Thermo-Hydro-Mechanical coupling, fractured formation, slip tendency, finite element method, wellbore stability.

5.2. Introduction

Off-grid communities in Canada rely extensively on fossil fuels to fulfill their energy requirements. All Nunavik's villages rely on fossil fuels to produce both electricity and heat, with production prices 10 times more than those in Southern Québec of Canada. This unsustainable energy system necessitates a fundamental change, and deep geothermal energy offers a promising solution (Miranda et al., 2020, 2023a, b). A study conducted by Grasby et al. (2012) explored the geothermal potential of northern Quebec, and their results indicate that the Canadian Shield holds promise as a prospective region for the future development of enhanced geothermal systems (EGS). Deep drilling is necessary to explore the potential of utilizing deep geothermal energy, including both energy production and deep geothermal energy storage. Specific geological conditions, such as fractured formations in fault zones of the Canadian Shield, prove advantageous for geothermal development from the perspective of permeability enhancement. However, it is crucial to ensure wellbore and fault stabilities throughout the drilling and energy production processes (An et al., 2021; Heidari et al., 2021; Li et al., 2018; Li et al., 2022; Zhang et al., 2019). Pore pressure and stress changes in deep wellbores are highly related to thermal-hydro-mechanical coupled processes in rock formations, which exerts a substantial impact on wellbore stability (Heidari et al., 2021, 2023; Li et al., 2018a; Tang et al., 2021). For geological formations containing natural fractures, the act of drilling into deep formations involves complex Thermo-Hydro-Mechanical (THM) coupled processes within fractured porous media. It is important to accurately assess and quantify the flow within both the fractures themselves and the surrounding rock matrix (Berre et al., 2019; Wang et al., 2021). Understanding these flow dynamics is essential for the effective production of geothermal energy. Additionally, the flow occurring within both fractures and the rock matrix has a direct impact on the redistribution of effective stress around the wellbore during excavation (Younessi and Rasouli, 2010). This, in turn, has the potential to expand

the plastic zone surrounding a wellbore. Managing this stress redistribution is crucial to maintain wellbore stability and ensuring the overall integrity of the geothermal engineering system. For the poromechanical analysis of wellbores drilled in a dual-porosity media under the non-isothermal condition, many analytical solutions have been presented in the past decades. Abousleiman and Ekbote (2005) presented analytical solutions for the inclined borehole problem in a transversely isotropic poroelastic medium under non-isothermal conditions. Li et al. (2018b) used fully coupled THM solutions to investigate the local thermal non-equilibrium effect on thermo-poroelastic responses of wellbores. Fan and Parashar (2019) proposed analytical solutions to investigate how cooling influences the sliding movement of preexisting fractures and changes the stress and pore pressure fields around a wellbore. Mirabbasi et al. (2020) presented an analytical thermo-poroelastic model based on fracture mechanics to add the stresses resulting from the changes in pore pressure and fluid temperature to the analytical elastic equations. The study of Mirabbasi et al. (2020) reveals that as the temperature difference between the drilling fluid and the formation of pore fluid increases, the thermal stresses around the wellbore wall become more pronounced. When the wellbore is cooled, it leads to the development of tensile stresses and promotes tensile fracturing behaviors. Using the thermo-poroelastic theory, Tang et al. (2021) discovered that the thermo-poroelastic effect of rock formation makes the wellbore susceptible to a shear failure mode. Furthermore, the cooling effect of drilling fluid diminishes the severity of wellbore breakout during the drilling process. A novel integrated formulation was introduced by Wang et al. (2021) to study the behavior of boreholes embedded in naturally fractured formations subjected to non-isothermal and two-phase fluid flow conditions. The formulation of Wang et al. (2021) utilizes a dual-porosity model and specifically focuses on scenarios involving a constant flow injection rate. Analytical solutions are often insufficient when it comes to addressing complex engineering problems that involve intricate boundary and loading conditions. In this regard, numerous numerical simulations have been performed synchronously (Gelet et al., 2012; Heidari et al., 2023; Nair et al., 2004; Wu et al., 2018). Due to the advantages of dealing with boundary conditions and the scalability of the numerical framework, the finite element method (FEM) is usually applied to carry out numerical modeling of borehole problems. In the study of Nair et al. (2004), a finite element dual-porosity model incorporating THM

coupling in fractures and rock matrix was developed. Nair et al. (2004) highlighted the importance of the temperature effect in the poromechanical analysis of wellbores drilled in fractured formations. Gelet et al. (2012) developed a comprehensive finite element formulation to model the THM behavior of a dual porous medium under non-isothermal and diffusion conditions. In their work, they also discussed the diffusion mechanisms and mass transfer between materials possessing two porosities. However, in most of those numerical approaches, the fractured porous media is also homogenized as a dual porous medium, thus stress and pore pressure distributions along a specific fracture cannot be quantified. The fracture slip tendency cannot be quantified in the homogenized formulation. Gomar et al. (2016) combine the finite element method for fully coupled thermo-poroelastic analysis of stress distribution around the borehole with the displacement discontinuity method to model fracture deformation and changes in fracture permeabilities during drilling in fractured rocks. Nevertheless, the slipping tendency is also not addressed. In addition, the thermal convection term is usually neglected in most previous analytical or numerical poromechanical analyses in fractured media for simplicity. Several studies have highlighted the role of thermal stresses in increasing the slipping tendency of major faults zones around deep geothermal wells demonstrating that such effect should also be relevant to fractured rock mass (Blöcher et al., 2018; Jacquey et al., 2015, 2016, 2018; Jeanne et al., 2014). There is however a lack of understanding of the overall performance of boreholes embedded in fractured formations under thermal disturbance with the considerations of plastic yielding of the rock matrix and the sliding potential of fractures. It is particularly relevant for a deep geothermal energy engineering project, where high stress and temperature conditions can be found in such formations. In this study, we carry out FEM analysis to investigate the THM coupled processes of fractured rock formations containing uncased boreholes for a potential deep geothermal engineering project in northern Canada. Both plastic yielding in rock matrix and sliding potential along specific fractures are quantified with the consideration of non-isothermal impacts. The studying site in Quebec is taken as an practical example, and the presented numerical approaches are also appliable to deep drilling issues in other geoenergy engineering projects.

5.3. Governing equations and constitutive laws

To model coupled THM processes, it is necessary to solve the governing equations for fluid flow, heat transfer, and deformation of both the porous medium and discrete fractures. These equations are derived from the principles of energy, mass, and momentum conservation for both the fluid and solid constituents. In this section, we present the governing equations specifically for a deformable porous media that is fully saturated. These equations are based on Biot's theory of consolidation (Biot, 1956). A more detailed presentation of the coupled equations can be found in Cacace and Jacquey (2017).

5.3.1. THM coupled governing equations

Momentum conservation

The stress equilibrium of the fluid-saturated porous medium can be written as:

$$\nabla\cdot\left(\boldsymbol{\sigma}' - \alpha_B p_f \delta_{ij}\right) = 0 \tag{5.1}$$

In which $\boldsymbol{\sigma}'$ is the effective stress tensor, p_f is the pore fluid pressure, and δ_{ij} is the Kronecker tensor.

Using the drained bulk modulus, K and the solid bulk modulus, K_s; Biot's poroelastic coefficient is obtained as:

$$\alpha_B = 1 - \frac{K}{K_s} \tag{5.2}$$

Mass conservation

The governing equation for reservoir fluid pressure results from the fluid mass balance can be given as:

$$\frac{1}{M_b}\frac{\partial p_f}{\partial t} - \beta_b \frac{\partial T}{\partial t} + \alpha_B \frac{\partial \varepsilon_{kk}}{\partial t} + \left(1-\alpha_B\right)\frac{\partial \varepsilon_{kk}^p}{\partial t} + \nabla\cdot\ \boldsymbol{q}_f = 0 \tag{5.3}$$

with t, T, β_s, and β_f being time, temperature, thermal expansion coefficients of the solid grains and fluid respectively. ε_{kk} is the total volumetric strain and ε_{kk}^{p} is the plastic volumetric strain. β_b is the bulk volumetric thermal expansion coefficient, which is calculated using $\beta_b = n\beta_f + (1-n)\beta_s$.

Biot's modulus M_b and Darcy based velocity $\boldsymbol{q}_{\mathrm{f}}$ given in Equation 5.3 are adopted as:

$$\frac{1}{M_b} = \frac{n}{K_f} + \frac{(\alpha_B - n)}{K_s} \tag{5.4}$$

$$\boldsymbol{q}_{\mathrm{f}} = -\frac{k}{\mu_f}\nabla\cdot\ p_f \tag{5.5}$$

Where n, K_f, k, μ_f denote the porosity, fluid bulk modulus, permeability, and fluid viscosity.

Porosity evolution

The rate of porosity change induced exclusively by the coupled THM processes can be shown as:

$$\frac{\partial n}{\partial t} - (\alpha_B - n)\left(\frac{1}{K_s}\frac{\partial p_f}{\partial t} - \beta_s\frac{\partial T}{\partial t} + \frac{\partial \varepsilon_{kk}}{\partial t}\right) - (1-\alpha_B)\frac{\partial \varepsilon_{kk}^{p}}{\partial t} = 0 \tag{5.6}$$

Equation 5.6 is derived from the solid mass balance and is complementary to Equation 5.3 (fluid mass balance).

Energy conservation

The governing equation for temperature results from the energy balance of the porous-system under the thermal equilibrium condition expressed as:

$$(\rho C)_b\frac{\partial T}{\partial t} + \nabla\cdot(\rho_f C_f \boldsymbol{q}_f T - \lambda_b \nabla\cdot T) = 0 \tag{5.7}$$

where $(\rho C)_b = (1-n)\rho_s C_s + n\rho_f C_f$ is the bulk specific heat, $\lambda_b = (1-n)\lambda_s + n\lambda_f$ is the bulk thermal conductivity, λ_s, λ_f, C_s, and C_f are thermal conductivities and thermal capacities of the solid and fluid constituents respectively. It should be noted that Equation 5.7 considers transport of heat both by conduction and by advection, the latter requiring a numerical stabilization technique when a FEM discretization is used.

Strain partitioning

The deformation of the rock matrix can be described following an additive splitting of the total strain ε, considering elastic, thermal, and irreversible (plastic) deformation:

$$\varepsilon = \varepsilon^e + \varepsilon^T + \varepsilon^p \tag{5.8}$$

where the superscripts e, T, and p refer to elastic, thermal, and plastic respectively. The thermal strain is expressed as:

$$\dot{\varepsilon}_{ij}^T = \frac{1}{3}\beta_b \dot{T}\,\delta_{ij} \tag{5.9}$$

Where $\dot{T}$ is the relative temperature rate and δ_{ij} is the identity matrix.

The plastic strain is expressed as:

$$\dot{\varepsilon}_{ij}^p = \dot{\gamma}\frac{\partial \Theta}{\partial \sigma'_{ij}} \tag{5.10}$$

where $\dot{\gamma}$ is the plastic multiplier satisfying the Khun-Tucker conditions and Θ is the plastic potential to be described in the next section.

5.3.2. Plasticity

In this study, we applied the Drucker-Prager (DP) plastic model to characterize the plastic yield and deformation behavior of rock matrix. The DP yield function reads as:

$$F = \sqrt{J_2 + \varepsilon_0^2} + \frac{\sin(\varphi)}{3} J_1 - C\cos(\varphi) \tag{5.11}$$

where the following expressions show the first and second stress invariants of the effective stress tensor:

$$J_1 = -\sigma'_{kk} \tag{5.12}$$

$$J_2 = \frac{1}{2}\tau_{ij}\tau_{ij} \tag{5.13}$$

where the deviatoric stress tensor τ_{ij} is given as:

$$\tau_{ij} = \sigma'_{ij} + \frac{1}{3} J_1 \delta_{ij} \tag{5.14}$$

C and φ are the Mohr–Coulomb friction angle and cohesion respectively. ε_0 is a small non-hardening parameter to relax the singularity at the cone's tip of the yield envelope. A non-associated form of DP model with a plastic potential function Θ as a function of dilation angle ψ is used for quantifying plastic strains:

$$\Theta = \sqrt{J_2} + \frac{\sin(\psi)}{3} J_1 \tag{5.15}$$

5.3.3. Fracture sliding potential

Changes in fluid pressure and temperature within a reservoir or near a borehole can modify the in-situ stress state and ultimately result in the reactivation of pre-existing fault zones (Blöcher et al., 2018; Jacquey et al., 2016; Jeanne et al., 2014). The likelihood of this reactivation and associated seismic activity during geothermal operations depends on the initial stress conditions acting on planes of weakness. To evaluate the potential for reactivation, slip tendency (ST) analysis is commonly used to identify the most susceptible fault or fracture planes. ST analysis is based on the concept that fault or fracture

reactivation is determined by the ratio of the shear stress to effective normal stress on the fault or fracture surface (Lisle and Srivastava, 2004; Blöcher et al., 2018).

$$\mathrm{ST} = \frac{\|\tau\|}{\|\boldsymbol{\sigma}_n - \alpha_B p_f\|} \tag{5.16}$$

where $\|\bullet\|$ denotes the norm of the stress, τ, and $\boldsymbol{\sigma}_n$ are the shear and normal stresses acting on the plane of the fracture. When the shear stress surpasses the shear strength of a fracture, slip will take place. This can be determined using the Mohr-Coulomb failure criterion as outlined by Labuz and Zang (2012):

$$\tau \geq S_0 + \mu_s \cdot \boldsymbol{\sigma}_n' \tag{5.17}$$

$$ST \geq \frac{S_0}{\boldsymbol{\sigma}_n'} + \mu_s \tag{5.18}$$

where μ_s is the friction coefficient and S_0 is the cohesion strength of the fracture or fault.

Byerlee (1978) reported that the friction coefficient is at least 0.85 when the confining pressure is up to 200 MPa, and greater than 0.6 when the confining pressure is higher. However, fractures that contain minerals such as phyllosilicates may have lower friction coefficients (less than 0.6) (Zoback, 2010). Once the ST is determined, the maximum fluid pressure that the fracture can withstand before failing can be recommended. The ST of a fracture is dependent on its orientation relative to the in-situ stresses. The fracture plane's orientation can be determined by the three directional cosines of the unit vector normal to the fault plane, using the principal stress axes as the coordinate system. The shear and effective normal stresses acting on the fracture plane can be computed using Equations 5.19 and 5.20 provided by Jaeger et al. (2007):

$$\tau = \sqrt{n_1^2 n_2^2 \left(\boldsymbol{\sigma}_1 - \boldsymbol{\sigma}_2\right)^2 + n_2^2 n_3^2 \left(\boldsymbol{\sigma}_2 - \boldsymbol{\sigma}_3\right)^2 + n_1^2 n_3^2 \left(\boldsymbol{\sigma}_1 - \boldsymbol{\sigma}_3\right)^2} \tag{5.19}$$

$$\boldsymbol{\sigma}_n' = n_1^2 \boldsymbol{\sigma}_1' + n_2^2 \boldsymbol{\sigma}_2' + n_3^2 \boldsymbol{\sigma}_3' \tag{5.20}$$

5.4. Poromechanical analysis of boreholes in Kuujjuaq, Canada

5.4.1. General background

Kuujjuaq is in a small Inuit community in northern Quebec, Canada. It is located in a tectonically active region of the Canadian Shield, a vast geological formation that covers a large part of North America. The main lithological units outcropping nearby Kuujjuaq are paragneiss and diorite, and they are also accompanied by gabbro, tonalite, and granite (Miranda et al., 2020). There is very limited data on THM properties of rock formations in the studying remote area. Shallow subsurface data and outcrop samples were used by Miranda et al. (2020) to infer the deep geothermal potential beneath the community of Kuujjuaq (Nunavik, Canada). According to the available literature and the preliminary analysis by Miranda et al. (2023a), the geological setting under investigation is believed to be controlled by a strike-slip regime. The results by Miranda et al. (2023a) also show that the old Canadian Shield beneath Kuujjuaq hosts the potential to fulfill the community's annual average heating demand. Deep geothermal energy can be treated as a promising solution to support the energy transition of the Kuujjuaq community. It is preferred to carry out drilling activities in intact rock formations for wellbore stability. However, the target geothermal energy engineering reservoir is within the fault zone, and the rock formation is abundant in natural fractures. It is very likely to drill through natural fractures or to have natural fractures distributed close to the borehole wall. In the present study, we aim to carry out numerical modeling to investigate the performance of wellbores in fractured formations.

5.4.2. Validation of THM coupled FEM solutions

To tackle the complexity and nonlinearity of THM behaviors presented in section 5.3.1, Cacace and Jacquey (2017) created an open-source FEM package named GOLEM that uses the Galerkin finite-element technique to discretize partial differential equations (PDEs). GOLEM investigates groundwater flow, heat, and solute mass transport in fully saturated fractured rocks with elastoplastic mechanical feedback. It was built on the MOOSE (Multiphysics Object Oriented Simulation Environment) framework that can solve the PDEs implicitly using the Newton-Raphson scheme. Previously, GOLEM has

been used to investigate large-scale fault stability and poromechanical effects due to injection activities (Blöcher et al., 2018; Cacace and Jacquey, 2017) but not at the borehole level. The study of wellbore poromechanical analysis has a special requirement on the numerical mesh and the appropriate treatment of boundary conditions. It is therefore necessary to carry out a validation with analytical solutions.

In this part, the FEM modeling of wellbore response is validated using the available thermo-poroelastic analytical solutions of boreholes drilled in a saturated porous media without fractures. The thermo-mechanical properties, in-situ stresses, and formation pore pressure information are chosen based on the study of Miranda et al. (2023b) and included in Table 5.1. The analytical solutions for a non-isothermal state of wellbore drilled in an infinite medium, subjected to a three-dimensional in situ state of stress and pore pressure are presented by Abousleiman and Ekbote (2005). The conditions of a wellbore during drilling in a thermo-poroelastic formation can be broken down into three modes: uniaxial, anti-plane, and modified plane strain. The first and second modes are utterly elastic since they do not initiate the diffusion of fluid or heat. The third mode represents a fully coupled solution of the fluid and heat diffusion with the deformation. A concise expression of the poromechanical solution is given as the following:

$$T = T_o + T^{(2)} \tag{5.21}$$

$$p_f = p_o + p_f^{(2)} + p_f^{(3)} \tag{5.22}$$

$$\sigma_{rr} = \sigma_m - \sigma_d \cos(2\theta) - \sigma_{rr}^{(1)} - \sigma_{rr}^{(2)} - \sigma_{rr}^{(3)} \tag{5.23}$$

$$\sigma_{\theta\theta} = \sigma_m + \sigma_d \cos(2\theta) - \sigma_{\theta\theta}^{(1)} - \sigma_{\theta\theta}^{(2)} - \sigma_{\theta\theta}^{(3)} \tag{5.24}$$

$$\begin{aligned} \sigma_{zz} &= \sigma_V - 2\nu\sigma_m + \nu(\sigma_{rr} + \sigma_{\theta\theta}) \\ &+ \alpha_B(1-2\nu)(p_f - p_o) - \beta_s(1-2\nu)(T - T_o) \end{aligned} \tag{5.25}$$

where T_o and p_o are formation temperature and pore pressure before the excavation. ν is the drained Poisson's ratio of rock. Tensors $\sigma_{rr}^{(1)}, \sigma_{rr}^{(2)}, \sigma_{rr}^{(3)}, \sigma_{\theta\theta}^{(1)}, \sigma_{\theta\theta}^{(2)}, \sigma_{\theta\theta}^{(3)}$, pore pressures

$p_f^{(2)}$, $p_f^{(3)}$, and temperature $T^{(2)}$ are obtained by solving the modified plan strain problem. The complete expressions of pore pressures, temperatures, and tensors are given in Appendix C. The compressive stress is considered positive, and the tensile stress is considered negative for the analysis. The superscripts (1), (2), and (3) represent the solutions of the three loading modes of the modified plane strain problem. *R* is the radius of the well, r and θ are radial coordinates in the wellbore local coordinate. σ_H is the maximum horizontal in-situ stress, σ_h the minimum horizontal in-situ stress, and σ_V is the vertical in-situ stress. At the far field, when $r \to \infty$, the boundary conditions can be assumed around the domain as shown in Figure 5.1.

The terms of σ_m, and σ_d are given as:

$$\sigma_m = \frac{\sigma_H + \sigma_h}{2} \tag{5.26a}$$

$$\sigma_d = \frac{\sigma_H - \sigma_h}{2} \tag{5.26b}$$

The depth of the wellbore was assumed to be 3950 m, where the original formation temperature is 87°C according to the study by Miranda et al. (2023a). The target reservoir at the old Canadian Shield beneath Kuujjuaq is potentially used to fulfill the community's annual average heating demand. The numerical model was first validated without considering the plastic parameters. The time domain solutions are solved by a numerical inversion method (Stehfest, 1970) using MATLAB.

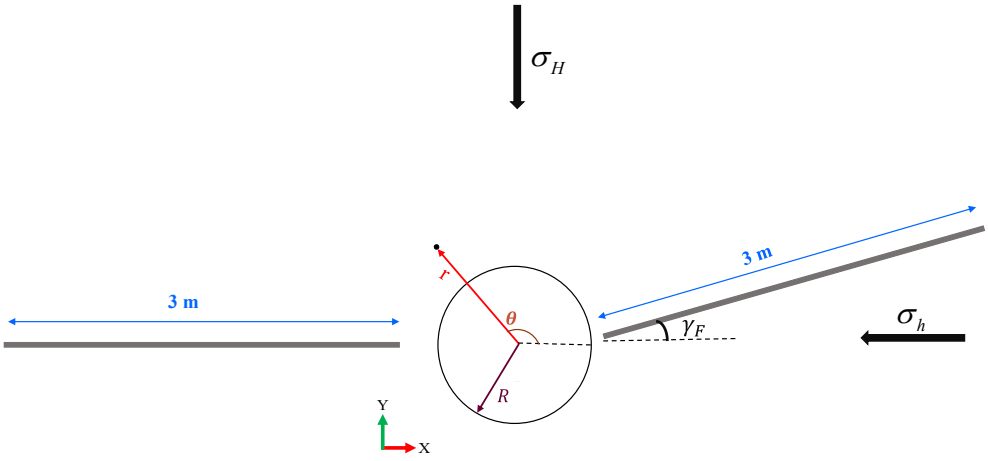

Fig. 5.1. Sketch showing the fracture arrangement and in-situ stress directions (γ_F = fracture inclination).

We applied GOLEM to carry out numerical studies of this thermal-poroelastic problem. The prescribed boundary conditions, the domain size considered for the FEM numerical simulations and the mesh distribution are shown in Figure 5.2. The zero-thickness mesh for fractures is also presented in Figure 5.2d, which is to be used in the subsequent numerical modeling tasks in section 5.4.3. The FEM mesh was generated using Coreform Cubit. For the numerical validation with analytical solutions, fractures were not involved. The numerical domain was chosen to represent a 3D plain strain problem which is to align with the analytical solution by Abousleiman and Ekbote (2005). The comparison between the analytical solutions and the corresponding pore pressure, temperature, effective radial, tangential, and vertical stresses obtained from simulations is displayed in Figure 5.3. Results are plotted along the radial direction when $\theta = 90^{\circ}$ at four different times after exaction. The agreement between the two solutions shows the accuracy of the FEM numerical code.

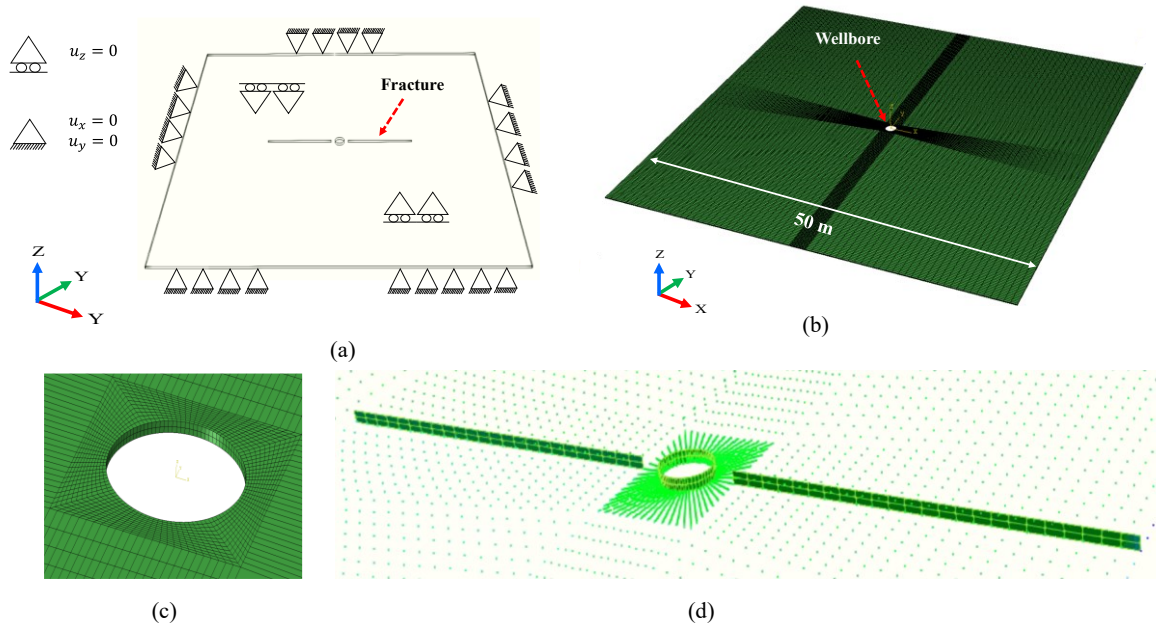

Fig. 5.2. Sketch showing (a) boundary conditions (b) 3D mesh distribution (c) model without fractures and (d) model with fractures.

Table 5.1. In situ stresses and well geometry parameters of the borehole to be drilled in Kuujjuaq, Quebec.

Parameters	**Units**	**Values**	**Parameters**	**Units**	**Values**
Poromechanical Properties			**Thermal Properties**		
Young's modulus, E	GPa	67	Solid thermal expansion, β_s	$1/^{\circ}\mathrm{C}$	3×10^{-5}
Solid modulus, K_s	GPa	231	Fluid thermal expansion, β_f	$1/^{\circ}\mathrm{C}$	9×10^{-5}
Fluid modulus, K_f	MPa	1744	Fluid heat capacity, C_f	$\mathrm{J/kg}^{\circ}\mathrm{C}$	4180
Solid density, ρ_s	$\mathrm{kg/m^3}$	2682	Solid heat capacity, C_s	$\mathrm{J/kg}^{\circ}\mathrm{C}$	895
Fluid density, ρ_f	$\mathrm{kg/m^3}$	1080	Fluid conductivity, λ_f	$\mathrm{J/s\ m}^{\circ}\mathrm{C}$	2.6
Permeability, k	$\mathrm{m^2}$	1×10^{-19}	Solid conductivity, λ_s	$\mathrm{J/s\ m}^{\circ}\mathrm{C}$	0.6
Fluid viscosity, μ_f	Pa.s	3×10^{-4}	Formation temperature, T_o	$^{\circ}\mathrm{C}$	87

Poisson's ratio, ν	-	0.23	**Wellbore**		
Undrained Poisson's ratio, ν_u	-	0.49	Wellbore fluid temperature, T_w	$^{\circ}$C	20
Biot's coefficient, α_B	-	0.81	Wellbore mud density, ρ_w	kg/m^3	1240
Porosity, n	-	0.004	Depth, D	m	3950
Fracture Properties					
Fluid modulus, K_f	MPa	2500	Heat capacity, C_s	J/kg $^{\circ}$C	950
Fluid viscosity, μ_f	Pa.s	3×10^{-4}	Conductivity, λ_s	J/s m $^{\circ}$C	0.65
Permeability, k	m^2	1×10^{-17}	Porosity, n	-	1
In situ stresses					
Vertical stress, σ_V	$\mathrm{MPa.km}^{-1}$	27	Formation pore pressure, p_0	$\mathrm{MPa.km}^{-1}$	10.8
max horizontal stress, σ_H	$\mathrm{MPa.km}^{-1}$	45.3	min horizontal stress, σ_h	$\mathrm{MPa.km}^{-1}$	26.5
Intact Rock Strength parameters					
Cohesion, C	MPa	34	Friction angle, φ	Degree	55

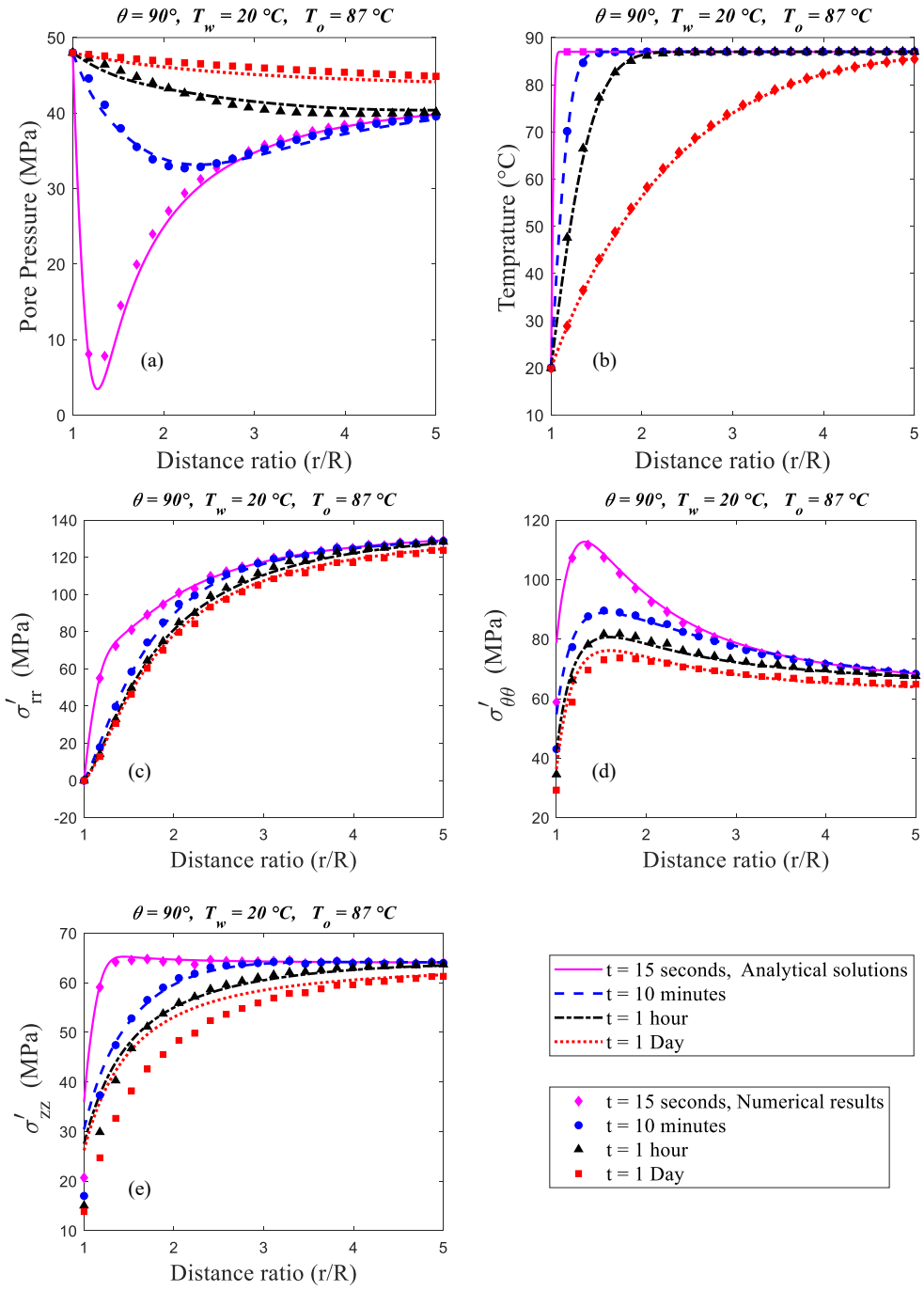

Fig. 5.3. Plots of analytical thermo-poroelastic and modeled results (a) pore pressure (b) Temperature (c) effective radial stress (d) effective tangential stress and (e) effective vertical stress.

5.4.3. Performance of wellbores drilled in fractured formations

We also carried out FEM analysis of poromechanical responses of boreholes drilled in a fractured rock formation. A set of four cases (I to IV) with different fracture inclination angles were chosen as initial models to find out the most critical value for fracture arrangement. The description of each case is summarized in Table 5.2. Simulated effective stresses along fractures were used to quantify the slip tendency (ST) values of different cases.

Table 5.2. Summary of in-situ stress, drilling fluid temperature, and fracture arrangements for different cases of wellbore THM analysis.

Cases	σ_H MPa	σ_h MPa	σ_V MPa	T_w °C	Fracture inclination γ_F (Degree)
I	178.9	104.67	106.65	20	0
II					30
III					45
IV					60
V	178.9	104.67	106.65	87	60
VI				87	No Fracture
VII				20	No Fracture
VIII	152	104.67	106.65	20	60
IX	185				

Fig. 5.4 shows the simulated ST values for cases I to IV. Negligible ST values are noticed for the case with horizontal fractures. By contrast, the case with γ_F = 60 degrees (case IV) shows the highest ST value in the vicinity of the well. In the present study, we are investigating a scenario that fractures are not intersecting with the borehole well surface. Such cases were usually treated as relatively safe ones when compared with cases with

natural fractures intersecting with boreholes. Our numerical results demonstrate the possibility of quantifying ST of specific fractures in the rock formation surrounding a borehole. We will use the subsequent discussion section to highlight the importance of considering flow in fractures when studying the drilling fluid cooling effect.

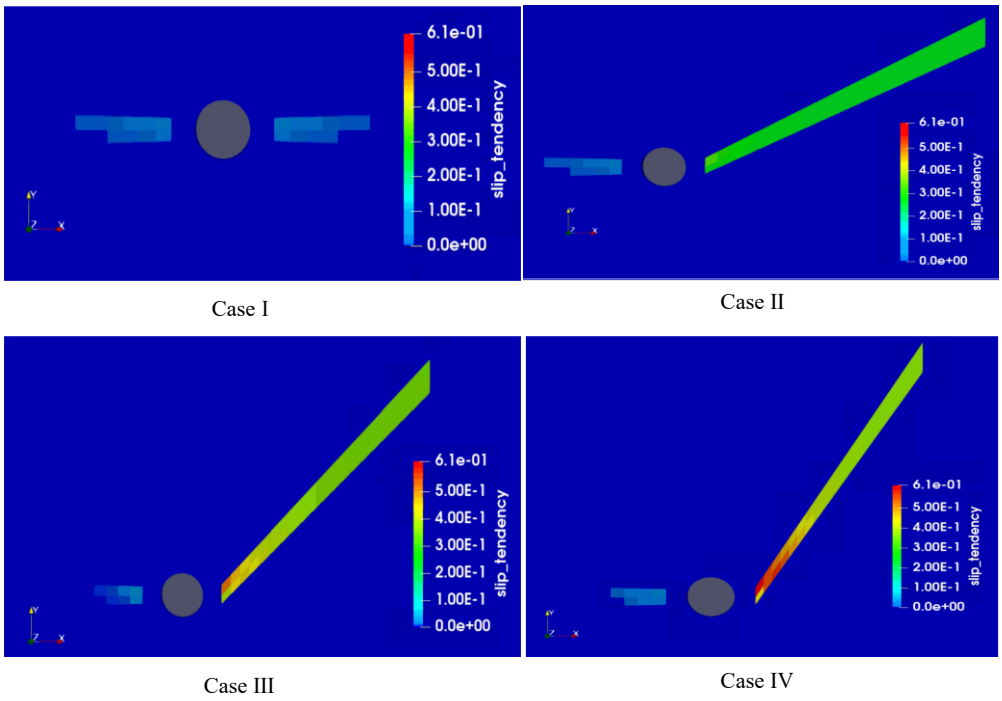

Fig. 5.4. Contours showing slip tendency for different cases at t = 1 day.

5.5. Discussion

5.5.1. Cooling effect

Heat transfer between the drilling fluid and the high temperature reservoir formation can alter the stress field and pore pressure in the vicinity of the well. In our FEM analysis, the thermally driven fluid flow behavior can be well characterized since the thermal convection term is involved in the energy balance equation (Equation 5.7). To demonstrate the significance of the cooling effect in the poromechanical analysis of boreholes in fractured formation, we also carried out numerical modeling of cases with the iso-thermal condition (Table 5.2). We focused on the case of γ_F = 60 degrees since it was shown to be the most important one. Simulated results of ST contours and generated

equivalent plastic strain around boreholes at t = 1 day are presented in Figure 5.5. Shown in Figure 5.5a, ST values of the non-isothermal case are higher than the isothermal case. Simulated plastic strains confirm that the failure tends to appear alongside the direction of the minimum horizontal stress (Figure 5.5b). Figure 5.5b also indicates that the cooling is creating a larger plastic zone and the plastic strain zone is no longer symmetrical when compared with the result from the isothermal case. The side of the well adjacent to the inclined fracture displays larger plastic zones.

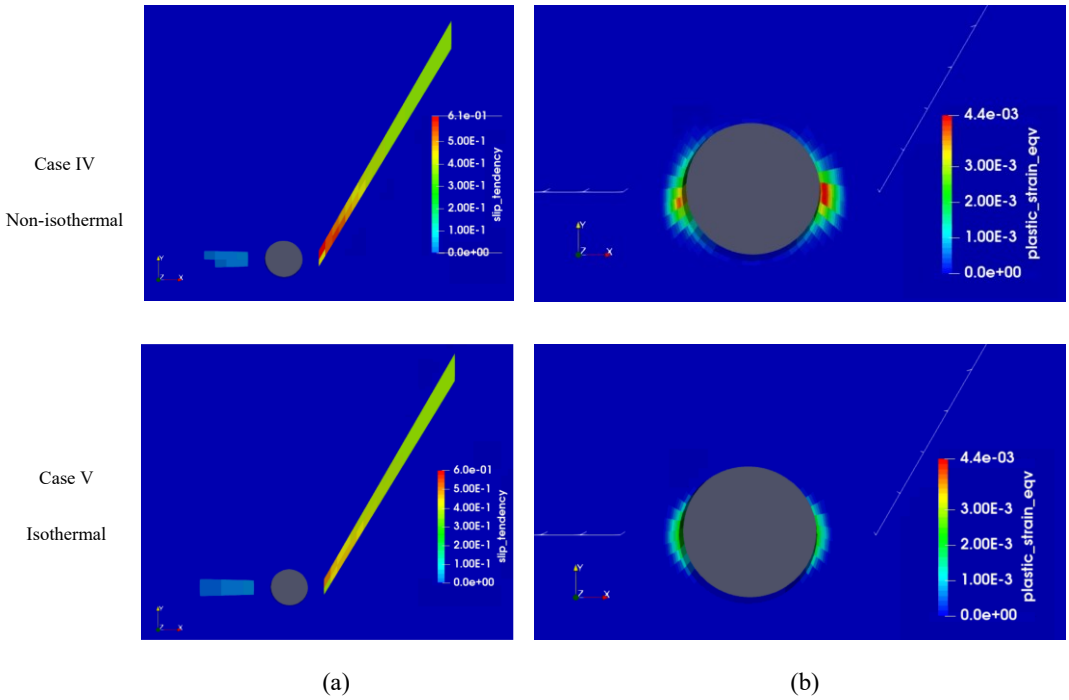

Fig. 5.5. Contours of (a) slip tendency and (b) equivalent plastic strain at t =1 day for non-isothermal and isothermal cases with fractures.

Simulated thermal impact on the developments of pore pressure and effective stresses along the radial direction (when $\theta = 0$) are displayed in Figure 5.6. Shown in Figure 5.6a, the pore pressure from the non-isothermal case is significantly larger than that from the isothermal case in the first 10 minutes. Correspondingly, the effective radial stress close to the borehole for the non-isothermal case generates a large tensile stress at t = 10 seconds

(Figure 5.6b). As shown in Figure 5.6c, the effective tangential stresses are less compressive as compared with the results from the isothermal case. Our results display a similar trend when compared with the research of Nair et al. (2004), which is based on a finite element modeling of homogenized dual-porosity media.

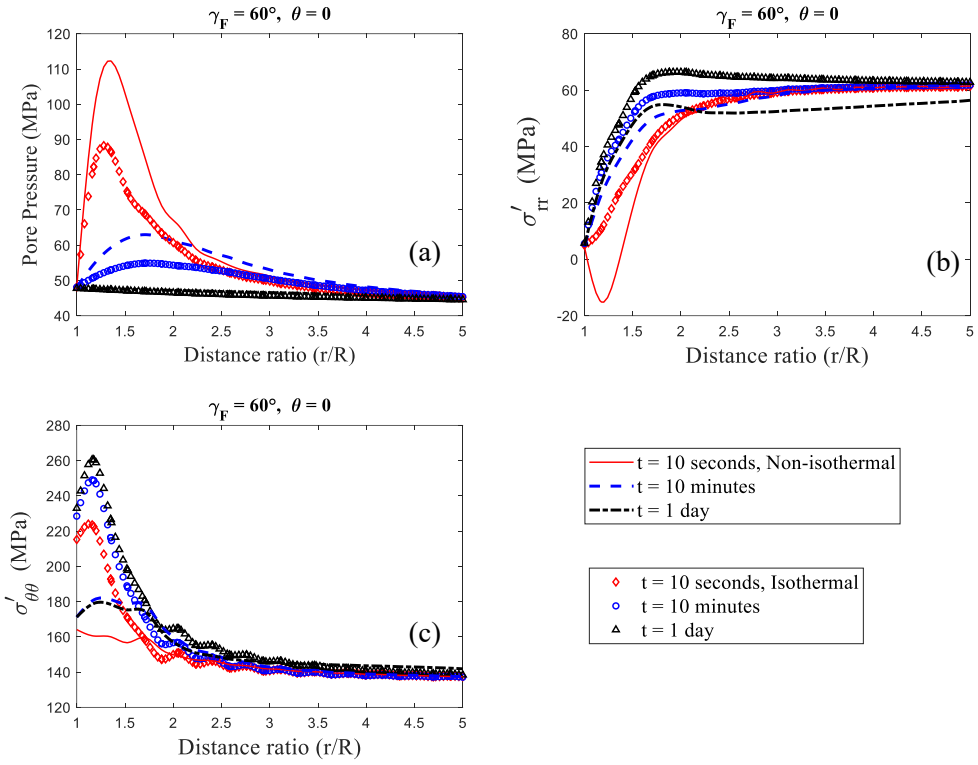

Fig. 5.6. Plots of (a) pore pressure (b) effective radial stress and (c) effective tangential stress for non-isothermal and isothermal cases with fractures (IV and V).

We also carried out numerical modeling of cases without fractures (VI and VII in Table 5.2) to elucidate the thermal impact. Figure 5.7 illustrates the accumulated plastic strain contours at t = 1 day, which shows that the simulated plastic strains for non-isothermal and isothermal cases are comparable. The results were confirmed by the pore pressure and effective stress developments shown in Figure 5.8, which indicates that thermal impact is negligible for the given temperature disturbance when there are no fractures present in the rock formation.

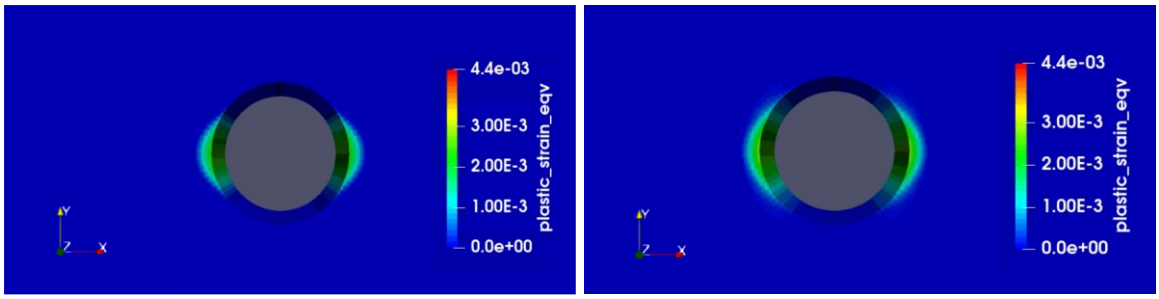

Case VI

Isothermal

Case VII

Non-isothermal

Fig. 5.7. Contours of plastic equivalent strain at t =1 day for isothermal and non-isothermal cases without fractures (VI and VII).

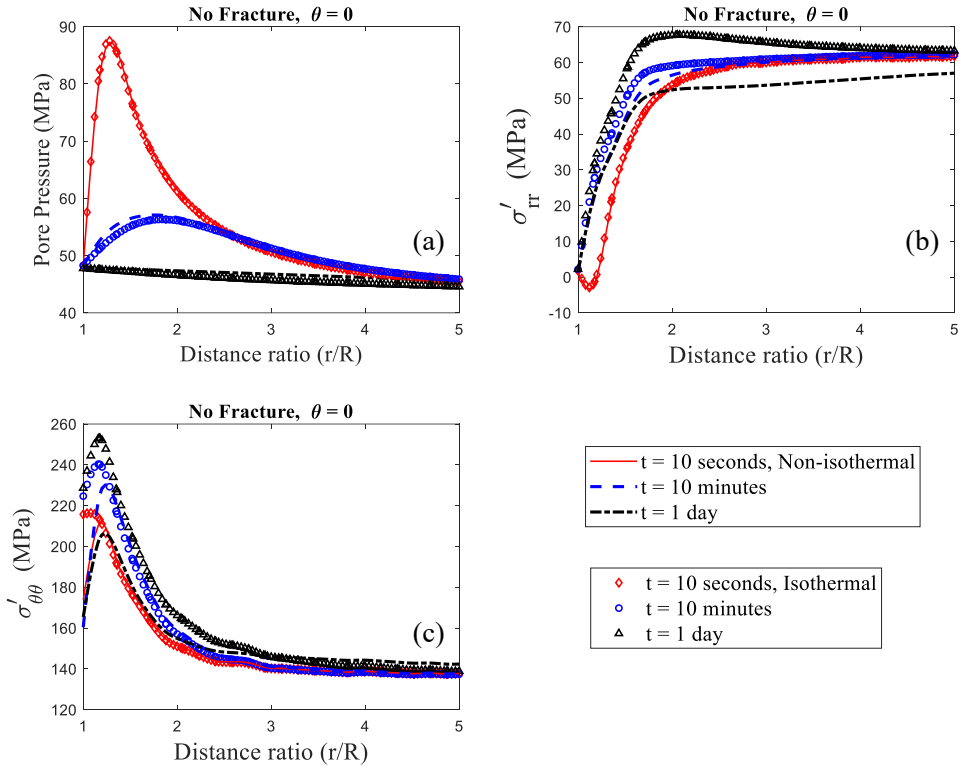

Fig. 5.8. Plots of (a) pore pressure (b) effective radial stress and (c) effective tangential stress for non-isothermal and isothermal cases without fractures (VI and VII).

5.5.2. Effect of in-situ stress

For a deep geological formation considered in this study, there are uncertainties in in-situ stress estimations (Miranda et al., 2023a, 2023b). The variation of in-situ stress can be due to regional heterogeneity in lithology (Liu et al., 2022; Ma et al., 2022) or regional tectonic activities. Particularly, there is a lack of deep geothermal exploratory boreholes in the studying remote northern community. Our applied in-situ stress data is based on the theoretical work by Miranda et al. (2023a). It is necessary to investigate the performance of boreholes under different in-situ stress conditions. As shown in Table 5.2, we also consider two possible cases with a different set of in-situ stress (case VIII: the maximum horizontal stress is decreased to 152 MPa; case IX: the maximum horizontal stress is increased to 185 MPa) to demonstrate the change in the ST values. Results of ST values at t = 1 day are presented in Figure 5.9, which indicates a higher magnitude of ST at a higher σ_H (with a stronger anisotropy of in-situ stresses).

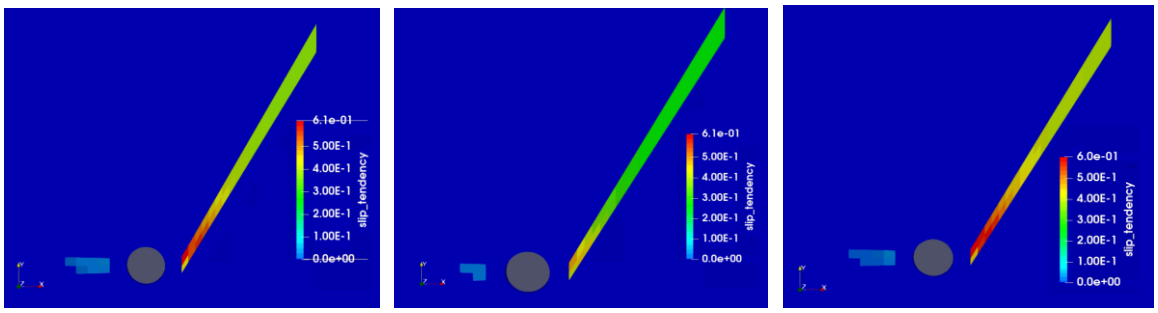

Case IV
σ_H=179 MPa

Case VIII
σ_H=152 MPa

Case IX
σ_H=185 MPa

Fig. 5.9. Contours of slip tendency at t =1 day for cases with different in-situ stresses.

5.6. conclusion

This study focuses on the performance of wellbores to be drilled in a fractured formation for geothermal applications in northern Quebec, Canada. FEM simulations were conducted for the poromechanical analysis of boreholes considering flows in fractures and rock matrix. The presented numerical approaches and findings are also applicable other deep geoenergy engineering projects. Several conclusions are drawn as the following:

- Our findings indicate that sliding can be triggered along tilted fractures even though the fractures are not intersecting with the borehole wall surface. The value of slipping tendency is influenced by the angle of fracture inclination with respect to the direction of the minimum horizontal stress. Inclined fractures exhibit a higher likelihood of slipping in the surrounding area of the well.
- The presence of fractures leads to a significant cooling effect within the formation, which is more pronounced compared to the scenario where there are no fractures. In the case of a fractured model, specifically for non-isothermal conditions, the introduction of low-temperature fluid results in higher ST values. When compared with the isothermal case, the plastic strain zone resulting from the non-isothermal case is no longer symmetrical and has a large area of the plastic zone.
- We investigated the thermal influence on pore pressure and stress. In the non-isothermal case, there is a significant increase in pore pressure compared to the isothermal scenario. Additionally, a large magnitude of tensile stress tends to be generated near the borehole wall in the non-isothermal case.
- In situations where the maximum and minimum horizontal stresses have a significant disparity, the likelihood of slip occurring within fractures increases. This means that fractures that are subjected to high differential stress are more prone to slipping compared to fractures experiencing smaller stress differentials.

Appendix C

Thermo-Poroelastic Solution

The analytical solutions of $T^{(2)}, \sigma_{rr}^{(1)}, \sigma_{rr}^{(2)}, \sigma_{rr}^{(3)}, \sigma_{\theta\theta}^{(1)}, \sigma_{\theta\theta}^{(2)}, \sigma_{\theta\theta}^{(3)}, p_f^{(2)},$ and $p_f^{(3)}$ in the Laplace domain are given as follows (Abousleiman and Ekbote, 2005)

$$\overline{T}^{(2)} = \frac{1}{s}\left\{\left(T_w - T_o\right)\Phi\left[\omega\right]\right\} \tag{C1}$$

$$\overline{\sigma}_{rr}^{(1)} = \left(\sigma_m - p_w\right)\frac{R^2}{r^2}H\left(t\right) \tag{C2}$$

$$\overline{\sigma}_{\theta\theta}^{(1)} = -\left(\sigma_m - p_w\right)\frac{R^2}{r^2}H\left(t\right) \tag{C3}$$

$$\overline{\sigma}_{rr}^{(2)} = -\frac{1}{s}\left[\ 2\chi_t\left\{F_1\Lambda\left[\xi\right] + F_2\Lambda\left[\omega\right]\right\} + \beta^s\left(\frac{1-2\nu}{1-\nu}\right)\left(T_w - T_o\right)\Lambda\left[\omega\right]\right] \tag{C4}$$

$$\overline{\sigma}_{\theta\theta}^{(2)} = \frac{1}{s}\begin{bmatrix} 2\chi_t\left\{F_1\left(\Phi\left[\xi\right] + \Lambda\left[\xi\right]\right) + F_2\left(\Phi\left[\omega\right] + \Lambda\left[\omega\right]\right)\right\} \\ -\beta^s\left(\frac{1-2\nu}{1-\nu}\right)\left(T_w - T_o\right)\left(\Phi\left[\omega\right] + \Lambda\left[\omega\right]\right) \end{bmatrix} \tag{C5}$$

$$\overline{\sigma}_{rr}^{(3)} = -\frac{\sigma_d}{s}\left[\ \frac{B\left(1+\nu_u\right)}{3\left(1-\nu_u\right)}C_1\psi\left[\xi\right] + \frac{1}{\left(1-\nu_u\right)}C_2\frac{R^2}{r^2} + 3C_3\frac{R^4}{r^4}\right]\cos\left(2\theta\right) \tag{C6}$$

$$\overline{\sigma}_{\theta\theta}^{(3)} = \frac{\sigma_d}{s}\left[\ \frac{B\left(1+\nu_u\right)}{3\left(1-\nu_u\right)}C_1\Omega\left[\xi\right] + 3C_3\frac{R^4}{r^4}\right]\cos\left(2\theta\right) \tag{C7}$$

$$\overline{p}_f^{(2)} = \frac{1}{s}\left\{F_1\Phi\left[\xi\right] + F_2\Phi\left[\omega\right]\right\} \tag{C8}$$

$$\overline{p}_f^{(3)} = \frac{\sigma_d}{s}\left[\frac{B^2\left(1-\nu\right)\left(1+\nu_u\right)^2}{9\left(1-\nu_u\right)\left(\nu-\nu_u\right)}C_1K_2\left[\xi r\right] + \frac{B\left(1+\nu_u\right)}{3\left(1-\nu_u\right)}C_2\frac{R^2}{r^2}\right]\cos\left(2\theta\right) \tag{C9}$$

where $H(\bullet)$ is the Heaviside unit step function, s is the Laplace transform variable, $\bar{\bullet}$ denotes the Laplace transformation, and K_n is the modified Bessel function of the second kind of nth order. T_w is the wellbore fluid temperature, B is the Skempton coefficient, and ν_u is the undrained Poisson's ratio of rock.

$$\xi = \sqrt{\frac{s}{c_f}}, \quad \omega = \sqrt{\frac{s}{c_h}} \tag{C10}$$

c_h and c_f are the heat and fluid diffusivities obtained as:

$$c_h = \frac{\lambda_b}{(\rho C)_b} \tag{C11}$$

$$c_f = \frac{2G\mathcal{K}(1-\nu)(\nu_u-\nu)}{\alpha_B{}^2(1-2\nu)^2(1-\nu_u)} \tag{C12}$$

$$\chi_t = \alpha_B \frac{1-2\nu}{2(1-\nu)} \tag{C13}$$

$$F_1 = \left[(p_w - p_o) - \left(\frac{c_{hf}}{(1-c_f/c_h)} \right)(T_w - T_o) \right] \tag{C14}$$

$$F_2 = \left(\frac{c_{hf}}{(1-c_f/c_h)} \right)(T_w - T_o) \tag{C15}$$

c_{hf} is a coupling constant given by:

$$c_{hf} = \frac{c_f}{\mathcal{K}} \left(\beta^{sf} - \alpha_B \beta_s \left(\frac{1+\nu}{1-\nu} \right) \right) \tag{C16}$$

G is the shear modulus and $\mathcal{K}$ is the fluid mobility adopted as:

$$\mathcal{K} = \frac{k}{\mu} \tag{C17}$$

β^{sf}, and β^{s} are thermic coefficient found by:

$$\beta^{sf} = 3\alpha_B \beta_s + n\left(\beta_f - 3\beta_s\right) \tag{C18}$$

$$\beta^{s} = \frac{2G(1+\nu)}{(1-2\nu)}\beta_s \tag{C19}$$

$$\Phi[x] = \frac{K_0[xr]}{K_0[xR]} \qquad x = \xi\ ,\ \omega \tag{C20}$$

$$\Lambda[x] = \frac{K_1[xr]}{xrK_0[xR]} - \frac{RK_1[xR]}{xr^2K_0[xR]} \qquad x = \xi\ ,\ \omega \tag{C21}$$

$$\psi[x] = \frac{1}{xr}K_1[\mathrm{xr}] + \frac{6}{(\mathrm{xr})^2}K_2[\mathrm{xr}] \qquad x = \xi\ ,\ \omega \tag{C22}$$

$$\Omega[x] = \frac{1}{xr}K_1[\mathrm{xr}] + \left(1 + \frac{6}{(\mathrm{xr})^2}\right)K_2[\mathrm{xr}] \qquad x = \xi\ ,\ \omega \tag{C23}$$

In which

$$C_1 = \frac{12\xi R(1-\nu_u)(\nu_u - \nu)}{B(1+\nu_u)(D_2 - D_1)} \tag{C24}$$

$$C_2 = \frac{4(1-\nu_u)D_2}{(D_2 - D_1)} \tag{C25}$$

$$C_3 = -\frac{\xi R(D_2 + D_1) + 8(\nu_u - \nu)K_2[\xi R]}{\xi R(D_2 - D_1)} \tag{C26}$$

And

$$D_1 = 2(\nu_u - \nu)K_1[\xi R] \tag{C27}$$

$$D_2 = \xi R(1-\nu)K_2[\xi R] \tag{C28}$$

Chapter 6

Conclusions and future work

6.1. Summary and conclusions

Upon thorough examination of diverse geological and mechanical facets in different rock formations, a comprehensive understanding of their behaviors and responses to various stress conditions emerges. The petrophysical characterizations of glutenite cores reveal the prevalence of laumontite minerals, accompanied by well-aligned pore spaces around large aggregates. This structural arrangement, indicative of strong confining pressure dependence, contributes to the rock's intricate mechanical behaviors. At low confining pressures, the rock exhibits strain hardening followed by post-peak softening behavior, while higher confining pressures lead to a transition from dilation to compression.

The utilization of a thermomechanics-based viscoplastic model aptly captures the complex constitutive behavior, considering both thermodynamic laws and the non-associated flow rule. This model is particularly advantageous in numerical simulations, as evidenced by plastic zone development around boreholes in over pressured reservoirs. The broader applicability of this model extends to deep geo-energy production and geological engineering projects involving similar soft rock formations.

Turning to Ordovician limestone, extensive laboratory characterizations reveal the prevalence of calcite and dolomite as dominant minerals. This limestone exhibits strain hardening under high confining pressures, coupled with linear elastic behavior before yielding. The dual-porosity theories offers a more accurate stress analysis by accounting for diffusion between rock matrix and fractures. These theories shed light on significant stress differentials between matrix and fractures during early excavation periods, underscoring the need for precise in-situ stress characterization for successful project execution.

Notably, the poromechanical analysis of borehole stability in fractured porous media highlights the critical role of fracture strength in borehole failure and drilling bit jamming. Sliding along tilted fractures, even without direct intersection with borehole surfaces, underscores the essential role of fracture inclination angle with respect to the minimum horizontal stress direction. This dynamic introduces the possibility of slipping in inclined fractures surrounding wells.

Thermal effects further complicate the complexity of rock behaviors. Fractures induce substantial cooling within formations, yielding distinctive plastic strain zones under non-isothermal conditions. The interaction between thermal conditions and pore pressure also emerges as a critical factor, with non-isothermal scenarios displaying heightened pore pressure and differential stress. The presence of significant disparities between maximum and minimum horizontal stresses exacerbates the likelihood of fractures slipping, underscoring the importance of stress differentials in fracture behavior.

In summary, the integration of these conclusions underscores the multifaceted nature of rock behavior under varying stress conditions. These findings have far-reaching implications for geological engineering projects, as a comprehensive understanding of mechanical, thermal, and structural interactions is essential for ensuring successful outcomes and sustainable practices.

6.2. Recommendations for future works

Based on the findings and conclusions presented in the three papers, several recommendations can be made for future research in the field:

- Further Exploration of Rock Formation Characteristics: Conduct more extensive petrophysical characterizations to understand the mineral compositions, micro-structures, and pore space distribution in different rock formations. This will provide a solid foundation for developing accurate constitutive models and understanding their mechanical behavior under varying stress conditions.
- Refinement and validation of modeling approaches: Continue refining and validating thermomechanics-based viscoplastic models, dual-porosity poroelastic

solutions, and finite element simulations to capture the complex behaviors of tight rocks, fractured porous media, and deep geo-energy systems. Incorporate more experimental data and field observations to improve the accuracy and reliability of the models.

- Consideration of fracture strength and In-Situ Stress characterization: In the analysis of borehole stability in fractured formations, give special attention to fracture strength and accurately characterize in-situ stress directions and magnitudes. This will enable a better understanding of stress distributions and potential failure mechanisms, leading to more effective designs and operational strategies.
- Investigation of non-isothermal conditions: further explore the influence of non-isothermal conditions on the mechanical behavior and performance of rock formations. Investigate the effects of thermal gradients, temperature changes, and heat transfer mechanisms on pore pressure, stress distribution, and plastic strain zones. This will provide insights into the thermal behavior of deep geo-energy systems and help optimize their performance.
- Integration of multiphysics coupling: Explore the coupling effects between different physical processes such as thermal, hydraulic, mechanical, and chemical behaviors in rock formations. Develop integrated modeling frameworks that consider the interactions and feedback mechanisms among these processes to provide a comprehensive understanding of the behavior of deep geo-energy systems and enhance their design and operation.
- Field validation and case Studies: Conduct field validation studies and case studies to verify the effectiveness and applicability of the developed models and approaches. Collaborate with industry partners and researchers to gather real-world data and validate the predictive capabilities of the models in different geological settings and operational conditions.
- By addressing these recommendations, future research can further advance our understanding of rock formation behavior, improve the accuracy of modeling approaches, and contribute to the design and optimization of deep geo-energy projects and geological engineering endeavors.

Appendix D

Validation of Dual Porosity Code

In this section, the dual-porosity code is verified against the closed form solutions of transversely isotropic poroelastic materials provided by Abousleiman and Cui (1998). Mathematically, the dual-porosity solution should collapse to single porosity if the parameters that represent the fractures approach rock matrix values or zero. A very large stiffness in the fractures $K^{\mathrm{II}} \to K_s$, which makes the fracture's Biot modulus tends to zero $\left(\alpha^{\mathrm{II}} \to 0\right)$, small amount of fracture permeability $k^{\mathrm{II}} \to 0$, and no interflow term $\Gamma \to 0$ must be assumed. Dual porosity MATLAB code (Heidari et al., 2021) is used to verify reduced dual porosity results for the inclined wellbore problem as presented in Abousleiman and Cui (1998). The far-field in situ stress, formation pore pressure gradients, and Poromechanical parameters adopted for the analysis are shown in Table D.1. The radius of the borehole was assumed to be $R = 0.1\mathrm{m}$. The deviation of the borehole was defined by $\varphi_b = 30^\circ$, and $\gamma_b = 60^\circ$. The depth of the formation was assumed to be 1000 m. In this example only the case of an excavation was analyzed which means the well pressure was assumed to be zero. The results of dual porosity code are presented in Figure D.1. Comparison of the generated pore pressure and effective stresses in this way serves as validation of the dual-porosity solution solved by MATLAB.

Table D.1. Poromechanical parameters of the borehole used for reduced dual porosity validation; single porosity data from Abousleiman and Cui (1998)

Parameters	Units	Values	Parameters	Units	Values
Reduced Dual Porosity					
Matrix bulk modulus, K^{I}	GPa	11	Matrix permeability, k^{I}	m^2	9.8692×10^{-20}
Matrix shear modulus, G^{I}	GPa	8.66	Matrix Biot's coefficient, α^{I}	-	0.78

Poisson's ratio, ν	-	0.189	Matrix porosity, ϕ^{I}	-	0.02
Solid modulus, K_s	GPa	48.2	Fracture permeability, k^{II}	m^2	9.8692×10^{-26} (Small value)
Fluid bulk modulus, K_f	MPa	419	Fracture Biot's coefficient, α^{II}	-	0.001 (Small value)
Fracture bulk modulus, K^{II}	GPa	48.2 (Large value)	Fracture porosity, ϕ^{II}	-	1×10^{-10} (Small value)
Fracture shear modulus, G^{II}	GPa	38 (Large value)	Interporosity flow, Γ	$(\mathrm{MPa.s})^{-1}$	1×10^{-10} (Small value)
Mud Density, ρ_w	kg/m^3	0	Fluid viscosity, μ	Pa.s	0.001
In situ stresses			**Wellbore**		
Vertical stress, σ_V	$\mathrm{MPa.km}^{-1}$	25	Radius, R	m	0.1
Maximum horizontal stress, σ_H	$\mathrm{MPa.km}^{-1}$	29	Azimuth, φ_b	Degree	30
Minimum horizontal stress, σ_h	$\mathrm{MPa.km}^{-1}$	20	Inclination, γ_b	Degree	60
Formation pore pressure, p_0	$\mathrm{MPa.km}^{-1}$	9.8	Depth, D	m	1000

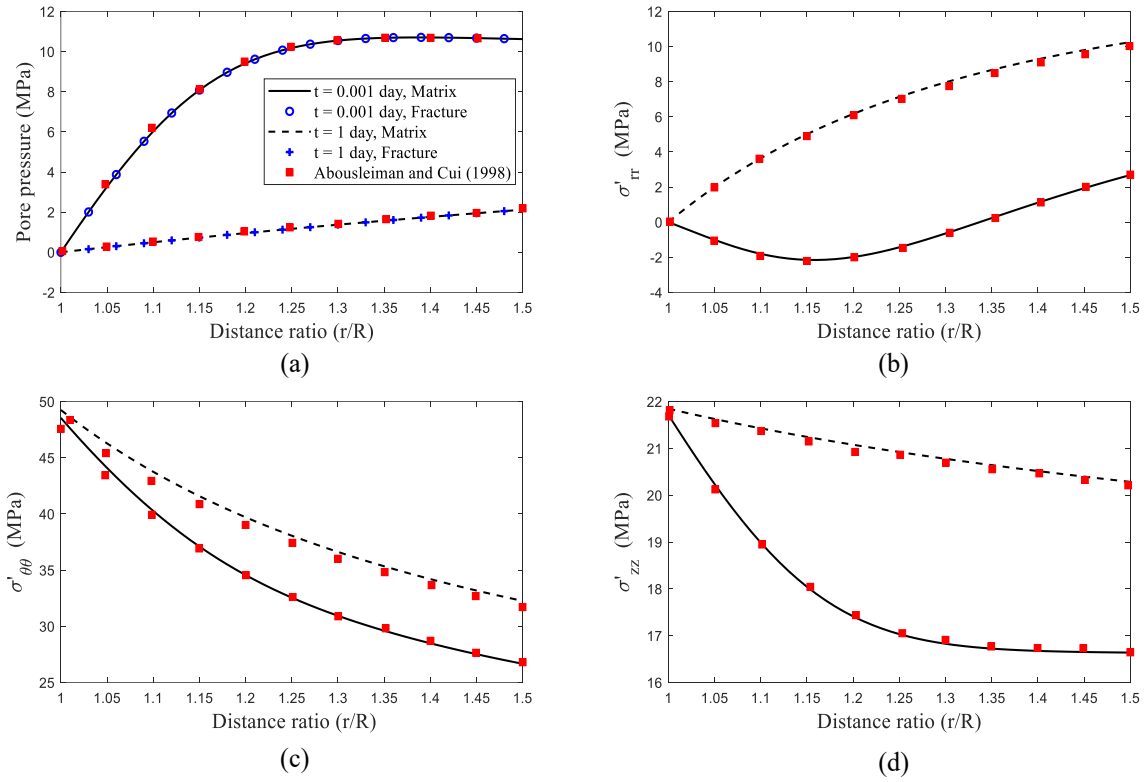

Fig. D.1. Dual porosity validation; distributions of (a) pore pressure, (b) radial, (c) tangential, and (d) vertical effective stresses at two different times.

Appendix E

Benchmark verification of THM numerical modeling

Case1: Thermal conduction

Conduction problem is solved as a first example in which a sudden rise of temperature is applied at the boundary of a semi-infinite saturated media. The initial and fixed Dirichlet boundary conditions are prescribed as $T\left(x>0,t=0\right)=T_0$ and $T\left(x=0,t>0\right)=T_\infty$.

By neglecting the convective heat transfer, the analytical solution by McTigue (1986) can be expressed as:

$$T\left(x,t\right)=T_\infty+\left(T_0-T_\infty\right)erfc\left(\frac{x}{2\sqrt{c_h t}}\right) \tag{E1}$$

The input parameters are illustrated in Table D.1. The modeled results are depicted in Figure D.1. It is noticeable that the observed temperature migration corresponds satisfactorily with the analytical solution. Furthermore, the outcomes indicated that applying heat to the boundary can result in the generation of excess pressure in the poroelastic medium due to the difference in thermal expansion coefficients between the solid and fluid.

Table E.1. Solid and pore fluid properties used in case 1.

Property	Value	Unit	Property	Value	Unit
Porosity, n	0.42	-	Fluid heat capacity, C_f	4200	J/kg $^\circ$C
Soil density, ρ_s	2720	kg/m^3	Soil heat capacity, C_s	710	J/kg $^\circ$C
Fluid density, ρ_f	1000	kg/m^3	Soil conductivity, λ_s	3.6	J/s m $^\circ$C

T_0	120	˚C	Fluid conductivity, λ_f	0.57	J/s m ˚C
T_∞	30	˚C	Poison ratio, ν	0.2	-

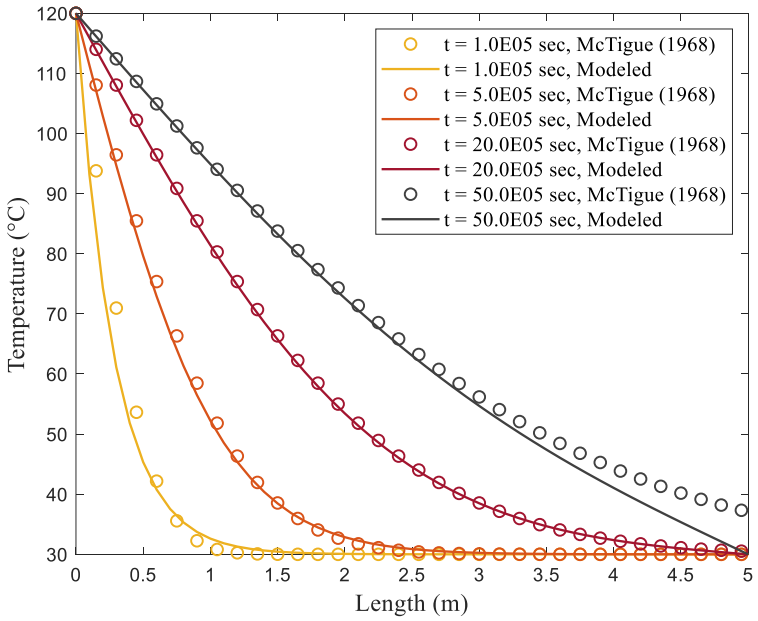

Fig. E.1. Profiles of temperature versus distance at four different times for case 1.

Case 2: THM validation

Lewis and Cherfler (1998) used an example of thermo-elastic consolidation of a saturated soil column as a benchmark for THM simulations. The example involves subjecting a linear elastic soil column to a constant pressure and temperature. The geometry of the column is shown in Figure E.2, and the initial water pressure and temperature in the problem domain are assumed to be zero. The top surface of the column has a fixed temperature of 50°C and no pore pressure. Additionally, a surface traction of 1000 Pa is applied. The side boundaries can only move vertically, while the bottom boundary is

restricted from moving at all. The properties of the soil and pore fluid used in this case can be found in Table E.2.

Table E.2. Soil and pore fluid properties used in case 2 from Lewis and cherfler (1998)

Property	**Value**	**Unit**	**Property**	**Value**	**Unit**
Young's modulus, E	6000	kPa	Soil thermal expansion, β_s	9×10^{-7}	$1/^{\circ}\mathrm{C}$
Porosity, n	0.1	-	Fluid heat capacity, C_f	0.04	J/kg $^{\circ}$C
Fluid viscosity, μ_f	0.001	Pa.s	Soil heat capacity, C_s	0.02	J/kg $^{\circ}$C
Soil density, ρ_s	2000	kg/m^3	Fluid Conductivity, λ_f	0.2	J/s m $^{\circ}$C
Fluid density, ρ_f	1000	kg/m^3	Soil Conductivity, λ_s	0.2	J/s m $^{\circ}$C
Poison ratio, ν	0.4	-	Permeability, k	4×10^{-12}	m^2

Figures E.3 and E.4 show the changes in temperature, pore water pressure, and vertical displacement over time. Results from Lewis and Cherfler (1998) were compared with the nodal points shown in Figure E.2. The maximum pore water pressure was observed to be 1000 Pa at all nodal points initially, followed by gradual dissipation. Due to the consolidation of soil column caused by the dissipation of pore water pressure, settlement occurred at every point, however the increase in temperature compensated for some of the settlement by causing expansion.

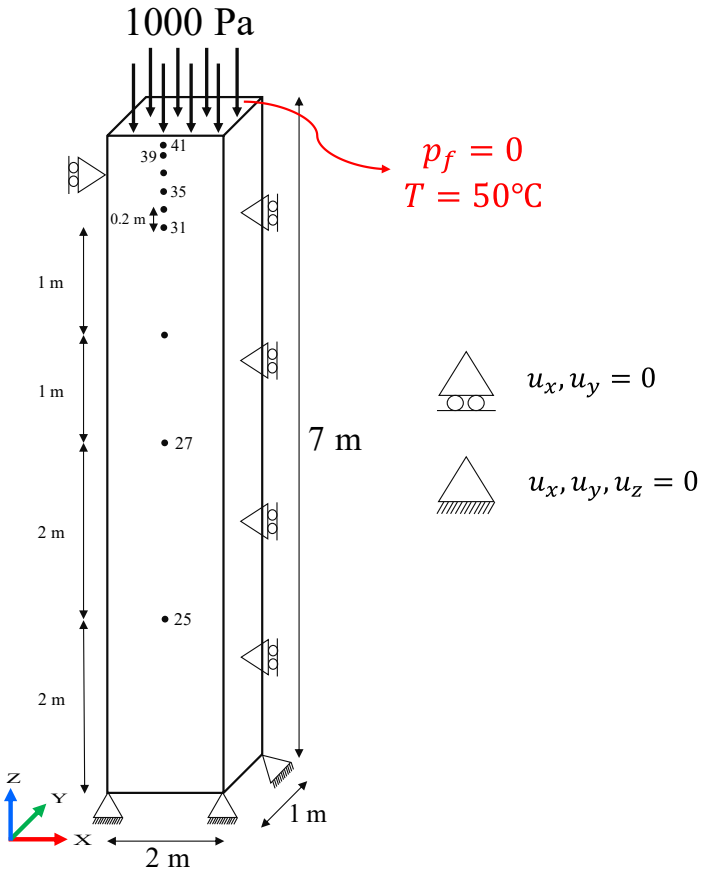

Fig. E.2. Geometry of case 2 along with the boundary conditions modified after Iranmanesh and Pak (2018)

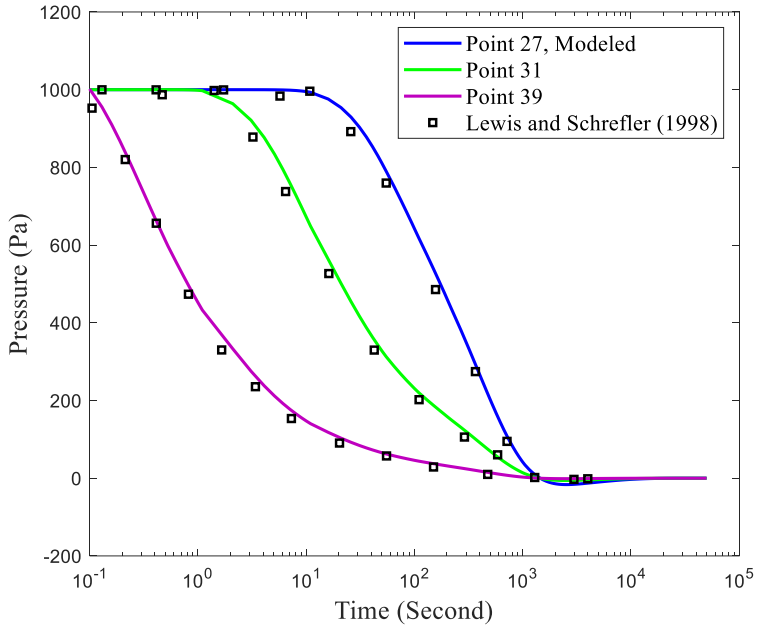

Fig. E.3. Pore pressure versus time of different nodes for case 2

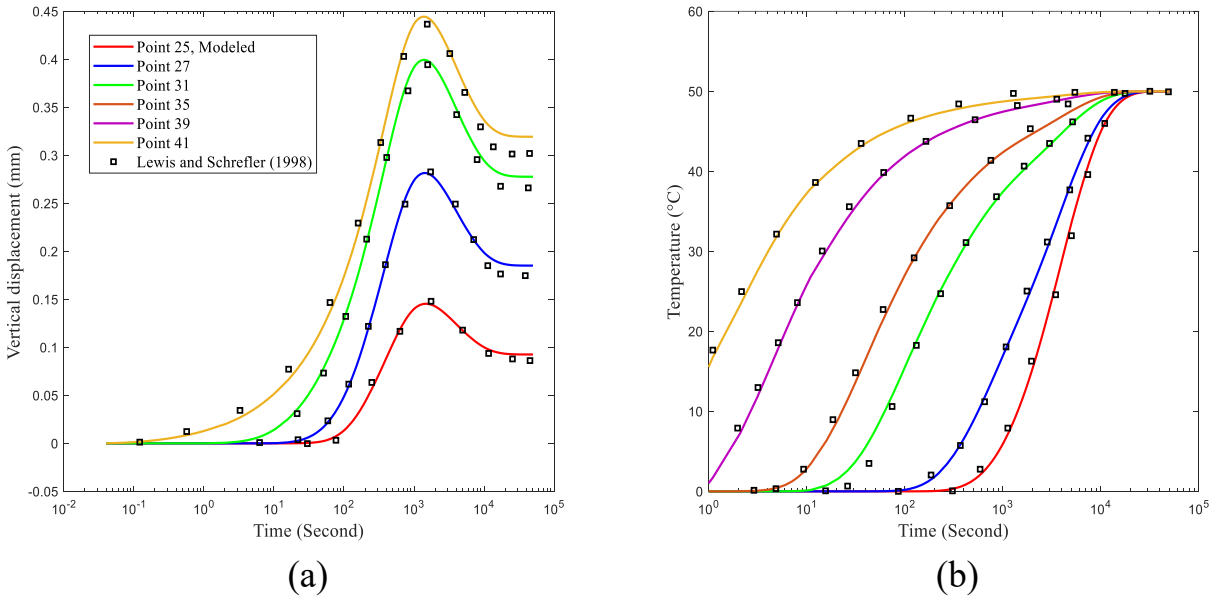

Fig. E.4. (a) Displacement, and (b) temperature versus time at different nodes for case 2

References

Aadnoy, B. S., & Ong, S. (2003). Introduction to special issue on Borehole Stability. *Journal of Petroleum Science and Engineering*, *38*(3–4), 79–82. https://doi.org/10.1016/s0920-4105(03)00022-6

Abaqus, (2016). Abaqus Theory Manual. Simulia, Version 6.16.

Abdollahipour, A., Soltanian, H., Pourmazaheri, Y., Kazemzadeh, E., & Fatehi-Marji, M. (2019). Sensitivity analysis of geomechanical parameters affecting a wellbore stability. *Journal of Central South University*, *26*(3), 768–778. https://doi.org/10.1007/s11771-019-4046-2

Abousleiman, Y., & Cui, L. (1998). Poroelastic solutions in transversely isotropic media for wellbore and cylinder. *International Journal of Solids and Structures*, *35*(34–35), 4905–4929. https://doi.org/10.1016/S0020-7683(98)00101-2

Abousleiman, Y., & Ekbote, S. (2005). Solutions for the inclined borehole in a porothermoelastic transversely isotropic medium. *Journal of Applied Mechanics, Transactions ASME*, *72*(1), 102–114. https://doi.org/10.1115/1.1825433

Abousleiman, Y., & Nguyen, V. (2005). Poromechanics Response of Inclined Wellbore Geometry in Fractured Porous Media. *Journal of Engineering Mechanics*, *131*(11), 1170–1183. https://doi.org/10.1061/(asce)0733-9399(2005)131:11(1170)

Aifantis EC (1979). On the response of fissured rocks. *Developments Mechanics* 10:249–253

Akhtar, S., & Li, B. (2020). Numerical Analysis of Pipeline Uplift Resistance in Frozen Clay Soil Considering Hybrid Tensile-Shear Yield Behaviors. *International Journal of Geosynthetics and Ground Engineering*, *6*(4), 1–12. https://doi.org/10.1007/s40891-020-00228-9

Allen RF, Baldini NC, Donofrio PE, Gutman EL, Keefe E, Kramer JG, Leinweber CM, Mayer VA (1988). *Annual book of ASTM standards.* ASTM, West Conshohocken, PA

An, M., Zhang, F., Chen, Z., Elsworth, D., & Zhang, L. (2020). Temperature and Fluid Pressurization Effects on Frictional Stability of Shale Faults Reactivated by Hydraulic Fracturing in the Changning Block, Southwest China. *Journal of Geophysical Research: Solid Earth*, *125*(8), 1–14. https://doi.org/10.1029/2020JB019584

An, M., Zhang, F., Elsworth, D., Xu, Z., Chen, Z., & Zhang, L. (2020). Friction of Longmaxi Shale Gouges and Implications for Seismicity During Hydraulic Fracturing. *Journal of Geophysical Research: Solid Earth*, *125*(8). https://doi.org/10.1029/2020JB019885

An, M., Zhang, F., Min, K., Elsworth, D., Marone, C., & He, C. (2021). The Potential for Low-Grade Metamorphism to Facilitate Fault Instability in a Geothermal Reservoir. *Geophysical Research Letters*, *48*(11), e2021GL093552.

Baik, M., Lee, S., & Shon, W. (2009). Retention of uranium (VI) by laumontite, a fracture-filling material of granite. *Journal of Radioanalytical and Nuclear Chemistry*, *280*(1), 69–77.

Baud, P., Vajdova, V., & Wong, T. F. (2006). Shear-enhanced compaction and strain localization: Inelastic deformation and constitutive modeling of four porous sandstones. *Journal of Geophysical Research: Solid Earth*, *111*(12), 1–17. https://doi.org/10.1029/2005JB004101

Berre, I., Doster, F., & Keilegavlen, E. (2019). Flow in fractured porous media: A review of conceptual models and discretization approaches. *Transport in Porous Media*, *130*(1), 215–236.

Biot, M.A. (1956). General solutions of the equations of elasticity and consolidation for a porous material. *J. Appl. Mech*. 23(1), 91–96.

Blöcher, G., Cacace, M., Jacquey, A. B., Zang, A., Heidbach, O., Hofmann, H., Kluge, C., & Zimmermann, G. (2018). Evaluating Micro-Seismic Events Triggered by Reservoir Operations at the Geothermal Site of Groß Schönebeck (Germany). *Rock Mechanics and Rock Engineering*, *51*(10), 3265–3279. https://doi.org/10.1007/s00603-018-1521-2

Bradford, I. D. R., & Cook, J. M. (1994). A semi-analytic elastoplastic model for wellbore stability with applications to sanding. In *Rock Mechanics in Petroleum Engineering* (p. SPE-28070-MS). https://doi.org/10.2118/28070-MS

Bradley, W. B. (1978). Failure of Inclined Boreholes. *American Society of Mechanical Engineers (Paper)*, *101*(78-Pet-44), 232–239.

Bravo, A., Jerez, O., Kelm, U., & Poblete, M. (2017). Dehydration-hydration reactivity of laumontite: analyses and tests for easy detection. *Clay Minerals*, *52*(3), 315–327.

Byerlee, J. (1978). Friction of rocks. *Pure and Applied Geophysics*, *116*(4), 615–626. https://doi.org/10.1007/BF00876528

Cacace, M., & Jacquey, A. B. (2017). Flexible parallel implicit modelling of coupled thermal-hydraulic-mechanical processes in fractured rocks. *Solid Earth*, *8*(5), 921–941. https://doi.org/10.5194/se-8-921-2017

Chen, B., Xu, B., Li, B., Kong, M., Wang, W., & Chen, H. (2020). Understanding the performance of hydraulically fractured wells in the laumontite-rich tight glutenite formation. *Journal of Petroleum Science and Engineering*, *185*. https://doi.org/10.1016/j.petrol.2019.106600

Chen, S. L., & Abousleiman, Y. N. (2017). Wellbore stability analysis using strain hardening and/or softening plasticity models. *International Journal of Rock Mechanics and Mining Sciences*, *93*(January), 260–268. https://doi.org/10.1016/j.ijrmms.2017.02.007

Chen, S. L., Abousleiman, Y. N., & Muraleetharan, K. K. (2012). Closed-form elastoplastic solution for the wellbore problem in strain hardening/softening rock formations. *International Journal of Geomechanics*, *12*(4), 494–507.

Chen, S., Xiang, H., Li, B., & Xu, B. (2022). Geomechanical Dilation Assisted VHSD Process in Altered-Stress Mature Oilsands Reservoir: Geomechanical Studies and Field Experiences. *56th US Rock Mechanics/Geomechanics Symposium*.

Chen, X., Li, S., Zhang, J., Wang, S., Gui, F., & Younessi, A. (2020). 3D Geomechanical Modeling for an Extra Deep Fractured Carbonate Reservoir, Northwest China. In *SPE Asia Pacific Oil & Gas Conference and Exhibition* (p. D013S101R019). https://doi.org/10.2118/202334-MS

Chen, X., Tan, C. P., & Haberfield, C. M. (1996). Wellbore stability analysis guidelines for practical well design. *SPE - Asia Pacific Oil & Gas Conference*, 117–126. https://doi.org/10.2118/36972-ms

Collins, I. F. (2003). A systematic procedure for constructing critical state models in three dimensions. *International Journal of Solids and Structures*, *40*(17), 4379–4397.

Cui, L., Cheng, A. H. D., & Abousleiman, Y. (1997). *Poroelastic solution for an inclined borehole*.

Dashti, R., Rahimpour-Bonab, H., & Zeinali, M. (2018). Fracture and mechanical stratigraphy in naturally fractured carbonate reservoirs-A case study from Zagros region. *Marine and Petroleum Geology*, *97*, 466–479. https://doi.org/https://doi.org/10.1016/j.marpetgeo.2018.06.027

Ding, W., Fan, T., Yu, B., Huang, X., & Liu, C. (2012). Ordovician carbonate reservoir fracture characteristics and fracture distribution forecasting in the Tazhong area of Tarim Basin, Northwest China. *Journal of Petroleum Science and Engineering*, *86–87*, 62–70. https://doi.org/10.1016/j.petrol.2012.03.006

Ding, Y., Liu, X. J., & Luo, P. Y. (2020). Investigation on influence of drilling unloading on wellbore stability in clay shale formation. *Petroleum Science*, *17*(3), 781–796. https://doi.org/10.1007/s12182-020-00438-w

Drucker, D. C. (1950). Some implications of work hardening and ideal plasticity. *Quarterly of Applied Mathematics*, *7*(4), 411–418.

Ekbote, S., & Abousleiman, Y. (2006). Porochemoelastic Solution for an Inclined Borehole in a Transversely Isotropic Formation. *Journal of Engineering Mechanics*, *132*(7), 754–763. https://doi.org/10.1061/(asce)0733-9399(2006)132:7(754)

Ekbote, S., Abousleiman, Y., Cui, L., & Zaman, M. (2004). Analyses of Inclined Boreholes in Poroelastic Media. *International Journal of Geomechanics*, *4*(3), 178–190. https://doi.org/10.1061/(asce)1532-3641(2004)4:3(178)

Evans, J. P., & Chester, F. M. (1995). Fluid-rock interaction in faults of the San Andreas system: Inferences from San Gabriel fault rock geochemistry and microstructures. *Journal of Geophysical Research: Solid Earth*, *100*(B7), 13007–13020.

Ezati, M., Azizzadeh, M., Riahi, M. A., Fattahpour, V., & Honarmand, J. (2020). Wellbore stability analysis using integrated geomechanical modeling: a case study from the Sarvak reservoir in one of the SW Iranian oil fields. *Arabian Journal of Geosciences*, *13*(4). https://doi.org/10.1007/s12517-020-5126-1

Fan, Z., & Parashar, R. (2019). Analytical solutions for a wellbore subjected to a non-isothermal fluid flux: Implications for optimizing injection rates, fracture reactivation, and EGS hydraulic stimulation. *Rock Mechanics and Rock Engineering*, *52*(11), 4715–4729.

Fang, Y., Elsworth, D., Ishibashi, T., & Zhang, F. (2018). Permeability Evolution and Frictional Stability of Fabricated Fractures With Specified Roughness. *Journal of Geophysical Research: Solid Earth*, *123*(11), 9355–9375. https://doi.org/10.1029/2018JB016215

Fjaer E, Holt RM, Horsrud P, Raeen AM, Risnes R (1992). *Petroleum Related Rock Mechanics*. Elsevier, Amsterdam

Fung, L. S. K., Wan, R. G., Rodriguez, H., & Bellorin, I. R. S. (1996). An Advanced Elasto-plastic Model For Borehole Stability Analysis of Horizontal Wells In Unconsolidated Formation. In *Annual Technical Meeting* (p. PETSOC-96-58). https://doi.org/10.2118/96-58

Garavand, A., Stefanov, Y. P., Rebetsky, Y. L., Bakeev, R. A., & Myasnikov, A. V. (2020). Numerical modeling of plastic deformation and failure around a wellbore in compaction and dilation modes. *International Journal for Numerical and Analytical Methods in Geomechanics*, *44*(6), 823–850. https://doi.org/10.1002/nag.3041

Gaston, D., Newman, C., Hansen, G., & Lebrun-Grandié, D. (2009). MOOSE: A parallel computational framework for coupled systems of nonlinear equations. *Nuclear Engineering and Design*, *239*(10), 1768–1778. https://doi.org/10.1016/j.nucengdes.2009.05.021

Gelet, R., Loret, B., & Khalili, N. (2012). Borehole stability analysis in a thermoporoelastic dual-porosity medium. *International Journal of Rock Mechanics and Mining Sciences*, *50*, 65–76. https://doi.org/https://doi.org/10.1016/j.ijrmms.2011.12.003

Gomar, M., Goodarznia, I., & Shadizadeh, S. R. (2016). Fully coupled analysis of interaction between the borehole and pre-existing fractures. *International Journal of Rock Mechanics and Mining Sciences*, *89*, 151–164. https://doi.org/10.1016/j.ijrmms.2016.07.029

Grasby, S. E., Majorowicz, J., & McCune, G. (2012). *Geothermal Energy Potential for Northern Communities*. Natural Resources Canada.

Heidari, S., Li, B., Jacquey, A. B., & Xu, B. (2023). Constitutive modeling of a laumontite-rich tight rock and the application to poromechanical analysis of deeply drilled wells. *Rock Mechanics Bulletin*, *2*(2), 100039.

Heidari, S., Li, B., Zsaki, A. M., Xu, B., & Wang, C. (2021). Stability analysis of a super deep petroleum well drilled in strike-slip fault zones in the Tarim Basin, NW China. *Arabian Journal of Geosciences*, *14*(8), 675. https://doi.org/10.1007/s12517-021-06709-z

Hosseini, S. M., Goebel, T. H. W., Jha, B., & Aminzadeh, F. (2018). A Probabilistic Approach to Injection-Induced Seismicity Assessment in the Presence and Absence of Flow Boundaries. *Geophysical Research Letters*, *45*(16), 8182–8189. https://doi.org/10.1029/2018GL077552

Hu, M., Veveakis, M., & Regenauer-Lieb, K. (2018). Influence of stress field anisotropy on drilling-induced tensile fracture. *Environmental Geotechnics*, *7*(5), 373–379.

Iranmanesh, M. A., & Pak, A. (2018). Extrinsically enriched element free Galerkin method for heat and fluid flow in deformable porous media involving weak and strong discontinuities. *Computers and Geotechnics*, *103*(July), 179–192. https://doi.org/10.1016/j.compgeo.2018.07.013

Jacquey, A. B., Cacace, M., Blöcher, G., & Scheck-Wenderoth, M. (2015). Numerical Investigation of Thermoelastic Effects on Fault Slip Tendency during Injection and Production of Geothermal Fluids. *Energy Procedia*, *76*, 311–320. https://doi.org/https://doi.org/10.1016/j.egypro.2015.07.868

Jacquey, A. B., Cacace, M., Blöcher, G., Watanabe, N., Huenges, E., & Scheck-Wenderoth, M. (2016). Thermo-poroelastic numerical modelling for enhanced geothermal system performance: Case study of the Groß Schönebeck reservoir. *Tectonophysics*, *684*, 119–130. https://doi.org/https://doi.org/10.1016/j.tecto.2015.12.020

Jacquey, A. B., & Regenauer-Lieb, K. (2021). Thermomechanics for Geological, Civil Engineering and Geodynamic Applications: Rate-Dependent Critical State Line Models. *Rock Mechanics and Rock Engineering*, *54*(10), 5355–5373. https://doi.org/10.1007/s00603-021-02397-z

Jacquey, A. B., Regenauer-Lieb, K., & Cacace, M. (2021). Thermomechanics for Geological, Civil Engineering and Geodynamic Applications: Numerical Implementation and Application to the Bentheim Sandstone. *Rock Mechanics and Rock Engineering*, *54*(10), 5337–5354. https://doi.org/10.1007/s00603-021-02582-0

Jacquey, A. B., Urpi, L., Cacace, M., Blöcher, G., Zimmermann, G., & Scheck-Wenderoth, M. (2018). Far field poroelastic response of geothermal reservoirs to hydraulic stimulation treatment: Theory and application at the Groß Schönebeck geothermal research facility. *International Journal of Rock Mechanics and Mining Sciences*, *110*, 316–327. https://doi.org/https://doi.org/10.1016/j.ijrmms.2018.08.012

Jaeger, J. C., Cook, N. G. W., & Zimmerman, R. (2007). *Fundamentals of rock mechanics*. John Wiley & Sons.

Jeanne, P., Rutqvist, J., Dobson, P. F., Walters, M., Hartline, C., & Garcia, J. (2014). The impacts of mechanical stress transfers caused by hydromechanical and thermal processes on fault stability during hydraulic stimulation in a deep geothermal reservoir. *International Journal of Rock Mechanics and Mining Sciences*, *72*, 149–163. https://doi.org/https://doi.org/10.1016/j.ijrmms.2014.09.005

Jiang, H., & Xie, Y. (2011). A note on the Mohr–Coulomb and Drucker–Prager strength criteria. *Mechanics Research Communications*, *38*(4), 309–314.

Kang, Y., Yu, M., Miska, S., & Takach, N. E. (2009). Wellbore Stability: A Critical Review and Introduction to DEM. In *SPE Annual Technical Conference and Exhibition* (p. SPE-124669-MS). https://doi.org/10.2118/124669-MS

Khalili, N., & Selvadurai, A. P. S. (2003). A fully coupled constitutive model for thermo-hydro-mechanical analysis in elastic media with double porosity. *Geophysical Research Letters*, *30*(24), 1–5. https://doi.org/10.1029/2003GL018838

Labuz, J. F., & Zang, A. (2012). Mohr–Coulomb failure criterion. *Rock Mechanics and Rock Engineering*, *45*, 975–979.

Lee, H., Ong, S. H., Azeemuddin, M., & Goodman, H. (2012). A wellbore stability model for formations with anisotropic rock strengths. *Journal of Petroleum Science and Engineering*, *96–97*, 109–119. https://doi.org/10.1016/j.petrol.2012.08.010

Levasseur, S., Charlier, R., Frieg, B., & Collin, F. (2010). Hydro-mechanical modelling of the excavation damaged zone around an underground excavation at Mont Terri Rock Laboratory. *International Journal of Rock Mechanics and Mining Sciences*, *47*(3), 414–425. https://doi.org/10.1016/j.ijrmms.2010.01.006

Lewis R W, Schrefler B A. (1998). The finite Element Method in the Static and Dynamic Deformation and Consolidation of Porous Media. *John Wiley& Sons.*

Li, B., & Wong, R. C. K. (2017). A mechanistic model for anisotropic thermal strain behavior of soft mudrocks. *Engineering Geology*, *228*. https://doi.org/10.1016/j.enggeo.2017.08.008

Li, B., Wong, R. C. K., & Milnes, T. (2014). Anisotropy in capillary invasion and fluid flow through induced sandstone and shale fractures. *International Journal of Rock Mechanics and Mining Sciences*, *65*, 129–140. https://doi.org/https://doi.org/10.1016/j.ijrmms.2013.10.004

Li, B., Wong, R. C. K., Xu, B., & Yang, B. (2018a). Comprehensive stability analysis of an inclined wellbore embedded in Colorado shale formation for thermal recovery. *International Journal of Rock Mechanics and Mining Sciences*. https://doi.org/10.1016/j.ijrmms.2018.07.019

Li, C., Wang, X., Li, B., & He, D. (2013). Paleozoic fault systems of the Tazhong Uplift, Tarim Basin, China. *Marine and Petroleum Geology*, *39*(1), 48–58. https://doi.org/https://doi.org/10.1016/j.marpetgeo.2012.09.010

Li, H. (2022). Development Characteristics of Silurian Strike-Slip Faults and Fractures and Their Effects on Drilling Leakage in Shunbei Area of Tarim Basin. *Frontiers in Earth Science*, *10*(June), 1–12. https://doi.org/10.3389/feart.2022.938765

Li, M., & Zhang, F. (2022). Discrete Element Modeling of Hydraulic Fracturing. In *Mechanics of Hydraulic Fracturing* (pp. 141–175). https://doi.org/https://doi.org/10.1002/9781119742487.ch12

Li, W., Chen, M., Jin, Y., Lu, Y., Gao, J., Meng, H., Zhang, Y., & Tan, P. (2018b). Effect of local thermal non-equilibrium on thermoporoelastic response of a borehole in dual-porosity media. *Applied Thermal Engineering*, *142*(May), 166–183. https://doi.org/10.1016/j.applthermaleng.2018.06.055

Li, X. (2003). Consolidation around a borehole embedded in media with double porosity under release of geostatic stresses. *Mechanics Research Communications*, *30*(1), 95–100. https://doi.org/10.1016/S0093-6413(02)00315-4

Li, X., El Mohtar, C. S., & Gray, K. E. (2019). Modeling progressive breakouts in deviated wellbores. *Journal of Petroleum Science and Engineering*, *175*(January), 905–918. https://doi.org/10.1016/j.petrol.2019.01.007

Li, X., Zhang, C., Feng, Y., Wei, Y., Chen, X., Weng, H., & Deng, J. (2022). An integrated geomechanics approach to evaluate and manage wellbore stability in a deep graben formation in Tarim Basin. *Journal of Petroleum Science and Engineering*, *208*(PA), 109391. https://doi.org/10.1016/j.petrol.2021.109391

Lisle, R. J., & Srivastava, D. C. (2004). Test of the frictional reactivation theory for faults and validity of fault-slip analysis. *Geology*, *32*(7), 569–572.

Liu, C., & Abousleiman, Y. N. (2016). N-Porosity and N-Permeability Generalized Wellbore Stability Analytical Solutions and Applications. In *50th U.S. Rock Mechanics/Geomechanics Symposium* (p. ARMA-2016-417).

Liu, J. G., Xu, B., Sun, L., Li, B., & Wei, G. J. (2022). In situ stress field in the Athabasca oil sands deposits: Field measurement, stress-field modeling, and engineering implications. *Journal of Petroleum Science and Engineering*, *215*, 110671. https://doi.org/https://doi.org/10.1016/j.petrol.2022.110671

Ma, T., & Chen, P. (2015). A wellbore stability analysis model with chemical-mechanical coupling for shale gas reservoirs. *Journal of Natural Gas Science and Engineering*, *26*, 72–98. https://doi.org/10.1016/j.jngse.2015.05.028

Ma, X., Zhang, S., Zhang, X., Liu, J., Jin, J., Cheng, W., Jiang, W., Zhang, G., Chen, Z., & Zoback, M. D. (2022). Lithology-controlled stress variations of Longmaxi shale – Example of an appraisal wellbore in the Changning area. *Rock Mechanics Bulletin*, *1*(1), 100002. https://doi.org/https://doi.org/10.1016/j.rockmb.2022.100002

Mehrabian, A., & Abousleiman, Y. N. (2014). Generalized Biot's theory and Mandel's problem of multiple-porosity and multiple-permeability poroelasticity. *Journal of Geophysical Research: Solid Earth*, *119*(4), 2745–2763. https://doi.org/https://doi.org/10.1002/2013JB010602

Méndez, J. N., Jin, Q., González, M., Zhang, X., Lobo, C., Boateng, C. D., & Zambrano, M. (2020). Fracture characterization and modeling of karsted carbonate reservoirs: A case study in Tahe oilfield, Tarim Basin (western China). *Marine and Petroleum Geology*, *112*, 104104. https://doi.org/https://doi.org/10.1016/j.marpetgeo.2019.104104

Meng, M., Baldino, S., Miska, S. Z., & Takach, N. (2019). Wellbore stability in naturally fractured formations featuring dual-porosity/single-permeability and finite radial fluid discharge. *Journal of Petroleum Science and Engineering*, *174*(November 2018), 790–803. https://doi.org/10.1016/j.petrol.2018.11.088

Mirabbasi, S. M., Ameri, M. J., Biglari, F. R., & Shirzadi, A. (2020). Thermo-poroelastic wellbore strengthening modeling: An analytical approach based on fracture mechanics. *Journal of Petroleum Science and Engineering*, *195*, 107492.

Miranda, M. M., Raymond, J., & Dezayes, C. (2020). Uncertainty and risk evaluation of deep geothermal energy source for heat production and electricity generation in remote northern regions. *Energies*, *13*(6), 5–19. https://doi.org/10.3390/en13164221

Miranda, M. M., Raymond, J., & Dezayes, C. (2023a). Estimating theoretical stress regime for engineered geothermal energy systems in an arctic community (Kuujjuaq, Canada). *Comptes Rendus. Géoscience*, *355*(G1), 85–108.

Miranda, M.M., Raymond, J., Dezayes, C., Wigston, A., Perreault. S., (2023b). Impact of fracture properties on the performance of engineered geothermal systems in the crystalline basement of Kuujjuaq (Canadian Shield) 1–34. https://doi.org/10.21203/rs.3.rs-2416987/v1

Morrow, C. A., & Byerlee, J. D. (1991). A note on the frictional strength of laumontite from Cajon Pass, California. *Geophysical Research Letters*, *18*(2), 211–214.

Mukherjee, M., Nguyen, G. D., Mir, A., Bui, H. H., Shen, L., El-Zein, A., & Maggi, F. (2017). Capturing pressure- and rate-dependent behaviour of rocks using a new damage-plasticity model. *International Journal of Impact Engineering*, *110*, 208–218. https://doi.org/https://doi.org/10.1016/j.ijimpeng.2017.01.006

Nair, R., Abousleiman, Y., & Zaman, M. (2004). A finite element porothermoelastic model for dual-porosity media. *International Journal for Numerical and Analytical Methods in Geomechanics*, *28*(9), 875–898.

Nair, R., Abousleiman, Y., & Zaman, M. (2005). Modeling Fully Coupled Oil–Gas Flow in a Dual-Porosity Medium. *International Journal of Geomechanics*, *5*(4), 326–338. https://doi.org/10.1061/(asce)1532-3641(2005)5:4(326)

Nguyen, V. X., & Abousleiman, Y. N. (2010). Poromechanics solutions to plane strain and axisymmetric mandel-type problems in dual-porosity and dual-permeability medium. *Journal of Applied Mechanics, Transactions ASME*, *77*(1), 1–18. https://doi.org/10.1115/1.3172146

Nguyen, V. X., Abousleiman, Y. N., & Hoang, S. K. (2009). Analyses of wellbore instability in drilling through chemically active fractured-rock formations. *SPE Journal*, *14*(2), 283–301. https://doi.org/10.2118/105383-PA

Norouzi, E., Moslemzadeh, H., & Mohammadi, S. (2019). Maximum entropy based finite element analysis of porous media. *Frontiers of Structural and Civil Engineering*, *13*(2), 364–379. https://doi.org/10.1007/s11709-018-0470-x

Paterson MS, Wong T-F (2005). Experimental Rock Deformation – *The Brittle Field. Springer-Verlag*, Berlin Heidelberg

Proctor, B., Lockner, D. A., Kilgore, B. D., Mitchell, T. M., & Beeler, N. M. (2020). Direct Evidence for Fluid Pressure, Dilatancy, and Compaction Affecting Slip in Isolated Faults. *Geophysical Research Letters*, *47*(16). https://doi.org/10.1029/2019GL086767

Puzrin, A. (2012). *Constitutive modelling in geomechanics: introduction*. Springer Science & Business Media.

Solum, J. G., van der Pluijm, B. A., Peacor, D. R., & Warr, L. N. (2003). Influence of phyllosilicate mineral assemblages, fabrics, and fluids on the behavior of the Punchbowl fault, southern California. *Journal of Geophysical Research: Solid Earth*, *108*(B5). https://doi.org/https://doi.org/10.1029/2002JB001858

Stehfest, H. (1970). Algorithm 368: Numerical inversion of Laplace transforms [D5]. *Communications of the ACM*, *13*(1), 47–49.

Tang, Z., Kong, X., Duan, W., & Gao, J. (2021). Wellbore breakout analysis and the maximum horizontal stress determination using the thermo-poroelasticity model. *Journal of Petroleum Science and Engineering*, *196*, 107674.

Tian, F., Luo, X., & Zhang, W. (2019). Integrated geological-geophysical characterizations of deeply buried fractured-vuggy carbonate reservoirs in Ordovician strata, Tarim Basin. *Marine and Petroleum Geology*, *99*, 292–309. https://doi.org/https://doi.org/10.1016/j.marpetgeo.2018.10.028

Vajdova, V., Baud, P., & Wong, T. fong. (2004). Compaction, dilatancy, and failure in porous carbonate rocks. *Journal of Geophysical Research: Solid Earth*, *109*(5), 1–16. https://doi.org/10.1029/2003JB002508

Veeken, C. A. M., Walters, J. V, Kenter, C. J., & Davies, D. R. (1989). Use of Plasticity Models For Predicting Borehole Stability. In *ISRM International Symposium* (p. ISRM-IS-1989-106).

Vermeer, P. A., & De Borst, R. (1984). Non-associated plasticity for soils, concrete and rock. *HERON, 29 (3), 1984*.

Vernik, L. (1990). A new type of reservoir rock in volcaniclastic sequences. *AAPG Bulletin*, *74*(6), 830–836.

Vernik, L., & Nur, A. (1992). Petrophysical analysis of the Cajon Pass scientific well: implications for fluid flow and seismic studies in the continental crust. *Journal of Geophysical Research: Solid Earth*, *97*(B4), 5121–5134.

Wang, Y., & Dusseault, M. B. (2003). A coupled conductive-convective thermo-poroelastic solution and implications for wellbore stability. *Journal of Petroleum Science and Engineering*, *38*(3–4), 187–198. https://doi.org/10.1016/S0920-4105(03)00032-9

Wang, Y., Li, W., & Dusseault, M. B. (2021). THM response of a borehole in naturally fractured media. *Journal of Petroleum Science and Engineering*, *205*(September 2020). https://doi.org/10.1016/j.petrol.2021.108941

White, C. L. I. M., Ruiz-Salvador, A. R., & Lewis, D. W. (2004). Pressure-Induced Hydration Effects in the Zeolite Laumontite. *Angewandte Chemie*, *116*(4), 475–478.

Wilson, R. K., & Aifantis, E. C. (1982). On the theory of consolidation with double porosity. *International Journal of Engineering Science*, *20*(9), 1009–1035. https://doi.org/https://doi.org/10.1016/0020-7225(82)90036-2

Wong, T., David, C., & Zhu, W. (1997). The transition from brittle faulting to cataclastic flow in porous sandstones: Mechanical deformation. *Journal of Geophysical Research: Solid Earth*, *102*(B2), 3009–3025. https://doi.org/10.1029/96jb03281

Wu, B., Zhang, X., Jeffrey, R. G., & Wu, B. (2012). A semi-analytic solution of a wellbore in a non-isothermal low-permeability porous medium under non-hydrostatic stresses. *International Journal of Solids and Structures*, *49*(13), 1472–1484. https://doi.org/10.1016/j.ijsolstr.2012.02.035

Wu, G., Xie, E., Zhang, Y., Qing, H., Luo, X., & Sun, C. (2019a). Structural diagenesis in carbonate rocks as identified in fault damage zones in the Northern Tarim Basin, NW China. *Minerals*, *9*(6), 16–22. https://doi.org/10.3390/min9060360

Wu J, Fan T, Gomez-Rivas E, Gao Z, Yao S, Li W, Zhang C, Sun Q, Gu Y, Xiang M (2019b). Impact of pore structure and fractal characteristics on the sealing capacity of Ordovician carbonate cap rock in the Tarim Basin, China. *Mar Pet Geol 102*:557 579. https://doi.org/10.1016/j.marpetgeo.2019.01.014

Wu, G., Zhao, K., Qu, H., Scarselli, N., Zhang, Y., Han, J., & Xu, Y. (2020). Permeability distribution and scaling in multi-stages carbonate damage zones: Insight from strike-slip fault zones in the Tarim Basin, NW China. *Marine and Petroleum Geology*, *114*, 104208. https://doi.org/https://doi.org/10.1016/j.marpetgeo.2019.104208

Wu, H., Zhao, J., & Guo, N. (2018). Multiscale insights into borehole instabilities in high-porosity sandstones. *Journal of Geophysical Research: Solid Earth*, *123*(5), 3450–3473.

Yang, S., Jin, Y., Lu, Y., Zhang, Y., & Chen, B. (2021). Performance of Hydraulically Fractured Wells in Xinjiang Oilfield: Experimental and Simulation Investigations on Laumontite-Rich Tight Glutenite Formation. *Energies*, *14*(6), 1667.

Younessi, A., & Rasouli, V. (2010). A fracture sliding potential index for wellbore stability analysis. *International Journal of Rock Mechanics and Mining Sciences*, *47*(6), 927–939. https://doi.org/10.1016/j.ijrmms.2010.05.014

Yuan, J. L., Deng, J. G., Tan, Q., Yu, B. H., & Jin, X. C. (2013). Borehole stability analysis of horizontal drilling in shale gas reservoirs. *Rock Mechanics and Rock Engineering*, *46*(5), 1157–1164. https://doi.org/10.1007/s00603-012-0341-z

Zeng, W., Liu, X., Liang, L., & Xiong, J. (2018). Analysis of influencing factors of wellbore stability in shale formations. *Arabian Journal of Geosciences*, *11*(18), 1–10. https://doi.org/10.1007/s12517-018-3865-z

Zhang, F., An, M., Zhang, L., Fang, Y., & Elsworth, D. (2019). The role of mineral composition on the frictional and stability properties of powdered reservoir rocks. *Journal of Geophysical Research: Solid Earth*, *124*(2), 1480–1497.

Zhang, F., An, M., Zhang, L., Fang, Y., & Elsworth, D. (2020). Effect of mineralogy on friction-dilation relationships for simulated faults: Implications for permeability evolution in caprock faults. *Geoscience Frontiers*, *11*(2), 439–450. https://doi.org/10.1016/j.gsf.2019.05.014

Zhang, F., Huang, R., An, M., Min, K., Elsworth, D., Hofmann, H., & Wang, X. (2022). Competing Controls of Effective Stress Variation and Chloritization on Friction and Stability of Faults in Granite: Implications for Seismicity Triggered by Fluid Injection. *Journal of Geophysical Research: Solid Earth*, *127*(8), e2022JB024310.

Zhang, F., Zhang, S., Jiang, X., Lu, R., & Chen, M. (2008). Borehole stability in naturally fractured reservoirs during production tests. *Petroleum Science*, *5*(3), 247–250. https://doi.org/10.1007/s12182-008-0039-8

Zhang, J. (2013). Borehole stability analysis accounting for anisotropies in drilling to weak bedding planes. *International Journal of Rock Mechanics and Mining Sciences*, *60*, 160–170. https://doi.org/10.1016/j.ijrmms.2012.12.025

Zhang, J., Bai, M., & Roegiers, J. C. (2003). Dual-porosity poroelastic analyses of wellbore stability. *International Journal of Rock Mechanics and Mining Sciences*, *40*(4), 473–483. https://doi.org/10.1016/S1365-1609(03)00019-4

Zhang, X., Jeffrey, R. G., & Thiercelin, M. (2009). Mechanics of fluid-driven fracture growth in naturally fractured reservoirs with simple network geometries. *Journal of Geophysical Research: Solid Earth*, *114*(12), 1–16. https://doi.org/10.1029/2009JB006548

Zhang, Y., Ding, X., Yang, P., Liu, Y., Jiang, Q., & Zhang, S. (2016). Reservoir formation mechanism analysis and deep high-quality reservoir prediction in Yingcheng Formation in Longfengshan area of Songliao Basin, China. *Petroleum*, *2*(4), 334–343. https://doi.org/https://doi.org/10.1016/j.petlm.2016.09.003

Zhang, Y., Tan, F., Sun, Y., Pan, W., Wang, Z., Yang, H., & Zhao, J. (2018). Differences between reservoirs in the intra-platform and platform margin reef-shoal complexes of the Upper Ordovician Lianglitag Formation in the Tazhong oil field, NW China, and corresponding exploration strategies. *Marine and Petroleum Geology*, *98*, 66–78. https://doi.org/https://doi.org/10.1016/j.marpetgeo.2018.07.013

Zheng, Z., Su, G., Jiang, Q., Pan, P., Huang, X., & Jiang, J. (2022a). Mechanical behavior and failure mechanisms of cylindrical and prismatic rock specimens under various confining stresses. *International Journal of Damage Mechanics*, *31*(6), 864–881.

Zheng, Z., Su, H., Mei, G., Cao, Y., Wang, W., Feng, G., & Jiang, Q. (2022b). Experimental and damage constitutive study of the stress-induced post-peak deformation and brittle–ductile behaviours of prismatic deeply buried marble. *Bulletin of Engineering Geology and the Environment*, *81*(10), 427.

Zhou, H., Kong, G., Liu, H., & Chen, S. L. (2016). A semi-analytical solution for cylindrical cavity expansion in elastic–perfectly plastic soil under biaxial in situ stress field. *Géotechnique*, *66*(9), 786–788. https://doi.org/10.1680/jgeot.16.P.077r

Zhou, J., Ding, S. D., Jiang, T. X., Bian, X. B., Liu, B. Y., Zhang, X., Geng, Y. D., & Mao, H. J. (2020). Research on Reservoir Geostress Characteristics of Ultra-Deep Carbonate Rocks With Multiple Fault Zones. In *54th U.S. Rock Mechanics/Geomechanics Symposium* (p. ARMA-2020-1798).

Zhu, C., & Arson, C. (2014). A thermo-mechanical damage model for rock stiffness during anisotropic crack opening and closure. *Acta Geotechnica*, *9*(5), 847–867. https://doi.org/10.1007/s11440-013-0281-0

Zhu, Q., & Shao, J. (2017). Micromechanics of rock damage: Advances in the quasi-brittle field. *Journal of Rock Mechanics and Geotechnical Engineering*, *9*(1), 29–40.

Zoback, M. D. (2007). *Reservoir Geomechanics*. Cambridge University Press. https://doi.org/10.1017/CBO9780511586477

Zoback, M. D. (2010). *Reservoir geomechanics*. Cambridge university press.

Zoback, M. D., Moos, D., Mastin, L., & Anderson, R. N. (1985). Well Bore Breakouts and in Situ Stress. *Journal of Geophysical Research*, *90*(B7), 5523–5530. https://doi.org/10.1029/JB090iB07p05523